DEVELOPMENT OF A STRONTIUM MAGNETO-OPTICAL TRAP FOR PROBING CASIMIR–POLDER POTENTIALS

by

PAUL J. MARTIN

A DISSERTATION

Presented to the Department of Physics
and the Graduate School of the University of Oregon
in partial fulfillment of the requirements
for the degree of
Doctor of Philosophy

March 2017

DISSERTATION APPROVAL PAGE

Student: Paul J. Martin

Title: Development of a Strontium Magneto-Optical Trap for Probing Casimir–Polder Potentials

This dissertation has been accepted and approved in partial fulfillment of the requirements for the Doctor of Philosophy degree in the Department of Physics by:

Michael G. Raymer	Chair
Daniel A. Steck	Advisor
Benjamin J. McMorran	Core Member
George V. Nazin	Institutional Representative

and

Scott L. Pratt	Dean of the Graduate School

Original approval signatures are on file with the University of Oregon Graduate School.

Degree awarded March 2017

DISSERTATION ABSTRACT

Paul J. Martin

Doctor of Philosophy

Department of Physics

March 2017

Title: Development of a Strontium Magneto-Optical Trap for Probing Casimir–Polder Potentials

In recent years, cold atoms have been the centerpiece of many remarkably sensitive measurements, and much effort has been made to devise miniaturized quantum sensors and quantum information processing devices. At small distances, however, mechanical effects of the quantum vacuum begin to significantly impact the behavior of the cold-atom systems. A better understanding of how surface composition and geometry affect Casimir and Casimir–Polder potentials would benefit future engineering of small-scale devices. Unfortunately, theoretical solutions are limited and the number of experimental techniques that can accurately detect such short-range forces is relatively small.

We believe the exemplary properties of atomic strontium—which have enabled unprecedented frequency metrology in optical lattice clocks—make it an ideal candidate for probing slight spectroscopic perturbations caused by vacuum fluctuations. To that end, we have constructed a magneto-optical trap for strontium to enable future study of atom–surface potentials, and the apparatus and proposed detection scheme are discussed herein. Of special note is a passively stable external-cavity diode laser we developed that is both affordable and competitive with high-end commercial options.

CURRICULUM VITAE

NAME OF AUTHOR: Paul J. Martin

GRADUATE AND UNDERGRADUATE SCHOOLS ATTENDED:

University of Oregon, Eugene, OR
University of New Mexico, Albuquerque, NM

DEGREES AWARDED:

Doctor of Philosophy, Physics, 2017, University of Oregon
Master of Science, Physics, 2014, University of Oregon
Bachelor of Science, Physics, 2007, University of New Mexico
Bachelor of Science, Applied Mathematics, 2007, University of New Mexico

AREAS OF SPECIAL INTEREST:

Atomic, Molecular, and Optical Physics
Experimental Design and Control

PROFESSIONAL EXPERIENCE:

Graduate Teaching Fellow, University of Oregon, 2007–2011, 2013–2017

Graduate STEM Fellow in K–12 Education, NSF GK–12, University of Oregon, 2011–2013

Undergraduate Research Assistant, University of New Mexico, 2007–2008

Physics Tutor, Center for Academic Program Support at the University of New Mexico, 2004–2007

GRANTS, AWARDS AND HONORS:

Weiser Senior Teaching Assistant Award, University of Oregon, 2015

Graduate STEM fellow in K-12 Education, NSF GK-12, University of Oregon, 2011-2013

Honorable Mention, National Science Foundation Graduate Research Fellowship Program, 2008

Qualifying exam award for outstanding performance, University of Oregon, 2008

Eoin Grey Award for "Best graduating senior in physics" at the University of New Mexico, 2007

Departmental and University Honors, University of New Mexico, 2007

Summa cum Laude, University of New Mexico, 2007

National Merit Scholarship Finalist, 2002

PUBLICATIONS:

Chris Seck, Paul J. Martin, Eryn C. Cook, Brian Odom, and Daniel A. Steck, "Noise reduction of a Libbrecht–Hall-style current driver," *Review of Scientific Instruments* **87**, 064703 (2016).

Jayampathi C. B. Kangara, Andrew J. Hachtel, Matthew C. Gillette, Jason T. Barkeloo, Ethan Clements, Samir Bali, Brett E. Unks, Nicholas A. Proite, Deniz D. Yavuz, Paul J. Martin, Jeremy J. Thorn, and Daniel A. Steck, "Design and construction of cost-effective tapered amplifier systems for laser cooling and trapping experiments," *American Journal of Physics* **82**, 805 (2014).

Eryn C. Cook, Paul J. Martin, Tobias L. Brown–Heft, Jeffrey C. Garman, and Daniel A. Steck, "High-passive-stability diode-laser design for use in atomic-physics experiments," *Review of Scientific Instruments* **83**, 043101 (2012).

Rob L. Cook, Paul J. Martin, and J. M. Geremia, "Optical coherent state discrimination using a closed-loop quantum measurement," *Nature* **446**, (2007).

ACKNOWLEDGEMENTS

Work behind the contents of this dissertation took place over several years and would not have been possible without the help of *many* people who assisted me both professionally and personally.

First, I need to acknowledge the work presented here belongs equally to my good friend and colleague Eryn Cook. We built the Sr apparatus together from scratch, and this thesis could not have been realized without her efforts. Eryn exemplifies the skeptical and inquisitive nature of a scientist, and I appreciate the objective clarity she brings when we are attempting to understand a process or solve a problem. On many occasions she prevented us from chasing a misconception—wasting time and effort—before thinking something through more clearly.

My advisor, Dan Steck, is unique as a hybrid of experimentalist and theorist, and he has been a wealth of knowledge and patience during this project. I thank him for providing Eryn and me with the opportunity to take a new project and develop it into our own. I admire Dan's ability to fully research and focus on a topic (even outside of physics), and especially appreciate his attention to detail. I hope I absorbed these qualities in some way and can better emulate them in the future.

Other members of Steck Lab also positively impacted my experience (including the lab dog, Maya!). The venerable first generation—Tao, Libby, and Jeremy—set a high bar that we strove to meet in the Sr apparatus. Jonathan, Richard, and Wes also were fun to work with, and we shared in many enjoyable non-physics conversations, including discussions about heavy metal, woeful baseball teams, and Kaggle. I am thankful for the help of many undergrads in the construction of the apparatus, but I must explicitly thank Tobias Brown–Heft for his extraordinary contributions.

The resources and expertise available at the UO TSA machine shop were invaluable in my experience. We owe a lot to the efforts of Kris and John, but Jeffrey in particular deserves special thanks. He masterfully crafted eight of our novel ECDLs and his consultation improved the design considerably.

I have also enjoyed wonderful investment from my friends, church, and family. Within the physics department I'd like to especially acknowledge—in alphabetical order—the support from my friends: Tom Baldwin, Eryn Cook, Brian Hake, Jonathan Mackrory, Erin Mondloch, Ryan Quitzow–James, Libby Schoene, Jake Searcy, Mike Taormina, and Dash Vitullo. My friends who have little to do with physics are also a deep well of encouragement: Stu Johnson, my "buddies," and the "Sunday Suppa" group. When my wife and daughter lived in Albuquerque during the final push, I was effectively adopted by several friends—especially the 'other' Martins, the Kruses, D. Bear, and Stu—and I am forever grateful for their love and hospitality.

Part friend, family, and new-parent and physics comrade, my brother Kyle understands my life more than most, and I am thankful for our conversations. My parents are my most stalwart supporters, and I am grateful for their love and sacrifices, from driving across the country with me in a moving van (twice) to enduring an hour-long physics thesis defense. My in-laws also provided prayers, love, and support, and I am thankful for the ways they support my family.

Finally, I owe the deepest gratitude to my wonderful and beautiful wife, Analisa, and our darling daughter, Elise. Analisa faithfully and patiently encouraged me, and provided uplifting refuge during difficult times. I am grateful for the sacrifices she made being married to a graduate student, and I have immensely enjoyed discovering the difficulties and delights of sharing my life with someone. Elise is a blessing to our family, and I am thankful for the unbridled joy she brings with a simple smile.

TABLE OF CONTENTS

Chapter Page

I. INTRODUCTION 1

1.1. Precision Metrology with Cold Atoms 1

1.2. Cold Strontium 2

1.3. Quantum Vacuum Effects 3

II. CASIMIR–POLDER POTENTIALS AND COLD STRONTIUM 5

2.1. Background 5

2.1.1. Casimir–Polder Potential 7

2.1.2. Previous Experimental Approaches 12

2.2. Strontium Atoms as Casimir–Polder Detectors 16

2.2.1. Optical Lattice Technique 18

2.2.2. Feasibility 20

2.2.3. Outlook 22

III. NOVEL EXTERNAL-CAVITY DIODE LASER 23

3.1. Stabilizing Cavity Length 25

3.1.1. Diffraction Grating Arm 26

3.1.2. Laser Diode Current Source 28

3.1.3. Additional Measures 29

3.2. Sensitivity to Perturbations 32

3.3. Linewidth Measurements 38

3.4. Construction and Assembly Details 43

3.4.1. Customizing a Particular Wavelength 43

Chapter Page

3.4.2. Final Assembly and Alignment 47

IV. EXPERIMENTAL APPARATUS 51

4.1. Vacuum System 51

4.1.1. Hot Strontium Source 53

4.1.1.1. Oven Design 53

4.1.1.2. Molecular Flow Conductance 55

4.1.1.3. Operating Lifetime and Beam Flux 56

4.1.1.4. Atomic Beam Considerations 59

4.1.2. Chamber Design 60

4.1.3. Assembly and Bakeout 63

4.1.4. Magnetic Coils 67

4.1.5. Zeeman Slower 70

4.2. Laser Systems 76

4.2.1. Tapered Amplifier 78

4.2.2. Second-Harmonic Generation 84

4.2.3. Frequency Stabilization 88

4.2.3.1. Heat-Pipe Vapor Cell 88

4.2.3.2. Frequency-Modulation Spectroscopy 91

4.2.3.3. Helical Resonators 95

4.2.4. Slave Laser 97

4.3. Electronics 98

4.3.1. Radio-Frequency Electronics 99

4.3.2. Computer Control 101

Chapter Page

V. TRAPPING AND COOLING STRONTIUM 103

5.1. Double-MOT Scheme 105

5.2. Blue MOT Temperature Measurements 107

5.2.1. Imaging System 109

5.2.2. Expansion Data and Temperature Estimate 110

5.3. Cooling in a Red MOT 116

5.3.1. Transfer Process 117

5.3.2. Current Progress 119

VI. CONCLUSION 123

APPENDICES

A. TRAPPING BASICS: MECHANICAL FORCES OF LIGHT . . . 126

A.1. Optical Molasses 128

A.2. Magneto-Optical Trap 131

A.3. Dipole Force and Optical Lattices 133

B. STRONTIUM DETAILS 135

B.1. Dipole Matrix Elements 139

B.1.1. Example: Ground State Dipole Potential 141

B.2. Casimir–Polder Level Shifts 142

B.3. Tabulated Data 145

C. DELAYED SELF-HETERODYNE METHOD 149

C.1. Mathematical Framework 150

C.2. Heterodyne Measurement 153

Chapter Page

C.3. Delayed Self-Heterodyne Measurement 155

C.3.1. White Noise 157

C.3.2. Adding $1/f$ Noise 159

C.3.3. Laser Linewidth and Observation Time 160

REFERENCES CITED 162

LIST OF FIGURES

Figure Page

2.1. Feynman diagram of an atom in its ground state interacting with the electromagnetic vacuum field 10

2.2. Level shift of the ground state of strontium near a perfectly conducting plate 13

2.3. Trapping potentials of the optical lattice and the CP effect 20

2.4. Expected differential level shifts due to the Casimir–Polder potential between strontium atoms and a perfect conductor 21

3.1. Sketch of a Littrow-configuration ECDL 26

3.2. A rendering of the ECDL diffraction grating arm, which rotates via a notch-hinge flexure 28

3.3. Laser susceptibility to noise in the current supply 30

3.4. Assembly drawing of the novel ECDL, featuring labels of all peripherals 31

3.5. Schematics for methods we use to analyze the laser's susceptibility to environmental perturbations 33

3.6. Laser response while driving the piezo at acoustic frequencies in the cavity resonance spectroscopy setup 34

3.7. Response of a prototype laser under various driving amplitudes in cavity resonance spectroscopy 35

3.8. Frequency-noise power spectral density (fSD) as a function of frequency, measured with the setup in Fig. 3.5(b) from 0–20 kHz 37

3.9. Schematic depicting the delayed self-heterodyne measurement 39

3.10. Delayed self-heterodyne spectra of a 922 nm laser 41

3.11. Delayed self-heterodyne spectra of long and short 689 nm lasers 43

Figure Page

3.12. Wavelengths that can be realized with the novel ECDL design using stock Richardson diffraction gratings between 300 nm and 1500 nm 44

3.13. Numerically determining the location of anamorphic prisms 46

4.1. Schematic of the UHV chamber used for trapping and cooling strontium atoms 52

4.2. Schematic of the strontium source. A crucible and collimation nozzle are centered in a custom-length nipple and heated externally 54

4.3. Vapor pressure of strontium 56

4.4. The estimated lifetime of the effusive oven and atomic beam flux as a function of temperature 58

4.5. Sketch of atomic beam passing through a capillary and constricted by downstream nickel gaskets 59

4.6. Model used to estimate expected initial pressures in the vacuum chamber 62

4.7. Photograph illustrating support structure for the trapping chamber . . . 68

4.8. Photograph of the permanent-magnet Zeeman slower 73

4.9. Magnetic field profile experienced by atoms as they pass through the Zeeman slower and into the trapping region 75

4.10. Basic block diagram of lasers required in the cold strontium experiment 77

4.11. Details of the tapered amplifier (TA) chip and housing 79

4.12. Output power of tapered amplifiers as a function of drive current and seed power 83

4.13. Schematic showing how 461 nm blue light is prepared for interaction with strontium atoms 85

4.14. Photograph of a strontium heat-pipe vapor cell 89

4.15. Schematic of frequency-modulation spectroscopy used to stabilize the blue 461 nm and red 689 nm lasers to an atomic reference 92

Figure Page

4.16. Error signal produced in FM spectroscoy of the $5s^2\,{}^1S_0 \longrightarrow 5s\,5p\,{}^1P_1$ "blue MOT" transition in strontium 93

4.17. Error signal produced in FM spectroscoy of the $5s^2\,{}^1S_0 \longrightarrow 5s\,5p\,{}^3P_1$ "red MOT" transition in strontium 94

4.18. Photographs of the helical resonating cans used to amplify RF signals for the EOMs 96

4.19. Overview of electronics used to control RF devices 101

5.1. Schematic of the arrangement of MOT beams for both the top and bottom traps, viewed from the atomic source 104

5.2. Photographs of cold strontium atoms 106

5.3. Control timing sequence used to trap and image the bottom MOT . . . 111

5.4. Example of attempt to subtract the image of the loaded MOT in the blue temperature measurement 112

5.5. Sum of pixel values along columns of CCD images, showing the difference between signal and background images and shot-to-shot fluctuations in MOT brightness 113

5.6. Series of images taken in an attempted temperature measurement of the blue MOT 115

5.7. Integrated pixel values of the series of subtracted images in the blue MOT measurement 116

5.8. Modulating the detuning of the red MOT beams to interact with atoms at blue MOT temperatures 118

5.9. Control timing sequence used to test if the red laser is affecting the atoms 120

A.1. Net scattering force an atom feels from two beams traveling in opposite directions 129

B.1. Relevant energy levels used in trapping and cooling of neutral ^{88}Sr . . . 135

B.2. Vapor pressure of strontium from 300–700°C 137

Figure Page

B.3. Isotopic shifts of the 'blue MOT' $5s^2\,{}^1S_0 \longrightarrow 5s\,5p\,{}^1P_1$ and 'red MOT' $5s^2\,{}^1S_0 \longrightarrow 5s\,5p\,{}^3P_1$ transitions, relative to ^{88}Sr 138

B.4. Expected level shifts of strontium atoms near a perfect conductor 145

C.1. Frequency spectrum of a laser with linewidth γ centered at frequency ω_0 beaten against a single-frequency plane wave with frequency ω_r 153

C.2. Plot of analytical solutions of the photocurrent power spectrum in the delayed self-heterodyne technique for white noise 158

LIST OF TABLES

Table Page

4.1. Maximum temperatures of various vacuum chamber components 65

4.2. Magnet size, location, and strength in the permanent magnet Zeeman slower 74

4.3. List of AOMs used in the experiment 100

A.1. Doppler and recoil temperatures for several atomic species 130

B.2. Reduced dipole matrix elements and total decay rates for transitions of the form $^1\mathrm{S}_0 \longrightarrow ^1\mathrm{P}_1$, originating from the $5s^2$ ground state. 146

B.3. Reduced dipole matrix elements and partial decay rates for transitions of the form $5\mathrm{s}\,5\mathrm{p}\,^3\mathrm{P}_J \longrightarrow 5\mathrm{s}\,N\mathrm{s}\,^3\mathrm{S}_{J'}$ ($N = 6$–10). 146

B.4. Reduced dipole matrix elements and partial decay rates for transitions of the form $5\mathrm{s}\,5\mathrm{p}\,^3\mathrm{P}_J \longrightarrow N\mathrm{p}^2\,^3\mathrm{P}_{J'}$. 147

B.5. Reduced dipole matrix elements and partial decay rates for transitions of the form $5\mathrm{s}\,5\mathrm{p}\,^3\mathrm{P}_J \longrightarrow 5\mathrm{s}\,N\mathrm{d}\,^3\mathrm{D}_{J'}$ ($N = 4$–6). 147

B.6. Reduced dipole matrix elements and partial decay rates for transitions of the form $5\mathrm{s}\,5\mathrm{p}\,^3\mathrm{P}_J \longrightarrow 5\mathrm{s}\,N\mathrm{d}\,^3\mathrm{D}_{J'}$ ($N = 7$–9). 148

CHAPTER I

INTRODUCTION

Atoms are incredibly useful in that all atoms of the same kind are identical. This is more than just a likeness in composition, however, since they share chemical properties and energy spectra as well. This makes atoms nice quantum systems because—unlike solid-state objects like quantum dots or nitrogen-vacancy centers in diamond—they are in some sense immediately well-characterized and predictable. This knowledge of how an atom ought to behave can be leveraged into learning something about its interaction with the environment. Loosely speaking, more can be learned over longer and more controlled observations, and reducing atomic motion is a straightforward way to improve measurement results.

1.1. Precision Metrology with Cold Atoms

In the 1970s—not long after the advent of the laser—physicists became interested in tuning coherent radiation to be resonant with atoms and affect their mechanical motion [1]. Over the course of a couple of decades, the field of cold-atom physics burgeoned into a high-profile and successful arena, and four Nobel Prizes have been awarded for work related to laser-cooled atoms.[1] Such attention was garnered not just because the physics is fundamentally interesting, but also because the resulting cold-atom media are immensely useful. State-of-the-art atomic beam clocks were almost immediately surpassed by atomic fountain clocks [3], and cold samples of atoms significantly decreased the momentum uncertainty in matter-wave interferometers [4].

[1] In particular, trapping and cooling of neutral atoms was developed in the 1980s, and the Nobel Prize lecture of William Phillips should be mandatory reading for anyone remotely interested in the mystery of cooling atoms by shining light at them [2].

Later, the realization of Bose–Einstein Condensates (BECs) [5] enabled long-range coherent interactions, allowing studies of phenomena such as quantized vortices [6] and Mott insulator phase transitions [7].

Metrology is enhanced in cold atomic samples because interaction times are extended, position can be controlled, and slight changes to atomic behavior are more readily detected. Highly sensitive inertial navigation systems [8, 9], magnetometers [10], and electrometers [11] have all been made using cold atoms. Contributions relevant to fundamental physics have also been made, such as measurement of the fine structure constant [12] and searches for the electric dipole moment [13]. Frequency metrology and timekeeping, in particular, have long compelled developments in atomic physics, and recent advances have allowed researchers to directly observe a gravitational red shift by raising an optical table 33 cm [14].

1.2. Cold Strontium

It was with frequency metrology in mind that work began in earnest to cool atomic strontium around the turn of the millennium [15–17]. The groups of Hidetoshi Katori (University of Tokyo) and Jun Ye (University of Colorado at Boulder) pioneered development of optical lattice clocks [18, 19], which offer much lower frequency instability $\delta f/f$ than the microwave transition in a cesium clock. This is because the clock transition is on a doubly-forbidden, ultranarrow transition in the optical regime (where absolute frequency measurement is made possible through optical frequency combs [20]). The results obtained have been astounding, with timing accuracy better than one second out of the age of the universe [21]. Optical lattice clock technology is quite mature, and work toward mobile strontium clocks has been

pursued, with one successfully built inside a car trailer [22] and plans to put one on the International Space Station by 2023 [23].

Strontium has attracted interest aside from timekeeping, however. The spinless ground state and low atom–atom interaction make it an ideal candidate for precision sensing [17], and Guglielmo Tino's group has proposed using it as a tool to search for short-range corrections to Newtonian gravity [24, 25]. They have also compared measurements of ^{87}Sr and ^{88}Sr in a test of the equivalence principle between fermions and bosons, probing the possibility of spin–gravity coupling [26]. Additionally, strontium's narrow-band secondary cooling transition at 689 nm can produce sub-recoil temperatures [27]. These cold traps have enabled BEC production without evaporative cooling, a promising first step toward realizing a continuous atom laser [28].

1.3. Quantum Vacuum Effects

Cold atoms are also appealing as a medium for quantum information processing and quantum sensors, and much effort has been made to miniaturize devices to enhance utility and scalability [29, 30]. The small distances involved, however, mean that quantum vacuum effects become manifest. For example, the lifetimes of neutral atom traps have been observed to decrease significantly for atom–surface separation on the order of a few μm [31]. Another series of experiments demonstrated strong coupling between single cesium atoms and microtoroidal resonators, but found the Casimir–Polder (CP) potential became a significant contributor to coupling dynamics [32].

A better understanding of geometries and materials in such quantum vacuum effects could enable engineering of small-scale devices which mitigate negative effects,

or—perhaps preferably—inspire novel devices whose functionality are based on Casimir and CP potentials. Examples of these include potentially using carbon nanotubes as conductors in atom-chip devices [33] or using nanoscale photonic crystals to create subwavelength vacuum lattices [34].

The contents of this thesis are based on the marriage of the above ideas: the sensitivity of the optical transitions in ultracold neutral strontium make it a reasonable medium for observing CP potentials spectroscopically. Chapter II first explores the origins of mechanical forces due to the quantum vacuum and discusses previous experimental work. After this, the prospects of measuring CP forces using ^{88}Sr atoms in an optical lattice are discussed. Chapters III, IV, and V document the extensive construction and initial loading of a magneto-optical trap (MOT) for strontium, including development of a novel external-cavity diode laser (ECDL), ultra-high vacuum (UHV) system, and stabilized light sources for interacting with the atoms. The appendix includes a brief overview of cooling and trapping of neutral atoms, a reference for some properties of strontium, and a discussion of measuring laser linewidth using the delayed self-heterodyne technique.

CHAPTER II

CASIMIR–POLDER POTENTIALS AND COLD STRONTIUM

2.1. Background

Quantum electrodynamics (QED) is a remarkably successful and complete field theory [35, 36], somewhat appropriately bearing the same moniker as *quod erat demonstrandum*. It provides the mathematical framework to describe the interaction of light and matter, and it has produced accurate calculations of the Lamb shift, the fine-structure constant, and corrections to the electron's magnetic dipole moment [37, 38]. In this chapter, we will be concerned with interactions with the electromagnetic vacuum that give rise to mechanical forces in so-called Casimir, Casimir–Polder (CP), London, or van der Waals (vdW) physics.

To sketch out the basic phenomenon, we begin with a brief overview of QED. The Hamiltonian for the electromagnetic field in the Coulomb gauge is

$$H_{\text{F}} = \int d^3r \left[\frac{\Pi^2}{2\epsilon_0} + \frac{1}{2}\epsilon_0 c^2 (\nabla \times \mathbf{A})^2 \right], \tag{2.1}$$

where $\mathbf{\Pi} = -\epsilon_0 \mathbf{E}$ is the momentum conjugate to $\mathbf{A}$, with $\mathbf{E}$ being the electric field and and $\mathbf{A}$ the magnetic vector potential. By separating the spatial and temporal components, this Hamiltonian is analogous to that of a quantum harmonic oscillator, and a canonical quantization of the electromagnetic field can be performed [36, 39], resulting in

$$H_{\text{F}} = \sum_{\mathbf{k},\zeta} \hbar c |\mathbf{k}| \left(a^\dagger_{\mathbf{k},\zeta} a_{\mathbf{k},\zeta} + \frac{1}{2} \right). \tag{2.2}$$

The $\mathbf{k}$ and ζ indices represent wave vector and polarization states of spatial field modes $\mathbf{f}_{\mathbf{k},\zeta}$, which are populated by the field creation operator $a^\dagger_{\mathbf{k},\zeta}$ (and correspondingly depopulated by the conjugate annihilation operator). The classical field modes are normalized, and the raising and lowering operators obey the commutation relations

$$\int d^3r \; \mathbf{f}_{\mathbf{k},\zeta}(\mathbf{r}) \cdot \mathbf{f}^*_{\mathbf{k}',\zeta'}(\mathbf{r}) = \delta^3_{\mathbf{k},\mathbf{k}'}\delta_{\zeta,\zeta'} \tag{2.3}$$

$$\left[a_{\mathbf{k},\zeta}, a^\dagger_{\mathbf{k}',\zeta'}\right] = \delta^3_{\mathbf{k},\mathbf{k}'}\delta_{\zeta,\zeta'}. \tag{2.4}$$

The creation (and annihilation) operators work in the same way as in the standard harmonic oscillator, but each applies to its own set of modes, including at zero population. That is,

$$a^\dagger_{\mathbf{k},\zeta}|0_{\mathbf{k},\zeta}\rangle = |1_{\mathbf{k},\zeta}\rangle \tag{2.5}$$

applies for *every* field mode vacuum state, and the collective "electromagnetic vacuum" consists of infinitely many unpopulated modes.[1] Since the energies of each oscillator mode are nonzero in the ground state, the terms "zero-point energy" or "zero-point fluctuations" are often used to reference vacuum energy. A summation of the contributions of these vacuum modes in Eq. (2.2) is obviously divergent, and renormalization techniques are needed to make physical predictions.

In a seminal paper in 1948, Hendrick Casimir found that zero-point fluctuations lead to mechanical forces between macroscopic bodies [40]. He considered two infinite, parallel, planar conductors in vacuum, separated by a distance d. The bodies create boundary conditions which define the allowed interior electromagnetic vacuum modes

[1]Spontaneous emission requires the machinery of QED to be understood as an atom coupling to these unpopulated modes through stimulated emission.

$\mathbf{f}_{\mathbf{k},\zeta}$ and their associated frequencies $\omega_{\mathbf{k}} = k/c$. To recover a physical quantity, he compared the total vacuum energy—found by summing $\hbar\omega_{\mathbf{k}}/2$ for the allowed modes—to the energy when $d \to \infty$. Increased separation results in a larger energy because more modes are allowed at low frequencies. The result is then an attractive potential, $V(d) - V(\infty) < 0$, and Casimir found the distance scaling to be d^{-3}. The result can be alternately derived through a more physical interpretation involving radiation pressure, where vacuum field modes can be considered to impart momentum through "virtual photons" reflecting off a surface [41]. Here, regions interior and exterior to the plates are considered, and again there is a discrepancy between the allowed field modes in the two geometries. Consider for simplicity the wave vectors normal to the planes. The lowest allowed frequency between the two planes is $\pi c/d$, but vanishingly small frequencies can exist in the exterior region. The pressure of the modes acting on the bodies is therefore unbalanced, and the plates are pushed together.

2.1.1. Casimir–Polder Potential

Before his result involving macroscopic bodies, Casimir worked with Dirk Polder[2] on the effect of retardation in London–vdW forces between atoms and molecules. In particular, they were intrigued by observations by Verwey and Overbeek in colloidal suspensions [42]. At long distances, the usual z^{-6} scaling (where z is the separation of the particles) did not match measurements as well as a z^{-7} power law. By modeling two atoms as polarizable particles interacting with quantized field modes, Casimir and

[2]Because of the authors of the seminal papers, quantum vacuum effects between macroscopic bodies are called Casimir interactions, while Casimir–Polder (CP) refers to particle–particle or particle–body interplay; broadly speaking, study of the interaction of dispersive objects with electromagnetic fluctuations is referred to as vdW or Casimir physics, but this thesis will reserve the term vdW for referencing near-field CP effects.

Polder confirmed the observed inter-particle potential scaling; they also performed similar analysis of an atom–conductor system, finding that the attractive potential shifted from the vdW z^{-3} behavior to a long-range potential that falls off more quickly at z^{-4} [40]. Roughly speaking, the change in scaling occurs when the separation becomes larger than the dominant atomic transition wavelength. This claim requires some further explanation, but first it is helpful to develop some intuition involving an atom's interaction with the fluctuating vacuum.

Working in the QED formalism defined above, we can calculate the effect of the quantized field interacting with an atom in its ground state and recover the basic form of the CP potential. For an atom with multiple excited levels, the atomic Hamiltonian is given by

$$H_{\mathrm{A}} = \sum_j \hbar\omega_{j0}|e_j\rangle\langle e_j|, \tag{2.6}$$

where $\omega_{j0} = \omega_j - \omega_0 = (E_j - E_0)/\hbar$ is the frequency splitting between the jth excited state $|e_j\rangle$ and the ground state $|g\rangle$. The electromagnetic field Hamiltonian H_{F} is given by Eq. (2.2), and we consider the dipole approximation for the interaction Hamiltonian, $H_{\mathrm{AF}} = -\mathbf{d}\cdot\mathbf{E}$. The quantized electromagnetic field is a sum over spatial modes and their annihilation and creation operators [36, 39],

$$\mathbf{E}(\mathbf{r}) = -\sum_{\mathbf{k},\zeta}\sqrt{\frac{\hbar\omega_{\mathbf{k}}}{2\epsilon_0}}\left(\mathbf{f}_{\mathbf{k},\zeta}(\mathbf{r})a_{\mathbf{k},\zeta} + \mathbf{f}^*_{\mathbf{k},\zeta}(\mathbf{r})a^\dagger_{\mathbf{k},\zeta}\right). \tag{2.7}$$

The atomic dipole operator $\mathbf{d}$ can be written in terms of atomic raising and lowering operators. For an atom in the ground state,

$$\mathbf{d} = \sum_j \left(\mathbf{d}_{ge_j} \sigma_j + \mathbf{d}^*_{ge_j} \sigma_j^\dagger \right), \tag{2.8}$$

where $\mathbf{d}_{ge_j} := \langle g|\mathbf{d}|e_j\rangle$ is the dipole matrix element connecting the ground and jth excited state and $\sigma_j := |g\rangle\langle e_j|$ is the atomic lowering operator.

The total Hamiltonian is thus $H = H_{\rm A} + H_{\rm F} + H_{\rm AF}$, and to find the CP shift due to the interaction with the vacuum field we treat $H_{\rm AF}$ as a perturbation. The first-order correction $\langle g|H_{\rm AF}|g\rangle$ is zero because of the atom raising and lowering operators, so we calculate to second order:

$$V_{\rm CP} = \sum_j \sum_{\mathbf{k},\zeta} \frac{|\langle g,0|H_{\rm AF}|e_j,1_{\mathbf{k},\zeta}\rangle|^2}{E_{g,0} - E_{e_j,1_{\mathbf{k},\zeta}}}. \tag{2.9}$$

The interaction Hamiltonian has four terms which go as $\sigma_j a^\dagger_{\mathbf{k},\zeta}$, $\sigma_j^\dagger a_{\mathbf{k},\zeta}$, $\sigma_j a_{\mathbf{k},\zeta}$, and $\sigma_j^\dagger a^\dagger_{\mathbf{k},\zeta}$. The latter two of these combine to produce the only non-vanishing term in the numerator of Eq. (2.9):

$$\frac{\hbar\omega_{\mathbf{k}}}{2\epsilon_0} \big\langle g,0 \,\big|\, \mathbf{d}_{ge_j} \cdot \mathbf{f}_{\mathbf{k},\zeta}\, \sigma_j a_{\mathbf{k},\zeta} \,\big|\, e_j, 1_{\mathbf{k},\zeta} \big\rangle \big\langle e_j, 1_{\mathbf{k},\zeta} \,\big|\, \mathbf{d}^*_{ge_j} \cdot \mathbf{f}^*_{\mathbf{k},\zeta}\, \sigma_j^\dagger a^\dagger_{\mathbf{k},\zeta} \,\big|\, g,0 \big\rangle. \tag{2.10}$$

This is notable for a couple of reasons. First, these two combinations of atom and field raising and lowering operators are usually discarded in the rotating-wave approximation (RWA) because they are the counter-rotating terms [39]. They also violate conservation of energy when considered individually—for example, $\sigma_j^\dagger a^\dagger_{\mathbf{k},\zeta}$ both raises the atomic state *and* adds a photon to the field—however, when both sets of operators are combined there is no net energy change. This process is sketched in the

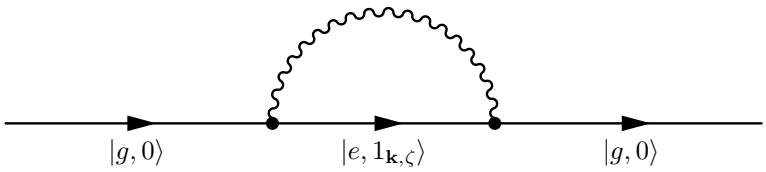

FIGURE 2.1. Feynman diagram of an atom in its ground state interacting with the electromagnetic vacuum field. As the atom is excited a photon is created in field mode $\mathbf{f}_{\mathbf{k},\zeta}$. The photon is later annihilated as the atom drops to the ground state.

Feynman diagram in Fig. 2.1. The interpretation is that the atom 'emits' a virtual photon into the vacuum mode before 'absorbing' it a short time later.

The energy difference in the denominator is $E_0 - E_j - \hbar\omega_{\mathbf{k}}$, so the CP potential is then

$$V_{\text{CP}} = -\sum_j \sum_{\mathbf{k},\zeta} \left(\frac{\hbar\omega_{\mathbf{k}}}{2\epsilon_0}\right) \frac{|\mathbf{d}_{ge_j} \cdot \mathbf{f}_{\mathbf{k},\zeta}|^2}{\hbar\left(\omega_{j0} + \omega_{\mathbf{k}}\right)}. \tag{2.11}$$

From here, the calculation requires the explicit field modes for a given geometry. Such calculations are difficult because $\mathbf{f}_{\mathbf{k},\zeta}$ are nontrivial for even relatively tame geometries. Furthermore, Casimir and CP forces are non-additive [43] because the addition of extra matter fundamentally alters the field modes.[3] A physical (non-infinite) potential is found by subtracting the CP shift the field induces on the atom in free space (the limit where geometric structures influencing the field modes are far away from the atom). Using Fig. 2.1 again for intuition, the physical CP potential can loosely be thought of as the collection of second-order processes where the virtual photons interact with surrounding objects—those that do not 'see' the geometric influences will be canceled under renormalization. This idea is evident in numerical

[3]In fact, this is how some of the hallmark results can be obtained: the Lamb shift can be found as the energy change in the free-space vacuum modes when a single atom is added; and modification from adding a second atom results in the London and CP attractive potentials [36].

worldline techniques, which only count the energy contribution of Monte–Carlo paths that intersect surfaces [44–46].

In the planar conductor geometry considered by Casimir and Polder (where the atom is displaced by $z\hat{z}$ from the conductor in the x-y plane), we insert half-space quantization modes [36] into Eq. (2.11) and the sum can be carried out analytically. For a spherically symmetric atom in the ground state, the result is [39]

$$V_{\rm CP} = -\frac{1}{4\pi\epsilon_0}\frac{1}{4\pi}\sum_j |\langle g|\,\hat{z}\cdot\mathbf{d}\,|e_j\rangle|^2 \left[\partial_z^2\,\frac{1}{z}\,f(2\omega_{j0}z/c)\right], \tag{2.12}$$

where $f(a)$ is one of the auxiliary functions of the sine and cosine integrals,

$$f(a) = \sin a\,\mathrm{Ci}(a) + \cos a\left[\frac{\pi}{2} - \mathrm{Si}(a)\right], \text{ and} \tag{2.13}$$

$$\partial_a f(a) = -g(a) = \cos a\,\mathrm{Ci}(a) - \sin a\left[\frac{\pi}{2} - \mathrm{Si}(a)\right]. \tag{2.14}$$

In the short-distance limit, $f(a) \to \pi/2$, and the resulting z^{-3} scaling is identical to the simple case of an atomic dipole interacting with its image [36]. Even though the atom is in its spherically symmetric ground state and $\langle g|\mathbf{d}|g\rangle = 0$, the second-order dipole moment $\langle g|d^2|g\rangle$ is non-vanishing. This means that fluctuations in the vacuum field that give rise to the CP potential can equivalently be cast as fluctuations in the atomic dipole, which is implied by the vertices in Fig. 2.1.

Equivalence of the CP result with the vdW scaling breaks down as the distance between the atom and conductor is increased. Mathematically, this is clear from the auxiliary functions decaying with increasing z. The retarded interaction of the fluctuating dipole and its image provide a more physical explanation: If the oscillation period of the fluctuating dipole is short compared to the amount of time it takes to exchange information with its image, then the two become uncorrelated and the

attraction is reduced.[4] In fact, the correct long-range potential can be derived in a semiclassical treatment in this manner, but a normal ordering of the fields must be invoked, thus implying the fundamentally quantum mechanical nature of the effect [47]. We can also corroborate our intuition from the retarded dipole interaction by considering the picture of an atom emitting virtual photons. An individual event only contributes to the CP potential if the time period of the brief violation of conservation of energy encompasses the time it takes the photon to leave the atom, interact with the mirror, and return.

Thus the important timescale for an atomic transition is $2z/c = 2\pi/\omega_{0j} = \lambda_{0j}/c$, which of course is implied by the argument of the auxiliary function in Eq. (2.12). Also important, however, is the strength of the dipole moment connecting $|g\rangle$ to $|e_j\rangle$. For reference, the strongest, lowest-frequency resonance of an atom is typically ~ 1 μm, so the crossover will occur at distances smaller than this. The ground-state level shift for strontium—whose strong cycling transition is at 461 nm—is pictured in Fig. 2.2 along with the near- and far-field approximations. At a few hundred nm, the scaling behavior of the exact solution noticeably deviates from the z^{-4} long distance behavior. Additionally, it is interesting that the vdW dipole-dipole energy does not correctly predict the actual shift except at extremely small distances, so the classical static intuition is really only useful for understanding the scaling.

2.1.2. Previous Experimental Approaches

At the end of his famous paper, Casimir estimates the size of the attractive force he calculated. He then proceeds to significantly *under*estimate the impact

[4]Even if ignoring orientations of the dipoles, the magnitudes are uncorrelated and the product of the dipole and its image is on average smaller than in the instantaneous case, $\langle d_{\rm atom}(t) d_{\rm image}(t-\tau)\rangle \leq \langle d_{\rm atom}(t) d_{\rm image}(t)\rangle = \langle d^{\,2}_{\rm atom}(t)\rangle]$.

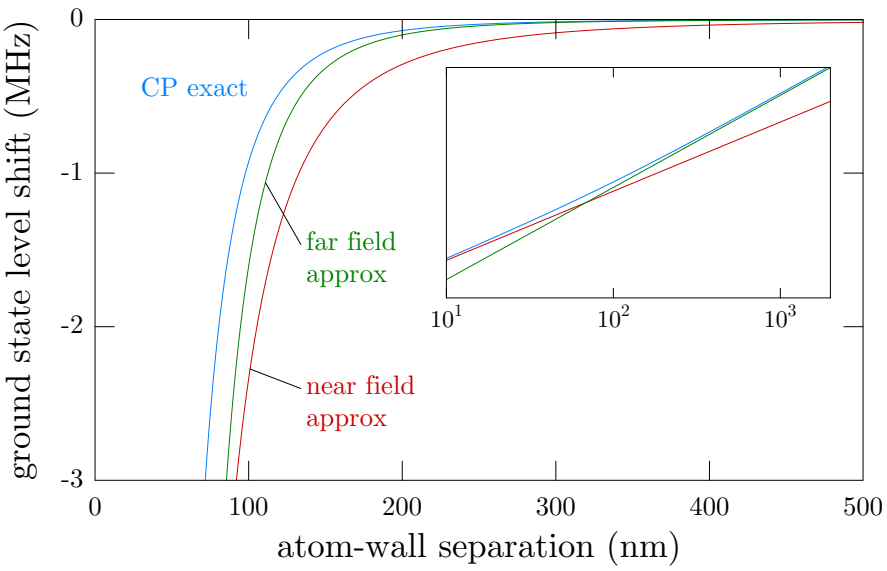

FIGURE 2.2. Level shift of the ground state of strontium near a perfectly conducting plate. The inset shows the same curves on a logarithmic scale, extending the range to 10 nm separation. Small- and long-distance limits of Eq. (2.12) illustrate the transition that occurs between roughly 10 nm and 1000 nm.

of his work, musing, "This force may be interpreted as a zero point pressure of electromagnetic waves. Although the effect is small, an experimental confirmation seems not unfeasable [*sic*] and might be of a certain interest" [40]. Since then, the field of Casimir and vdW physics has become vibrant and important, overlapping with many disciplines, including atomic physics, condensed-matter systems, surface chemistry, and structural biology. As such, this thesis will only provide selective, brief overviews of landmark achievements; more complete discussion is detailed in numerous books and review articles [48–52].

In practice, understanding Casimir and CP potentials for real bodies is quite difficult, and for a field of physics that is seventy years old, analytic solutions are few and far between. In the years following Casimir's original result, Lifshitz generalized the theory to accommodate arbitrary bodies at finite temperature [53, 54], but the dielectric permittivity and magnetic permeability must be well-characterized at all

frequencies. Thus, writing down the field modes $\mathbf{f}_{\mathbf{k},\zeta}$ is not just a geometric problem, but also one of materials, which builds additional model-based complications into predictions regarding Casimir and CP forces. Luckily, experimental progress has been steadily growing in the past three decades, which can be helpful in addressing questions about appropriate theoretical models [55].

Remarkably, accurate demonstration of Casimir's parallel plate prediction was not achieved for fifty years. The reason for this long delay was the technical difficulty in realizing a clean, charge-free system with parallel surfaces. In the end, experiments became feasible using a sphere to approximate one of the bodies as an infinite plane at the point of closest approach [56] (parallel plate experiments have since been performed—albeit with relatively poor accuracy [57]). This technique opened the door for sphere–plate experiments in micro- and nano-electromechanical systems (MEMS and NEMS), including the use of atomic-force microscopy [58] and small-scale torsional oscillators [59]. The latter became somewhat of a model system and allowed investigation into reducing the Casimir force through thin-film metallic skin depth effects [60] and nanostructured materials [61, 62]. Researchers in Ref. [63] demonstrated a repulsive interaction when adding a layer of bromobenzene between a silica surface and gold sphere (where the permittivities satisfy $\varepsilon_{\mathrm{g}} > \varepsilon_{\mathrm{b}} > \varepsilon_{\mathrm{s}}$, thus meeting the repulsive criteria found in Ref. [54]). The flurry of macroscopic Casimir experiments have (not coincidentally) occurred alongside progress in MEMS and NEMS technologies. As devices are miniaturized there is great interest in leveraging understanding of the Casimir effect in engineering new devices and mechanisms; circumventing negative effects of bodies irrevocably bonding together through Casimir-induced "stiction" has long been a goal of research [64, 65], but novel arrangements, like low-power Casimir-force switches [66], are also tantalizing.

In a recent proposal, the Casimir effect is used to control an optical switch based on optomechanically-induced transparency (OMIT) [67].

While macroscopic Casimir experiments have largely been achieved by sensitively measuring slight deflections of bodies which are brought close together, their CP counterparts have had to be creative in extracting surface potentials through dynamical interaction of atomic systems. One subclass of CP experiments uses atomic beams traveling past surfaces [68–70]. The seminal result of Ref. [71] confirmed both vdW and CP scaling by passing a beam of sodium atoms through a gold-coated groove. By focusing an ionizing laser through the beam at the output (and then counting the ions with an electron multiplier) they could monitor the 'opacity' of the channel as a function of plate separation. Other hot-atom experiments have found success in the vdW regime. Atoms passing through transmission gratings pick up a small phase change which can be detected through atomic-beam interferometry [72, 73], and this effect has been used to detect the increase in attraction from adding a thin gold layer to a silicon-nitride grating [74].

Cold-atom approaches have also been developed. In a series of admirable experiments, the Cornell group measured the influence of a surface on a Bose–Einstein condensate (BEC) of ^{87}Rb atoms [75]. By bringing a magnetically trapped, cigar-shaped BEC near a surface, the researchers could accurately measure CP perturbations to the harmonic potential. This system provided good signal from 6–12 μm, allowing them to study temperature dependence of the CP force [76]. They also investigated sensitivity to surface patch potentials (caused by rubidium atoms adsorbed onto the surface), concluding that short-range investigations are likely difficult in this system [77]. Another host of experiments use quantum reflections of atoms off of CP surfaces potentials [78–83]. Such an experiment provided the first

measurement of CP forces in the intermediate distance regime [84] using a well-characterized evanescent field at the surface of borosilicate glass to tune the effective turnaround point for cold rubidium atoms.

Finally, a class of spectroscopic experiments have also been pursued. By using a two-laser scheme to probe an excited transition (where the CP shifts are larger than for the ground state), changes in the resonance have been probed in an atomic-beam experiment [70] and in atomic vapor cells [85–87] in the vdW regime. Recently, this technique has demonstrated an increase in the attraction between cesium and sapphire with increasing surface temperature [88].

2.2. Strontium Atoms as Casimir–Polder Detectors

The atomic physics approaches outlined above have been impressive in their ability to sense CP forces, particularly in the near-field vdW regime. Absent, however, is a spectroscopic approach with atoms which are a controllable distance away from the surface. Current spectroscopic techniques have some drawbacks. The results in Ref. [88] rely on a surface-reflection measurement using a probe laser, which is sensitive to shifts in the atomic energy levels in the vapor to a penetration depth of roughly $\lambda_{\text{probe}}/2\pi \sim 100$ nm. The varying thickness of the "nanocell" used in Ref. [87] allows some control of the distance of the atoms sampled, but the information obtained by the surface reflection is ultimately model dependent. There is also some extra uncertainty since the transition probabilities are not well characterized in these excited state optical transitions [88].

A useful addition to the class of spectroscopic measurements of the CP potential would therefore be a *direct* measurement of an atomic transition. In particular, ultracold atoms with a well-characterized transition would provide detailed

observation of surface potentials without the need to assume a particular theoretical comparison. Strontium is a good candidate for such a measurement because its optical "clock" transitions are extremely narrow and well-characterized. The sub-Hz accuracy obtained in Ref. [89] was limited by the interrogation laser's linewidth, and such frequency resolution would easily probe CP-sized shifts (compare to Fig. 2.4, for example).

In addition to the narrow linewidth, strontium offers other benefits over alkali atoms, especially in the variety of surfaces it can probe. Thermal excitations in metallic surfaces have been shown to be a significant source of loss in atom traps, since small fluctuations in the magnetic field can drive oscillations of atoms which are resonant with the trap's fundamental frequency. Ion traps are strongly susceptible to this effect—where significant loss is incurred even tens of micrometers away of a surface—and neutral atoms with spin are affected at the $\sim\mu$m scale [90]. This was studied by the Cornell group shortly before they began work in their BEC–surface CP experiments, where they were exploring the feasibility of microtraps of ^{87}Rb involving current carrying wires [91]. In contrast to the $5^2S_{1/2}$ ground state of ^{87}Rb, the nuclear-spin-free ^{88}Sr has a spinless ground state that is decoupled from the thermal fluctuations [90], making trapping more convenient in close proximity to a metallic surface. A more considerable limitation on the Cornell BEC experiments, however, was the effect of stray patches of charge from adsorbed atoms ("adatoms") on the surface. Roughly speaking, adatoms on a metal are slightly ionic because the valence electron penetrates into the surface, creating a dipole-like separation—in the case of Rb—of roughly 0.5 nm. These charges created potentials of $1/r^2$ for titanium (conductor) and $1/r^{2.3}$ for silicon (semiconductor) [77], so the CP measurements had to be carried out with fused silica and sapphire [91]. Strontium adatoms, on the

other hand, should be much less ionic in character because its ionization energy is larger than the work function of most materials [77], opening the door to probing both metals and insulators. Furthermore, a spectroscopic method of detection (in contrast to the BEC center-of-mass method) does not require as great a number of atoms, and surface contamination would be largely reduced.

Finally, cold strontium is a promising medium for probing CP potentials because of extensive recent work on the optical lattice clock. In addition to detailed spectroscopy knowledge, frequency-measurement systematics are extremely well characterized [89] or have been eliminated altogether. Supreme among these is the ability to circumvent spatial-dependent ac Stark shifts in an optical trap by using the "magic wavelength" of the clock transition [92], which is central to the proposed measurement scheme discussed below.

2.2.1. Optical Lattice Technique

Cold strontium is thus well-suited to use in CP measurements, but we need to be able to confine it in a reasonably small cloud next to a test surface. A focused dipole trap could be used to trap atoms and move them near the surface, but trap widths are typically many μm in the radial direction and even larger axially [93]. An optical lattice, on the other hand, provides steep changes in potentials that hold atoms in very well-defined positions along the beam's axis. If we orient the lattice normal to the surface, then a single lattice site would provide good spatial resolution of the atom–surface separation, but we would need to be able to sample various distances to make a useful measurement. Forming the lattice by retro-reflecting a beam from the surface is problematic because atoms can only be trapped at positions $z = \lambda_{\mathrm{L}}/4 + n\lambda_{\mathrm{L}}/2$. A basic requirement of using cold strontium in such a configuration, therefore, is that

the test surface be at least somewhat transparent to the optical lattice wavelength. This way one of the lattice's beams comes from behind the surface, and the trapping regions can be positioned at arbitrary z.

The frequency at which the test surface is transparent is a stringent condition, however, because the wavelength of the optical lattice is not negotiable. In an optical field, the total shift of an energy level in an atom is found by summing the ac Stark shift from all dipole-allowed transitions connected to that state, and in general the ground and excited states of a particular transition will not shift by the same amount. Because of the varying intensity in a lattice potential, the differential shift depends on position, which would complicate the search for a small frequency shift in a CP measurement. Fortunately there are particular wavelengths at which the shifts of the two levels are identical. Such magic wavelengths occur at 813.428(1) nm for the $5s^2\,{}^1S_0 \longrightarrow 5s5p\,{}^3P_0$ transition in ^{87}Sr used in the optical lattice clocks [92], and at 914(1) nm for the $5s^2\,{}^1S_0 \longrightarrow 5s5p\,{}^3P_1$ intercombination line in ^{88}Sr [94]. By operating our trapping laser at a magic wavelength, the differential ac Stark shift is eliminated, and all atoms within the trap will have the same resonant frequency for the transition we want to interrogate.

To shift the location of the trapped atoms and probe different z, we propose direct translation of the lattice via a linear air-bearing translation stage (Aerotech ABL10100-LT), which was used in previous, one-way barrier experiments with rubidium in our lab [95]. The resolution of this stage is 5 nm, and it has a repeatability of 50 nm, meaning that atoms could be repositioned reasonably well as data are recorded. Atoms can be loaded from a MOT far away from the surface before they are moved into position for the CP measurement, which greatly reduces the risk of unwanted adatom contamination on the test surface. Note that the nearest the

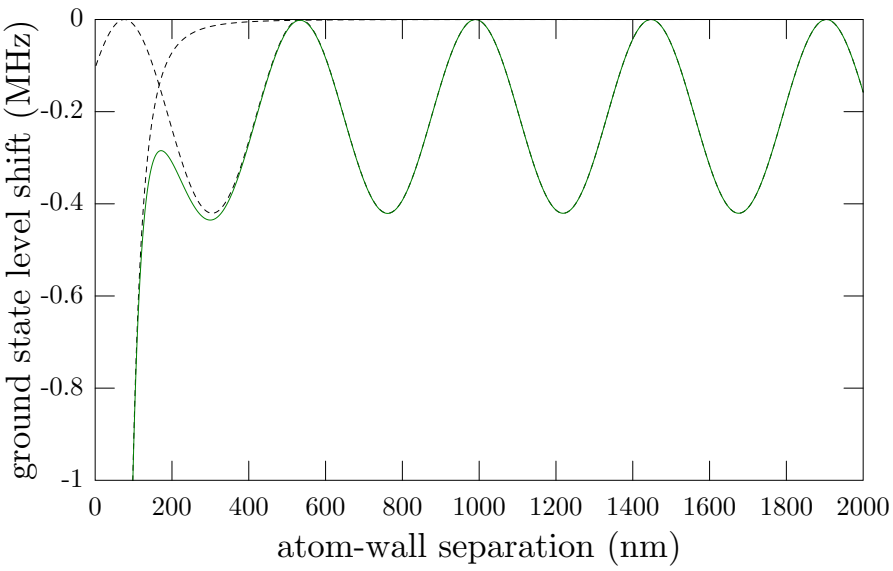

FIGURE 2.3. Trapping potentials of the optical lattice and the CP effect, plotted both individually (dashed) and combined (solid green). Here the lattice has a depth of 22 μK, corresponding to a power of 380 mW and a waist of 50 μm. At close range, the strength of the CP potential overwhelms the confining potential of the lattice, placing a lower limit on achievable atom–surface separation.

atoms can be brought to the surface before getting pulled out of the lattice is roughly 200 nm, as shown in Fig. 2.3 for a trapping depth of 22 μK.

2.2.2. Feasibility

The spectroscopic measurement is an interrogation of the frequency separation of the ground and excited states, and we therefore are only sensitive to the *differential* CP shift of the two states. The generalization of Eq. (2.12) for an excited state is identical for vacuum-couplings to higher-lying states, but is modified for lower-lying states. This is because in the perturbative calculation the dipole interaction induces the atom to emit additional "real" photons which reflect off the surface and are reabsorbed. The modification of Eq. (2.12) adds oscillatory terms which are consistent with a dipole radiating near a mirror [39].

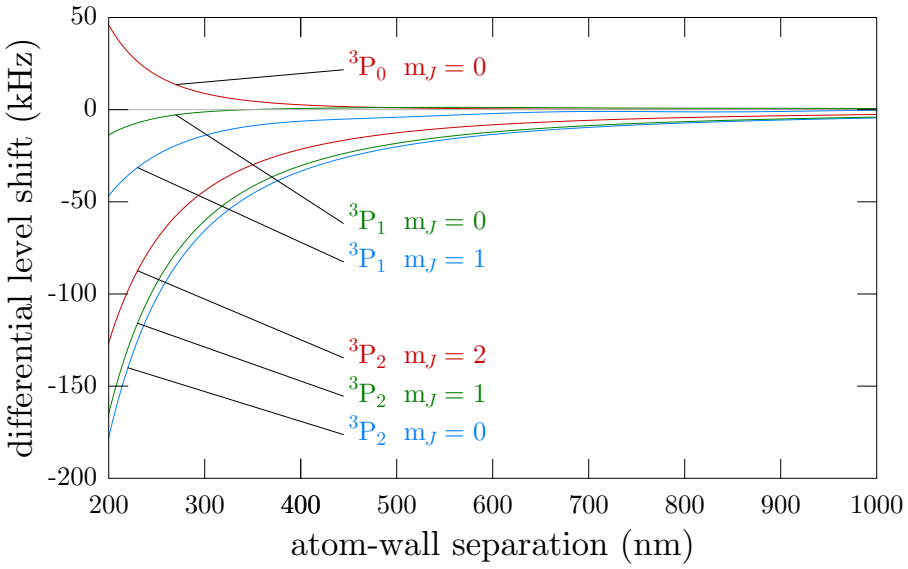

FIGURE 2.4. Expected differential level shifts between the ground state and various excited states in strontium. Shifts of a particular level are computed by assuming an infinite planar conductor and summing over dipole-allowed atomic transitions (see Appendix B).

CP potentials for various energy levels in Sr are calculated by summing over dipole-allowed transitions, and the differences in the ground- and excited-state shifts are shown in Fig. 2.4. These are computed using the generalized version of Eq. (2.12) derived in Ref. [39], and details about calculating the various dipole matrix elements are discussed briefly in Appendix B. The differential shift is largest for the $^3P_2$ excited states, but at 200 nm—where the lattice trap begins to break down—the shift of the $^3P_1$ state is roughly 50 kHz for magnetic sublevel $m_J = 1$. Such a shift can be resolved by the 7.6-kHz-wide intercombination line, and a first generation of experiments can interrogate the potential using the same laser used to make a red MOT (see Chapters IV and V) and a magic wavelength lattice operating at 914 nm.

Probing the CP shift at a particular distance will require many repetitions of loading and translating the lattice and performing a spectroscopic interrogation. Since the absorption of the narrow transition is so small (I_{sat} is only 3 μW/cm^2), the

interrogation procedure will consist of a $\pi/2$ pulse on the 689-nm line followed by a measure of the ground state population using a resonant 461-nm beam. By varying the detuning of the interrogating laser, the transition's lineshape can be mapped out, so shifts in the resonant frequency can be sensed well below the 7.6-kHz width of the transition.

2.2.3. Outlook

Demonstrating the viability of this lattice-based approach would add diversity to atom–surface CP experiments. In particular, this method would join the reflection experiments of Ref. [84] as a measure of intermediate distances where the CP potential departs from the far-field z^{-4} scaling. Moreover, the cold-strontium technique is more amenable to a variety of surfaces than previous experiments, with the only real requirement being that the test surface is somewhat transparent at the lattice wavelength and that it does not significantly distort the beam.

The remainder of this thesis discusses the development of an apparatus to provide a cold-strontium source for such CP experiments. The first proof-of-principle experiment will be performed using a pyrex vacuum cell as the interaction surface. In addition to investigating a variety of surfaces, subsequent evolution of the project would add the ability to interrogate the true $^3P_0$ clock transition, providing orders of magnitude higher sensitivity to the CP potential.

CHAPTER III

NOVEL EXTERNAL-CAVITY DIODE LASER

Diode lasers, as semiconductor devices, benefit from manufacturing techniques driving computing technology, making them fairly cheap to produce in large quantities. They are also highly efficient and compact, greatly simplifying the overhead needed to furnish a laser lab. They have become the lasers of choice in modern atomic physics laboratories [96–99] because the linewidth can be made narrow relative to an atomic transition and the frequency is easily tuned and controlled.

Discussion of a laser's linewidth typically begins with the Schawlow–Townes linewidth $\Delta\nu_{\mathrm{ST}}$, which is a result of phase fluctuations from spontaneous emission into the laser mode [100]. In diode lasers, however, phase fluctuations in the gain medium can alter the carrier density, causing fluctuations in both amplitude and optical path length [101]. The result is a broadening of the laser linewidth via β, a "cavity enhancement factor" [102, 103], which typically has values between 2 and 8 [101]. The modified Schawlow–Townes linewidth of a laser diode operating at frequency ν is then

$$\Delta\nu_{\mathrm{LD}} = \Delta\nu_{\mathrm{ST}}(1+\beta^2) = \frac{h\nu g n_{\mathrm{sp}} \left(\Delta\nu_{\mathrm{C}}\right)^2}{P_0}\alpha_t \left(1+\beta^2\right), \tag{3.1}$$

where h is Planck's constant, g is the gain, n_{sp} is the number of spontaneous emission events, P_0 is the power in the mode, α_t is the cavity loss, and $\Delta\nu_{\mathrm{C}}$ is the cavity bandwidth [98]. Typically, linewidths of laser diodes are 20–50 MHz [97], and need to be narrowed before interacting with atomic transitions. The enhancement factor is an obvious source of broadening, but it is fundamentally determined by the diode's

semiconductor composition and is thus difficult to alter. The linewidth can, however, be narrowed by improving the quality factor Q of the lasing cavity. To lowest order,

$$Q = \frac{\nu_{\mathrm{C}}}{\Delta\nu_{\mathrm{C}}} = -\frac{l}{\Delta l} \tag{3.2}$$

in an optical cavity [104], and the laser's linewidth is then inversely related to the square of the length of the cavity. This means that the linewidth of a diode laser (which has a cavity length of only a few hundred μm) can be narrowed considerably by creating a much longer 'external-cavity diode laser' (ECDL), where a reflective optical element overrides one of the diode's output facets and acts as a cavity mirror [105, 106]. Extending the length too far does have drawbacks, however. Longer lasers are more sensitive to mechanical vibrations (see Sec. 3.1), and significant reduction in the cavity's free spectral range makes mode hops between closely spaced cavity modes more likely to occur.

Typically, a frequency-selective element is also used so the diode's frequency output is not only narrowed, but tunable as well. A simple and common way to create a tunable ECDL is through the use of a diffraction grating in the Littrow configuration, as pictured in Fig. 3.1.[1] The laser's two cavity mirrors are formed by the diode's rear facet and the grating. First-order diffracted light is fed back into the laser-diode gain medium, allowing coarse tuning of the cavity's resonant frequency through rotation of the grating. Fine tuning is controlled with a piezoelectric device

[1] An alternative popular ECDL design uses a "cat's-eye" configuration, which focuses the cavity mode onto a mirror. An interference filter within the cavity can be tilted to coarsely select the operating wavelength [107–109]. Such a design is attractive because mechanical stability of the tuning and feedback elements are, in principle, not as paramount to frequency stability as in a grating-feedback configuration. It can be argued, however, that the narrow linewidths achieved in the cat's-eye designs are a result of the long cavity lengths needed to fit the necessary optical components.

placed behind the grating, and laser frequency is stabilized via electronic feedback to the piezo. These grating-stabilized ECDLs are found in virtually all atomic physics laboratories, and it is not uncommon that they are built in-house [110–113].

Constructing a new strontium experiment requires a variety of laser systems (four in our case, including one for the particularly narrow 7.6 kHz intercombination line, see Sec. 4.2), and we decided it was worth the effort to create a new Littrow-configuration ECDL design. In particular, we wanted to surpass the passive stability achieved by the previous generation of lasers built in our lab [95, 114, 115], and, if possible, produce lasers which were competitive with high-end commercial products. We have achieved these goals, published the results [116], and made our design freely available to the atomic-physics community (including machine drawings and step-by-step pictorial construction instructions [117]). Since our publication is fairly comprehensive, the current chapter will not be concerned with reproducing that content in its entirety, but will instead cover major highlights and fill in gaps which add to the utility and discussion of the design.[2]

3.1. Stabilizing Cavity Length

As is apparent from combining Eqs. (3.1) and (3.2), the frequency stability of a diode laser can be severely impacted by mechanical instability in the length of the external cavity. A change in length can happen slowly (drifts in pressure, humidity, or temperature) or on faster timescales (mechanical vibrations or current-induced changes in the diode's index of refraction). Whatever the cause, if a displacement is large enough, stabilization electronics will eventually fail. Low-frequency resonances are particularly concerning, because these can limit the frequency bandwidth of the

[2]Another useful resource is the undergraduate thesis of Erica Mason [118], who thoroughly documented the process of constructing the laser without our assistance.

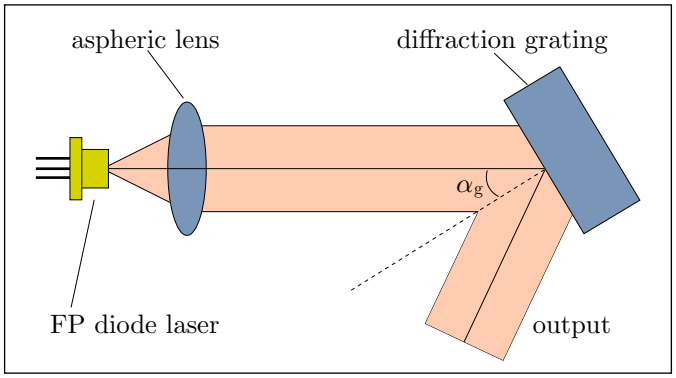

FIGURE 3.1. Sketch of a Littrow-configuration ECDL. The output of a Fabry–Pérot (FP) diode laser is collimated by an aspheric lens before being reflected by a diffraction grating. The first-order mode is reflected back at angle α_g into the laser diode, and the zeroth-order is the usable output.

electronic servomechanism if no special compensation is designed into the controller. In a Littrow-geometry ECDL, though, tuning is fundamentally achieved by physically moving the diffraction grating, and a main challenge is simultaneously implementing mobility while retaining rigidity.

Our approach is similar in spirit to that of Carl Wieman's group [119]: by carving the laser cavity out of a monolithic block of aluminum, the cavity length is better isolated from external vibrations. Sensitivity to background noise is additionally ameliorated (it is, of course, impossible to remove effects of all background noise, since it diverges at low frequency [120]) by increasing the fundamental vibrational resonance of the arm which moves the diffraction grating. Ideally, the resonance should be higher than most lab acoustic noise, whether it is generated by cooling fans, discoursing scientists, or clumsy graduate students.

3.1.1. Diffraction Grating Arm

A simple arm with a symmetrically notched hinge—formed by carving two semicircular channels into a cantilever—can have a relatively high fundamental

frequency while allowing deflection from a piezoelectric stack (we use Noliac SCMAP02/S2/A/5/5/10/60/10.6/1000, which has a blocking force of 1000 N). A finite-element analysis [121] yields an empirical formula for the torsional constant of the hinge,

$$\kappa = \frac{Eht^3}{24KR}, \tag{3.3}$$

where E is the elastic modulus of the material (68.9 GPa in 6061-T6 aluminum), h is the height of the hinge, t is the minimum thickness of the hinge, R is the radius of the semicircular channel, and the factor K is determined from the approximate formula $K = 0.565\,t/R + 0.166$. In the case of a rectangular bar (of length l and width w) attached to such a hinge, the resonant frequency is

$$f = \frac{1}{2\pi}\sqrt{\frac{\kappa}{I}} = \frac{1}{2\pi}\sqrt{\frac{t^3}{2KRwl(w^2+4l^2)}}. \tag{3.4}$$

Note that the height of the hinge cancels out for objects whose moments of inertia I are proportional to h (anything with a uniform cross section through the height of the arm). We constructed a sample flexure using a $0.25''$ ball-end mill to carve out a notch of thickness $0.09''$. For an aluminum (density 2770 kg/m^3) arm of length $l = 1.25''$ and width $w = 0.25''$, the calculated resonance frequency was $f \sim 1700$ Hz, consistent with the measured $f \sim 1520$ Hz.

The final laser design uses a grating arm with dimensions similar to this simple case. To increase the resonant frequency, however, much of the material in the arm is removed, as shown in Fig. 3.2. Four 2-56 clearance holes are counterbored through almost the entire height of the arm, allowing the arm to be attached to a support base during machining. Eight additional holes are drilled through the arm and the

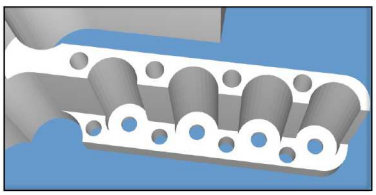

FIGURE 3.2. A rendering of the diffraction grating arm, which rotates via a notch-hinge flexure at left. Mass is removed to increase the fundamental resonance frequency.

front half is mostly removed. We also use a custom-sized grating (6 mm tall, 12 mm long, and only 3 mm deep) to minimize the mass we add to the end of the pendulum.

Plucking the arm in a constructed laser body (with no grating attached) produces a 2.05 kHz tone. The target Littrow grating angle is 45°, but the arm is machined at an angle of 43°, and must be pushed from behind by piezo and coarse adjust screw to be "loaded" into final position. The support from the piezo and coarse adjust screw significantly increases the frequency of the fundamental resonance (see Sec. 3.2). Care should be taken to avoid deflecting the arm too far past the desired operational point and fatiguing the aluminum [118]. Using an expression for the maximum yield stress [121], we estimate that angular deflections beyond $\sim 0.3°$ will begin to enter this regime, so it is best to monitor the laser's wavelength during initial alignment of the cavity and have a reasonable expectation for the laser's output direction. Note that this is especially true when using a shim behind the grating (Sec. 3.4.1) because the angle provided by the shim is somewhat difficult to control.

3.1.2. Laser Diode Current Source

As mentioned earlier, frequency fluctuations in a diode laser can be caused by changes in charge-carrier density due to noise in the supply current. This effect turns out to be significant, and—if unchecked—can actually be the dominant contributor

do a diode laser's linewidth. While making preliminary stability measurements of a prototype of the ECDL, we powered the diode using a homebuilt current source (based on Ref. [122] and discussed in Ref. [123]; output current is driven by a pair of BUF634 op-amps which are regulated by a proportional–integral [PI] servo monitoring the voltage dropping over a sense resistor). As shown in Fig. 3.3, the current supply has an obvious noise bump around 400 kHz in its power spectrum, and this is imprinted on the frequency noise spectrum of the laser and broadens its linewidth significantly. Using a $f_{3\mathrm{dB}} = 15$ Hz low-pass filter on the circuit's output corrects this behavior, but hampers the practicality of the controller by disallowing current modulation. Instead, it is best to use a low-noise circuit, such as a Libbrecht–Hall-style controller [124, 125], which cleverly pairs a low-noise op-amp and metal-oxide-semiconductor field-effect transistor (MOSFET) to regulate the current. Incidentally, the laser's sensitivity to current noise enabled our collaborators to uncover an issue with the Libbrecht–Hall design operating near its current limit, and this led to a joint publication about simple ways to make improvements [126].

3.1.3. Additional Measures

We make several efforts to further stabilize the length of the laser cavity, as shown in the assembly drawing of our ECDL in Fig. 3.4. The main laser-cavity area is carved from a 1″-thick piece of 6061-T6 aluminum, and a separate block—which holds a Thorlabs LT230P-B diode-collimation tube—is secured into the side to define one end of the lasing cavity. A diffraction grating is glued to the notched-hinge arm to complete the cavity. The main body has a top and bottom lid, and the stack is actively temperature-controlled with two thermoelectric coolers (TECs) in series. Temperature is monitored at the diode to have control over the gain curve,

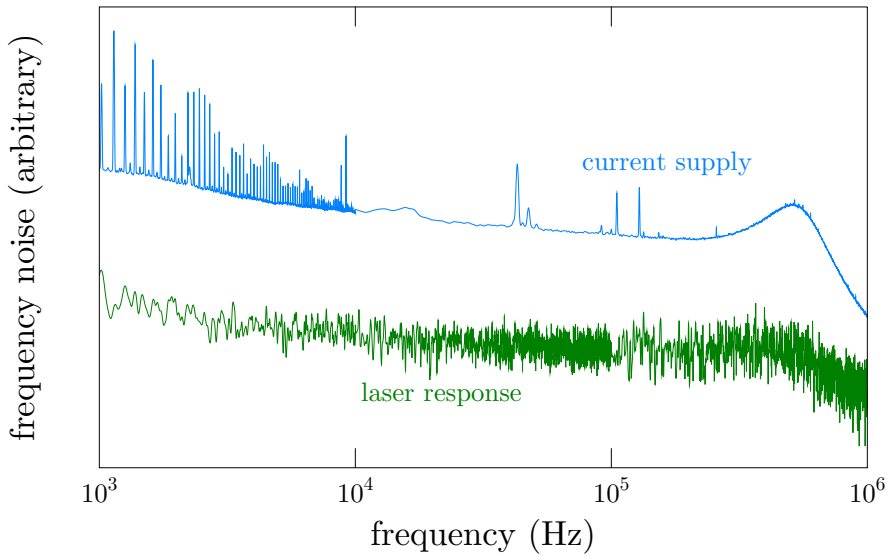

FIGURE 3.3. Laser susceptibility to noise in the current supply. The current controller (blue) has a noise bump around 400 kHz. Laser frequency noise (green) is converted to voltage fluctuations using an atomic absorption feature as in Fig. 3.5(b), and exhibits a rise in its power spectral density matching that of the current controller.

but temperature control of the entire assembly stabilizes the path length of the cavity (for 6061-T6, the coefficient of expansion is 23.6 μm/m/°C, so a temperature change of less than half a degree would result in a mode hop in a 2-cm-long, 780-nm laser, even if the diode's temperature was constant).

A hermetically sealed cavity limits effects of slow changes in the lab's pressure or humidity. We seal all joints and points of mechanical access, electrical inputs, and optical outputs using Viton O-rings or a high-temperature vacuum epoxy (Epotek 353ND). A vacuum seal-off valve is machined into the front of the main body, where a pump can be attached to evacuate the cavity or backfill it with an inert gas to remove moisture, also enabling operation below the dew point. (We had initially hoped that evacuating the cavity might improve acoustic stability, but the methods used in Sec. 3.2 seem to indicate that this is not an important effect.)

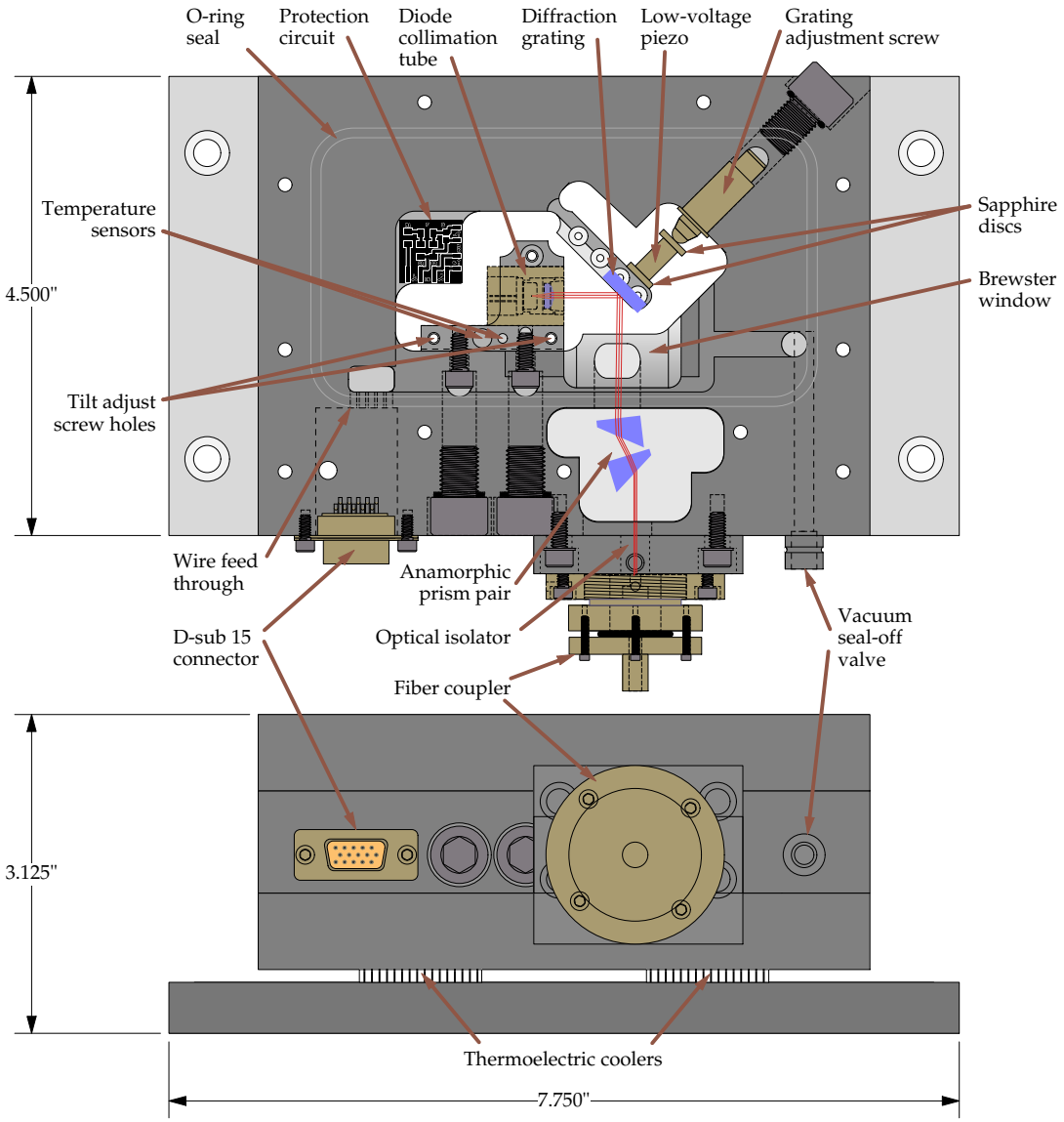

FIGURE 3.4. Assembly drawing of the novel ECDL, featuring labels of all peripherals. Complete discussion is available in [116]. The cavity body is hermetically sealed using O-rings and epoxy, and the beam exits through a microscope slide at Brewster's angle before beam-shaping, optical isolation, and fiber-coupling.

Vibration isolation is provided from below by viscoelastic (E-A-R Specialty Composites, Isodamp C-1002-06)[3] and aggregate (custom part from Castinite) materials, and a molded, floppy silicon cover. The silicon cover, built in house [127], additionally damps effects of fluctuations in lab temperature. Beam-shaping optics, Faraday isolation, and fiber coupling are all integrated, and extreme isolation from local environmental effects could be achieved by moving the ECDL to a sandbox in an atmospherically controlled chamber, for example. The point of the novel design, however, is to make such extreme measures unnecessary; while we have not carefully characterized the long-time frequency stability of our laser, we have noticed that the passive measures are quite effective: day-to-day drifts of a free-running laser are typically less than a few linewidths of the 30-MHz-wide $5s^2\,{}^1S_0 \longrightarrow 5s\,5p\,{}^1P_1$ cycling transition in ^{88}Sr.

3.2. Sensitivity to Perturbations

To measure the laser's response to external perturbations, we use a couple of techniques, pictured in Fig. 3.5. First, we actively drive the ECDL's piezo—effectively shaking the grating arm—and monitor light through a Fabry-Pérot (FP) cavity. We offset the signal by half of the FP peak height, and slowly lock (100 ms integration time) to the side of the resonance. Changes in frequency at the laser are transformed into changes in amplitude of the error signal, Fig. 3.5(a). This technique is mainly to search for acoustic resonances in the laser and we name it "cavity-resonance spectroscopy." Scope traces are produced using a Stanford Research Systems DS345 function generator to drive the piezo (0.03 $V_{p\text{-}p}$ amplitude before passing through a

[3]There may be some benefit to cutting this material into smaller pieces, as implied in the discussion about Sorbothane in Sec. 5.2.1.

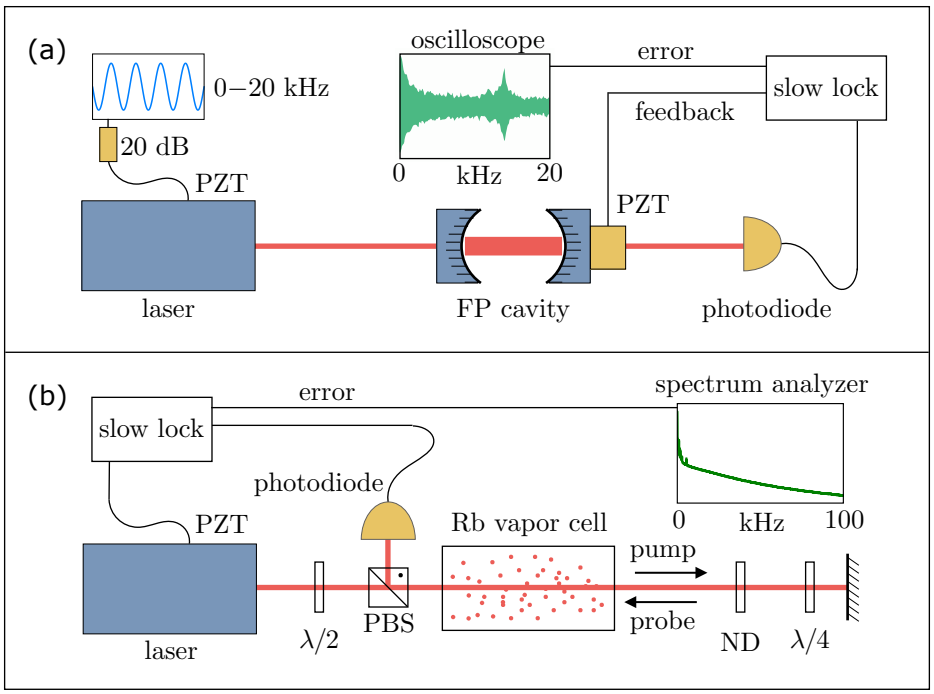

FIGURE 3.5. Schematics for methods we use to analyze the laser's susceptibility to environmental perturbations. In (a), an active perturbation excites the laser's piezo, and we measure the amplitude of the frequency response by slow-locking a Fabry-Pérot (FP) cavity to the laser and monitoring the error signal. In (b), the laser's passive frequency power spectral density is measured in a similar manner by locking the laser's frequency to an atomic resonance in ^{85}Rb.

20.2 dB attenuator) from 0–20 kHz. Two hundred traces are squared and averaged to produce the frequency-deviation data in Figs. 3.6 and 3.7.

In Fig. 3.6, we compare the novel ECDL with an existing "bronze" laser in our laboratory (named for its 954 aluminum-bronze alloy [95, 114, 115]), which is designed with a longer grating arm to optimize the pivot point and mechanical feed-forward [98]. This makes the bronze laser much more susceptible to vibrational perturbations than the new ECDL, especially at lower acoustic frequencies. Indeed, a rough estimate of the fundamental frequency (as in Sec. 3.1.1) yields 360 Hz. To compare the two lasers, the data are scaled to overlap the high-frequency tails, where the response of the lasers should be the same. At low driving frequencies, the

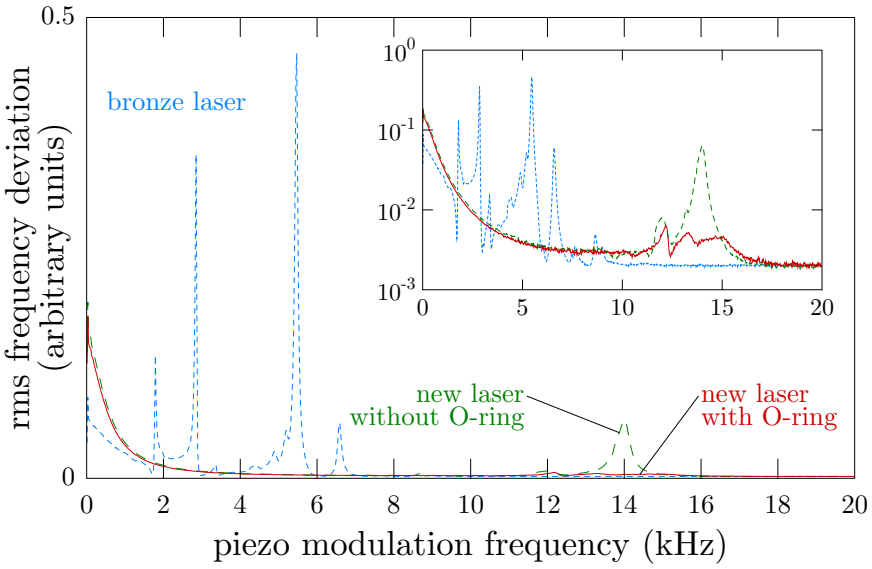

FIGURE 3.6. Laser response while driving the piezo at acoustic frequencies in the cavity resonance spectroscopy setup, Fig. 3.5(a). For comparison, an existing laser made from 954 aluminum-bronze alloy is also analyzed. The inset shows the same data on a logarithmic scale.

measured response is a result of the grating arm being tuned by the piezo rather than being an actual mechanical resonance. So while both lasers operate at 780 nm, the bronze laser has a smaller frequency deviation because the diffraction angles are different (the bronze and new lasers use 1200 and 1800 lines/mm, respectively).

The difference in resonances is significant between the two lasers, and the log-scale inset shows that lowest-frequency resonance in the new laser occurs around 12 kHz. The somewhat larger resonance at 14 kHz (which is the fundamental torsional resonance, shifted from 2.05 kHz by the piezo supporting the end of the arm) is dramatically damped by introducing a Viton O-ring underneath the grating arm. The shear damping does not affect the 12 kHz feature, and it is likely that this resonance is related to the lids. (The original prototype had 0.5″-thick lids instead of 0.75″, and we noticed that a similar resonance would shrink if the top lid was removed

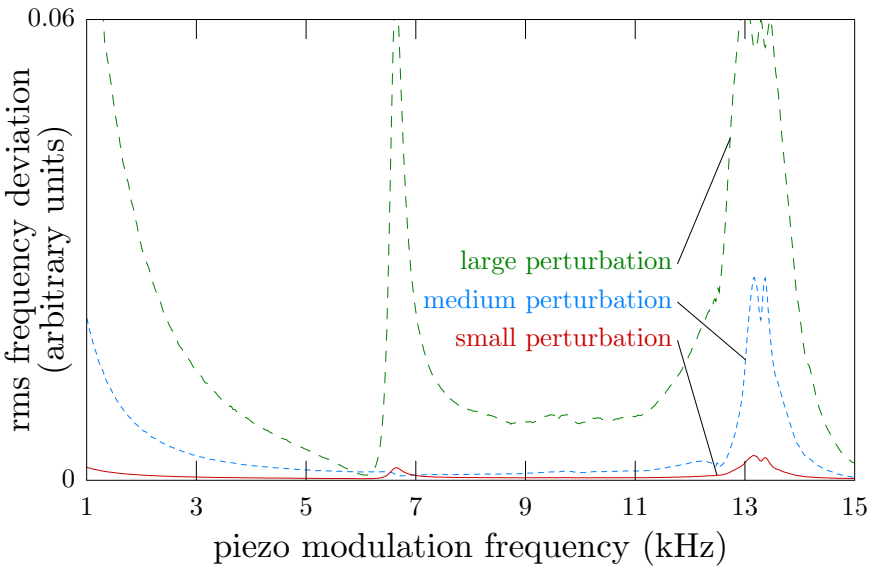

FIGURE 3.7. Response of a prototype laser under various driving amplitudes in cavity resonance spectroscopy. These data were useful in diagnosing a loosely glued diffraction grating (resonance just below 7 kHz), and were recorded in the following order: medium, large, small.

or thickened.) We did not try other materials to dampen the arm motion, but it is likely that Sorbothane would work well [128].

As implied in the preceding paragraph, cavity-resonance spectroscopy can be useful in understanding and assuaging sensitivity to perturbations. As a concrete illustration of this, in our prototype lasers we had occasionally seen small peaks in the 3–7 kHz region which did not seem to have consistent location or height and were unaffected by altering the lid or gluing masses onto the grating arm. The sequence of data presented in Fig. 3.7 helped us to confirm these resonances were caused by diffraction gratings not being glued in place firmly enough. We had originally tried to use little epoxy to reduce the mass as much as possible, but when an undergrad used larger quantities in a final production run, these resonances did not appear (to see how much was used in this run, see the pictorial guide [117]). The hypothesis was that the resonance of a shaking grating would behave in a nonlinear manner, and

driving the piezo with larger amplitudes would cause the grating resonance to grow differently than the fundamental arm resonance. We tested this on a laser with no O-ring damping, using drive amplitudes of first 0.6 $V_{p\text{-}p}$ ("medium perturbation"), then 3.0 $V_{p\text{-}p}$ ("large perturbation"), and finally 0.03 $V_{p\text{-}p}$ ("small perturbation"). The change in the grating resonance (just below 7 kHz) is clear: the response for the large perturbation is much more extreme than the medium, where the latter is barely visible. Furthermore, after the violent shaking, the resonance is still larger for small drive than it was for medium, implying that the grating has been shaken loose. After applying more epoxy, we retested the small and medium amplitudes and confirmed that the sensitivity near 7 kHz had vanished (we avoided the large perturbation condition, afraid that we might once again loosen the grating).

A second method we used to characterize the laser's response to perturbations is a measurement of its frequency-noise spectral density (fSD). Here we converted frequency fluctuations using an atomic resonance, which provides a narrower feature than the FP cavity (and also eliminates coupling from vibration of FP mirrors to the measured fSD). In this case, the laser itself was slowly locked (3 s integration time) to the $F = 3 \longrightarrow F' = 3, 4$ hyperfine crossover of ^{85}Rb using simple variant of saturated absorption spectroscopy (SAS) [129], and the fluctuations of the error signal were monitored on a digital spectrum analyzer (Tektronix RSA3408A). We did not worry about subtracting off the Doppler-broadened background because absolute frequency accuracy is not important in this measurement. The hyperfine splittings help convert the error signal voltage to a frequency via a factor η, and we used this to transform the power spectrum $P(f)$ measured by the analyzer into an fSD $S_\nu(f)$ for the laser via $S_\nu(f) = \eta^2 R P(f)$, where R is the 50-Ω impedance of the spectrum analyzer.

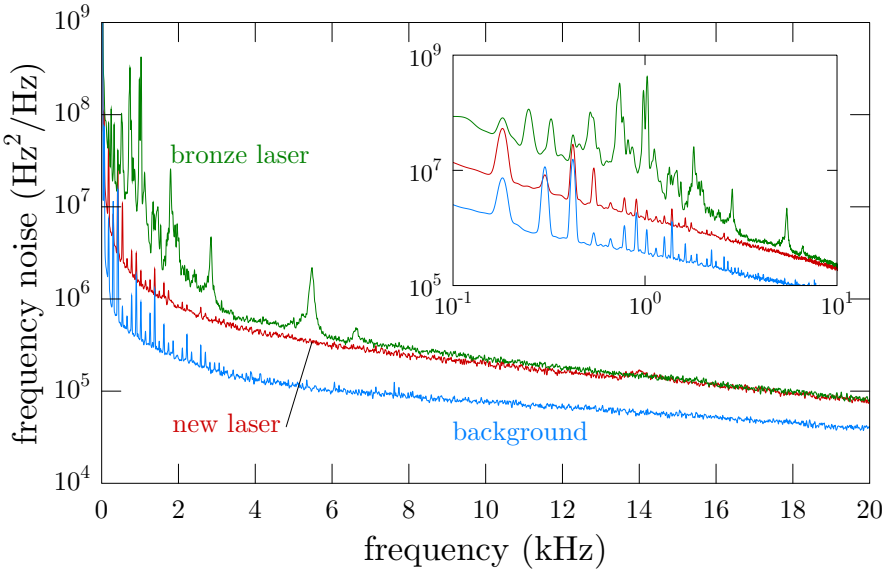

FIGURE 3.8. Frequency-noise power spectral density (fSD) as a function of frequency, measured with the setup in Fig. 3.5(b) from 0–20 kHz. Inset is on a log-log scale up to 10 kHz to highlight that many of the low-frequency noise peaks are associated with pickup during acquisition since they are also in the background data.

Data for the frequency-noise power spectral densities are presented in Fig. 3.8, including a trace taken with the light to the photodetector blocked to serve as a baseline. Each trace represents several minutes of averaging performed by the spectrum analyzer. The lasers were powered by a Libbrecht–Hall-style current source from Vescent Photonics (D2-105) to minimize the supply's contribution to the frequency noise. The measurement was performed in a quiet environment: no one spoke, the optical table was "floated," and we turned off unnecessary equipment such as a high-efficiency particulate arrestance (HEPA) filter fan. Even under such quiet laboratory conditions, the difference between the new laser design and the older bronze laser is stark. The resonances in the bronze laser appearing in Fig. 3.6 are all visible here, highlighting the importance of eliminating susceptibility to low-frequency perturbations in the new design. The fSD of the new laser sits below the bronze, save for the small peak at 14 kHz, above which the two lasers are indistinguishable.

We also looked at the fSD measurements while actively perturbing the lasers (clapping, tapping on the optical table, etc.) and observed that the new laser was much less sensitive. In fact, after increasing the robustness of the feedback servo (by adding a proportional stage and decreasing the integrating time constant), the new laser was difficult to unlock, even via direct physical contact. This led us to make similar fSD measurements under extreme, "calibrated" perturbation by an airhorn (roughly 105 dBA in the vicinity of the lasers). The frequency excursions of the bronze laser were larger than the crossover feature, so we instead had to lock onto the side of the Doppler-broadened D_2 line. The fSD in this case could not be averaged, and a single trace from each laser are presented in [116].

3.3. Linewidth Measurements

The mean-frequency excursion $\Delta\nu_{\mathrm{rms}}$, akin to the laser linewidth due to noise in a particular frequency band, is found by integrating the fSD between f_1 and f_2 [130],

$$\begin{aligned}\Delta\nu_{\mathrm{rms}} &= \sqrt{\int_{f_1}^{f_2} \bar{S}_\nu(f)df} \\ &= \eta\sqrt{R\int_{f_1}^{f_2} \bar{P}(f)df}.\end{aligned} \tag{3.5}$$

Here, $\bar{S}_\nu(f)$ and $\bar{P}(f)$ are the the adjusted fSD and power spectral density, found by subtracting the background signal. The lower frequency can be interpreted to be related to the observation time $f_1 = 1/T_{\mathrm{obs}}$, which should be specified when discussing a laser's linewidth (see Sec. C.3.3). Integrating the data in Fig. 3.8 from 20 Hz to 100 kHz gives $\Delta\nu_{\mathrm{rms}} = 296(26)$ kHz for the bronze laser and 146(8) kHz for the new laser over a 50 ms observation time. The difference in these measured linewidths is entirely in the band below 10 kHz, and by more carefully controlling the

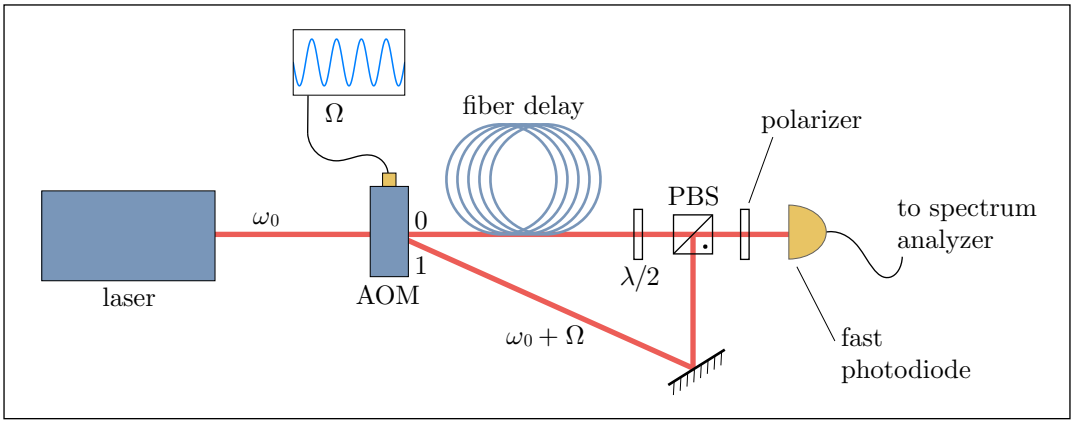

FIGURE 3.9. Schematic depicting the delayed self-heterodyne measurement. An AOM operating at frequency Ω splits a laser into two paths of an interferometer. One of the arms has a long fiber delay before the two beams are combined on a fast photodiode (New Focus 1801-FS). The resultant spectrum, centered at Ω, contains information about the laser's linewidth (see Appendix C).

mechanical behavior of the laser at these frequencies, we have cut the linewidth in half. Moreover, in the case of the airhorn, the integrated rms noises are $\Delta\nu_{\text{rms}} = 40$ MHz and $\Delta\nu_{\text{rms}} = 1$ MHz for the bronze and new laser, respectively, demonstrating the superior performance of the new laser under active perturbation.

Another method used to measure laser linewidth is the delayed self-heterodyne technique [131, 132], discussed in more detail in Appendix C. In this process, depicted in Fig. 3.9, a laser is interfered with itself, producing a beatnote on a photodiode (from which linewidth information can be ascertained). An acousto-optic modulator (AOM) shifts the beatnote spectrum away from dc for easy measurement on a radio-frequency (RF) spectrum analyzer. One version of the laser is time-delayed by traveling through a long fiber so that two different time periods can be compared. If the delay is long compared to the coherence time of the laser, the two beams have uncorrelated frequency noise and can be regarded as separate sources. In this case, extraction of the laser's full width at half maximum (FWHM) linewidth is straightforward, but a more precise understanding is generally necessary.

Using the machinery of phase-fluctuation statistics [133], the laser's frequency is modeled to have both white- and $1/f$-noise components:

$$S_\omega(\omega) = \gamma + \frac{k}{|\omega|}. \tag{3.6}$$

The white-noise parameter γ is the modified Schawlow-Townes linewidth, Eq. (3.1), while the k parameter characterizes the strength of the $1/f$ noise expected in an electronic device. The current power spectral density measured at the photodiode in the self-heterodyne technique is

$$S_I(\omega) \propto \int_{-\infty}^{\infty} d\tau e^{-i(\omega-\Omega)\tau} \exp\big(-\gamma \min\{|\tau|, |t_d|\} - \delta_{\text{drift}}\tau/2 - (\delta_{\text{RBW}}\tau)^2/16\ln 2\big) \times \left[|\tau + t_d|^{-k(\tau+t_d)^2/2\pi} |\tau - t_d|^{-k(\tau-t_d)^2/2\pi} |\tau|^{k\tau^2/\pi} |t_d|^{kt_d^2/\pi}\right], \tag{3.7}$$

where t_d is the delay time, Ω is the AOM frequency, and δ_{RBW} is the Gaussian resolution bandwidth (RBW) of the spectrum analyzer. This equation is the same as Eq. (C.20) with the addition of the δ_{drift} term, which accounts for drift in Ω during averages on long timescales by convolving the resulting spectrum with a Lorentzian of width δ_{drift}. Information about the observation time T_{obs} is contained in δ_{RBW}, and this term explicitly cuts off the integral, which would be otherwise divergent for large t_d [39].

We have three lengths of single-mode telecommunication fiber to use as delay paths: 2.260 km, 4.415 km, and 4.457 km. These are combined to take a series of self-heterodyne spectra at various delay times, such as those pictured in Fig. 3.10. For short delays, coherent wiggles can be clearly seen in the wings of the spectrum, and these are used to fit the time delay t_d in the 2.260 km fiber. This sets the light's wavelength-dependent propagation speed in the fiber, which is used to determine t_d

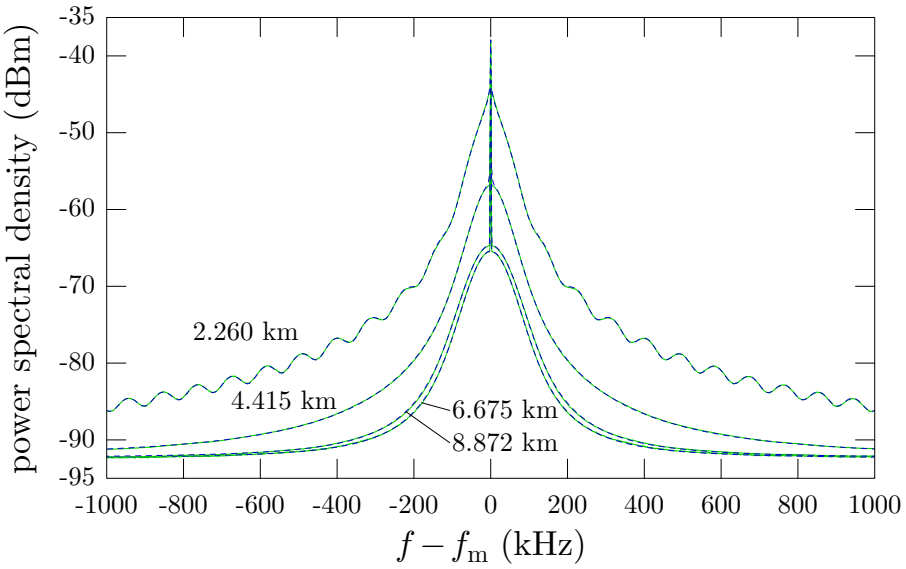

FIGURE 3.10. Delayed self-heterodyne spectra of a 922 nm laser, including both data (green line) and numerical fitting (dashed blue line) described the text. The RF frequency of the AOM is $f_{\mathrm{m}} = \Omega/2\pi = 80$ MHz. Four fiber lengths are used, and fitted spectral parameters are $\gamma = 1.86(29)$ kHz and $\sqrt{k}/2\pi = 27.0(15)$ kHz, yielding an expected 32 kHz FWHM linewidth for $T_{\mathrm{obs}} = 100$ μs.

for longer delays. The spike in the center of the spectrum is caused by remaining coherence in the laser's frequency fluctuations and by extra RF pickup of the AOM signal by the spectrum analyzer.

We numerically fit the data using Eq. (3.7), taking as fitting parameters δ_{RBW} and δ_{drift} for the spike, and γ and k for the spectral tails. Amplitudes for the spike and remaining spectrum, as well as a background baseline level, are also used to fit the height of the spectra. The results of the fit (dashed blue line) are plotted with the data (solid green line) for a 922 nm laser in Fig. 3.10, and the model is clearly sufficient to characterize both the center and the tails of the spectra. (Often, linewidth analyses only consist of fitting a Lorentzian to the spectrum and taking half of the resulting FWHM as the linewidth, but these miss the Gaussian part caused by $1/f$ noise and underestimate the actual width [116, 132].) After the γ and k parameters are known,

the overall FWHM linewidth can be computed for a specified rectangular-window observation time $T_{\rm obs}$ [39].

We used the self-heterodyne technique to characterize several lasers we made [116], but of special interest is an extra-long ECDL we constructed at 689 nm for use in narrow-band cooling on strontium's $5s^2\,{}^1S_0 \longrightarrow 5s5p\,{}^3P_1$ intercombination line (which is less than 10 kHz wide). For comparison, we also constructed an otherwise identical 689-nm laser in the standard "short" length depicted in Fig. 3.4. As discussed previously, a diode laser's linewidth is inversely related to the square of the cavity length [see Eqs. (3.1) and (3.2)], so the linewidths of two ECDLs operating at the same frequency with similar cavity length stability are related by

$$\Delta\nu_1 = \Delta\nu_2 \frac{L_2^2}{L_1^2}. \tag{3.8}$$

For an ECDL, the total cavity length is the sum of the optical path length in the diode itself and the extended cavity length: $L = nd + L_{\rm ext}$. Typically, $nd \sim 600$ μm, and the added lengths of our two cavities are 2.2 cm and 10.0 cm. We therefore expect the linewidth of the long laser to be reduced by roughly a factor of 20. Self-heterodyne spectra for the 2.260 km fiber for the short- and long-cavity lasers are shown in Fig. 3.11. Clearly the short laser has a much smaller coherence time since periodic structure is not visible in the tails of the spectrum. Averaging the fits of two fiber lengths (because Rayleigh scattering at 689 nm is significant, longer delays are not feasible), we find the noise parameters to be $\gamma/2\pi = 93(36)$ kHz and $\sqrt{k}/2\pi = 87.0(7)$ kHz for the short laser and $\gamma/2\pi = 4(1)$ kHz and $\sqrt{k}/2\pi = 22(1)$ kHz for the long. The reduction in white-noise linewidth is consistent with the increase in cavity length. Using these parameters the short- and long-laser's FWHM are 254 kHz and 11.7 kHz, respectively, for $T_{\rm obs} = 100$ μs.

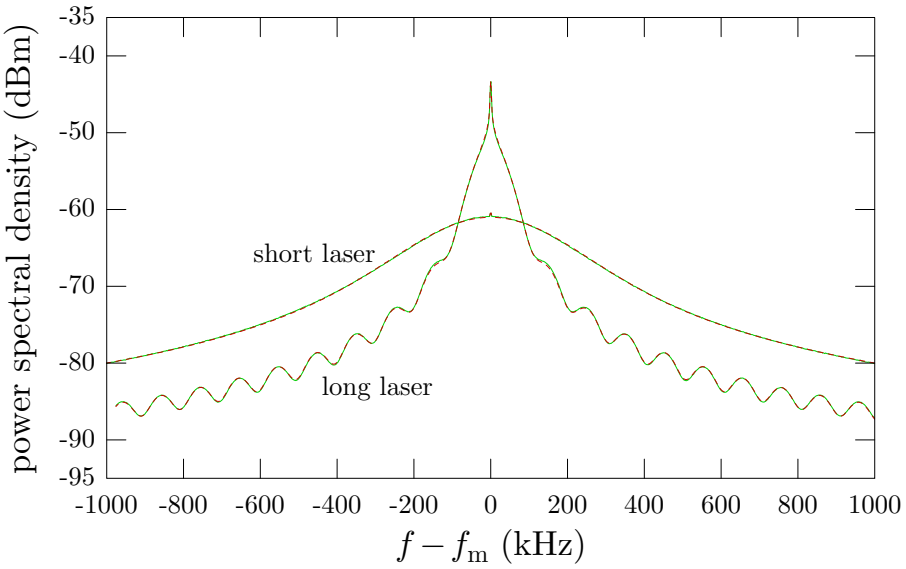

FIGURE 3.11. Measured data (green lines) and numerical fits (dashed red lines) using a 2.260-km delay fiber for two 689 nm lasers with different cavity lengths. Reduction in linewidth of the long laser matches expectations (see text).

3.4. Construction and Assembly Details

Complete details of the laser's peripherals are discussed in [116], and the pictures posted on our website [117] are useful, but inexperienced users may require a little more guidance to assemble the ECDL. This section provides some extra instruction where necessary.

3.4.1. Customizing a Particular Wavelength

A primary goal in designing the new laser was to make it cheap to construct and easily adaptable to many wavelengths. We made efforts to minimize the number of orientations and tool changes required on a computer numerical controlled (CNC) milling machine, and also used stocked commercial peripherals when possible. Interactions with the machine shop are simplified by using a standard set of machined pieces for any laser, with the operating wavelength being determined by a few key

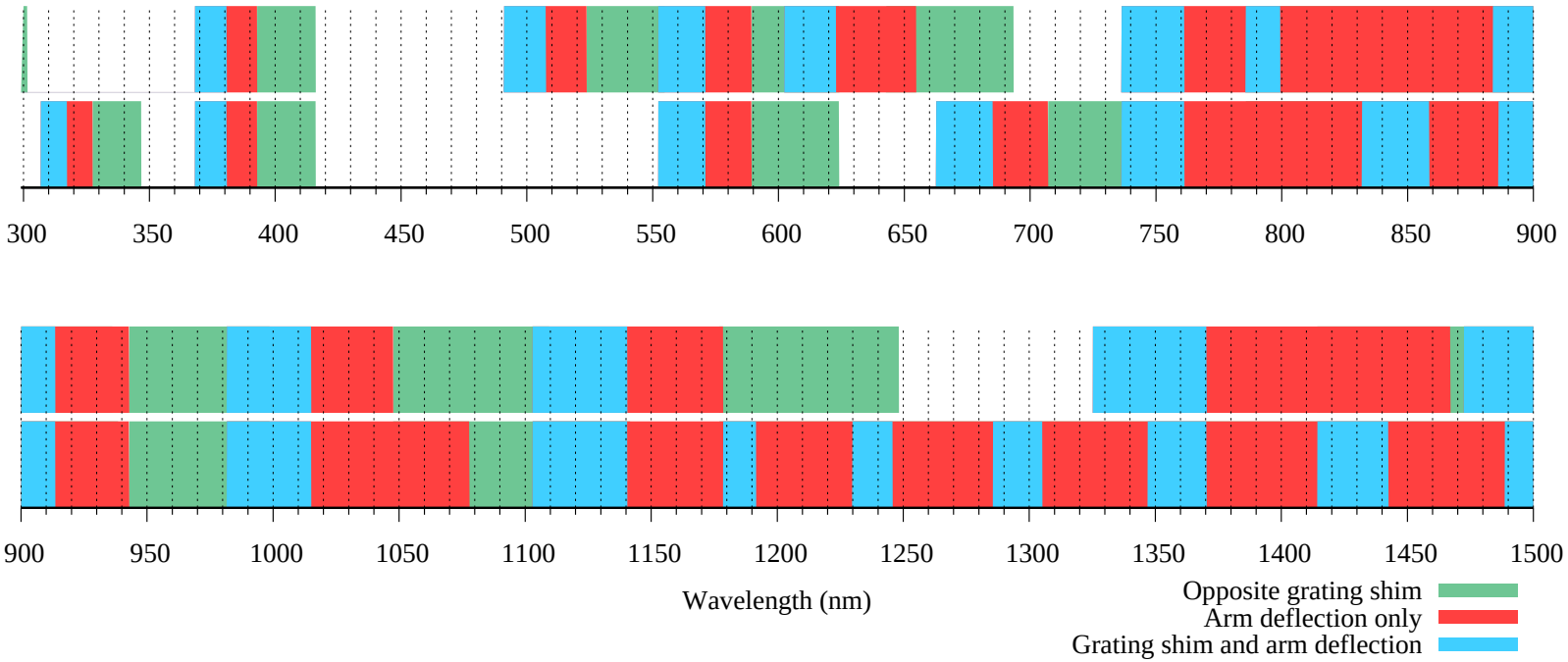

FIGURE 3.12. Wavelengths that can be realized with the novel ECDL design using stock Richardson diffraction gratings between 300 nm and 1500 nm. Available wavelengths for ruled gratings are presented above those for holographic ones. Red regions do not require any shimming of the grating, but blue and green require normal and reverse shimming, respectively (where "normal" shimming is performed at the end of the grating arm). Details of choosing the correct number of lines/mm for a particular wavelength are given in the text.

optical components—the laser diode, diffraction grating, anamorphic prism pair, optical isolator, and fiber coupler. This also adds flexibility and utility to spare or retired lasers without need of additional machine work.

Referring again to Fig. 3.4, the basic cavity geometry has light from the diode incident on the diffraction grating at $\sim \pi/4$ radians. The exact angle is determined by the diffraction equation in the Littrow configuration, where $\alpha_{\text{in}} = \alpha_{\text{out}} =: \alpha_{\text{g}}$ and the diffraction order is $m = 1$:

$$\begin{aligned} \lambda &= \frac{d}{m}(\sin\alpha_{\text{in}} + \sin\alpha_{\text{out}}) \\ &= 2d\sin\alpha_{\text{g}}. \end{aligned} \tag{3.9}$$

Here d is the separation between grooves in the grating, but values are typically given in the number of lines/mm. Recall that the diffraction grating arm (Sec. 3.1.1) is designed to be "loaded" into place by the piezo and fine adjust screw, but since we want to avoid fatiguing the aluminum, large changes to this location should be avoided. This means angles that $\pi/4 - \alpha_{\text{g}}$ should be positive (to retain tension in the flexure pivot and avoid "unloading" the arm) and relatively small. We have successfully deflected the arm by $\pi/4 - \alpha_{\text{g}} \approx 2^\circ$, but any angle larger than this requires a shim behind the outer edge of the grating. Our custom-sized gratings have a width of 12 mm, so this angle is converted to shim thickness (in thousandths of an inch) via $t = 1000(12/25.4)\sin(\pi/4 - \alpha_{\text{g}})$. We usually undersize the shim by about $0.005''$ to allow leniency for burrs or layers of epoxy adding extra thickness. Fig. 3.12 shows a range of wavelengths that can be achieved using our laser's geometry and a list of available ruled and holographic diffraction gratings from Newport's Richardson Gratings (these are gratings for which they have a "master" grating, which cost about

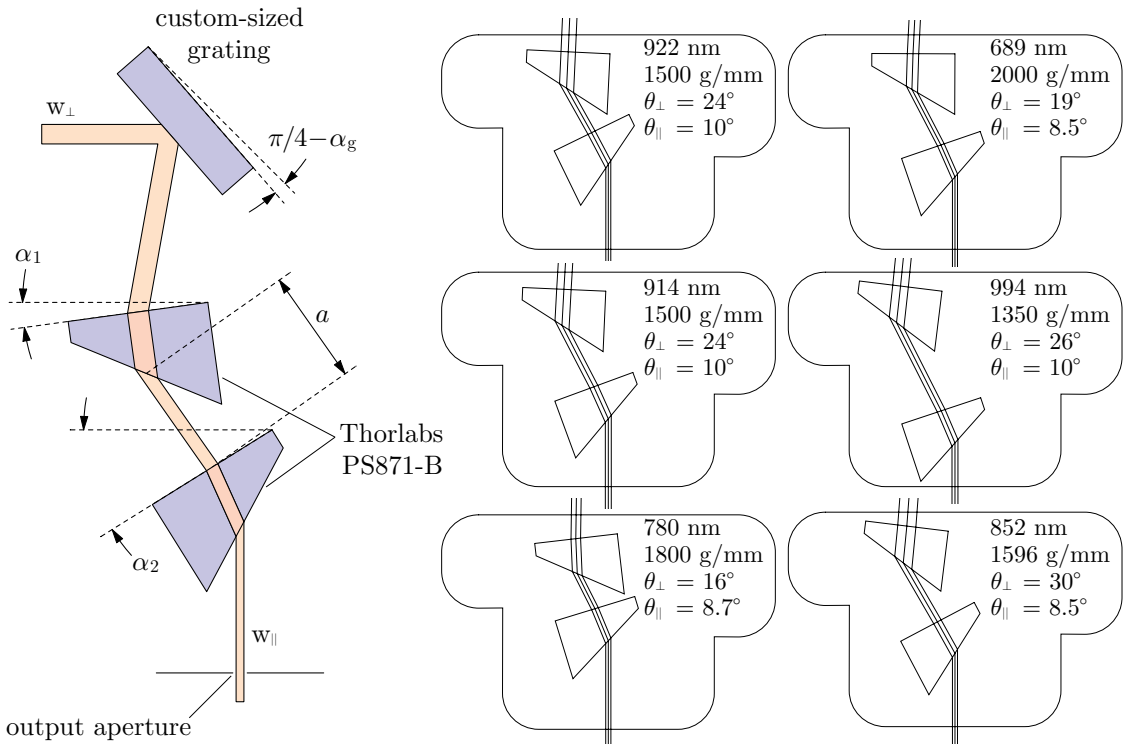

FIGURE 3.13. Numerically determining the location of anamorphic prisms. The grating angle α_g is set by the Littrow condition for λ by Eq. (3.9), and α_1, α_2, and a are calculated to enable fiber coupling at the output aperture. Footprints for prism locations (which are to scale and can be directly printed from this document) are shown for strontium-wavelength lasers as well as common rubidium and cesium wavelengths. Diverging angles $\theta_\perp$ and $\theta_\parallel$ are taken from laser diode data sheets.

$10k to produce). Note that "normal" shimming is preferred over "reverse" based on the location of the beam output from the laser body. (The idea of a reverse shim to expand wavelength coverage came after we finalized and published the design, and we anticipate that much of the green areas in the figure cannot be nicely circularized or fiber-coupled without some extra machining or creativity.) Note also that the figure is *not* representative of wavelengths covered by existing laser diodes, and that a suitable source still needs to be attained.

The magnification of the prism pair, meanwhile, is determined by the desired operational wavelength and the divergence angles of the laser diode, typically given

as FWHM angles $\theta_\perp$ and $\theta_\parallel$, where the orientation is relative to the diode junction (for a TE diode, light is polarized parallel to the junction, along the minor axis of the elliptical output). Fig. 3.13 shows a (not-to-scale) cartoon of the grating and prisms, where the beam is circularized by transforming $w_\perp$ into $w_\parallel$ (while not affecting $w_\parallel$ in the orthogonal direction). We start with the position and orientation of the diffraction grating for the given λ, assuming the grating has been pivoted and shimmed at the standard location of the supporting arm. Next, three parameters—the angle of the first prism α_1, the angle of the second prism α_2, and the distance between them a—are adjusted numerically until the beam is circularized and passes normal to the laser body through a fixed output point (for fiber coupling). A computer script generates an outline footprint of the resultant prism locations which can be printed and glued into the prism pocket for aid in alignment (we etch the outline on a thin piece of acrylic using a laser cutter, which works nicely). The outlines in Fig. 3.13 for strontium, rubidium, and cesium wavelengths are presented to scale and can be printed directly for use in building lasers at these wavelengths. Additional wavelengths require the use of the Octave script posted on our web site [117]. By default the beam is constrained to pass through the center of the prisms, but they might need to be nudged to avoid touching each other or the pocket boundary.

3.4.2. Final Assembly and Alignment

After a suitable geometry is chosen, the grating is epoxied in place using a Torr-Seal equivalent (Duniway "Epoxi-Patch" EP-8034) as one of the final steps in assembly. A machined spacer positions the grating against the top outer edge of the arm, and a laser-cut jig holds the laser so the grating lays flat (we made a couple of attempts to clamp the grating in place, but nothing worked as well as using gravity

to hold it in place, especially with the complication of sandwiching a small shim in place). We use three dots of epoxy on the exterior of accessible corners of the grating-arm interface and carefully slide the spacer out after the epoxy sets overnight. It's a good idea to refrain from putting epoxy underneath the grating: the grating should be secure enough that it does not vibrate as in Fig. 3.7, but should also be easy to break free if necessary.

To more easily align the laser diode, it is helpful to be able to lift the entire diode can mount out of the laser body and move it to an external platform. This means that wires connecting the protection circuit, diode, and temperature sensors should be as long as possible while being short enough to fold nicely into the main cavity pocket. First, the laser's output is pointed at a far wall and the aspherical optic in the collimation package is adjusted to minimize the spot size (ensuring the beam does not go through a focus). Next, a polarization beamsplitting cube (PBS) is used to orient the polarization. Since for our diodes we wanted our light to be vertically polarized, we minimized transmission through the PBS by rotating the collimating tube inside the mounting block. A 4-40 screw secures the tube in place, and it is helpful to pre-tighten this somewhat with the tube sticking about $0.25''$ out of the front of the block. The tube can then be rotated with fingers to controllably find the minimum, at which point the screw is tightened a bit more. The tube is then pushed into the mount until the front faces are flush—while making sure the minimum transmission does not change—and the screw is fully tightened. We recommend this procedure because using the wires at the rear to rotate the can be frustrating, not to mention dangerous for the diode.

The aligned diode can mount is placed inside the main cavity body, loosely attached using two $1/4''$ 8-32 screws, and the wires are carefully packed into the

available space behind the diode (the protection circuit should not be epoxied in place, since removal of the diode may be necessary in the future). Standard procedures are followed to align the cavity [110], with horizontal alignment performed via the screw behind the grating and vertical alignment with two rounded 4-40 screws threaded through the diode can block, pushing off the bottom lid. It is helpful to set the current just above threshold and iterate horizontal and vertical degrees of freedom while monitoring the wavelength on a wavemeter (such a step was crucial in prototype versions of our laser, where the grating adjustment screw did not push in the center of the arm and the horizontal and vertical degrees of freedom were coupled). When the desired wavelength is reached, the grating is in the correct position, and threshold should be minimized using the vertical tilt screws. Raising the diode (clockwise screw motion) is easier than lowering, which requires force on the adjusting ball driver to push the can downward. To rigidly secure the diode can mount to the main cavity block, the 8-32 mounting screws are tightened while the tilt screws are removed (the diode's position is thus not over-constrained and is less susceptible to future creep). This process is somewhat difficult, and iterative tightening and loosening by small amounts is required. Even then, a discontinuous shift in alignment can happen as tension in the tilt screws is released, and tightening often needs to be repeated numerously in a somewhat stochastic process.

Finally, anamorphic prisms are installed using the printed outline as a guide. The laser's output is monitored about a meter away, and small changes are made to prism locations and angles so that the beam is roughly round and—more importantly—perpendicular to the laser body. An optical isolator is attached to the main cavity body, and the laser is then ready to be coupled into fiber. We have had some difficulty with the fiber couplers we use from Oz Optics (HPUC series). The locking screws are

not rounded and will cut slight grooves into the anodized laser-head adapter; upon subsequent coupling and locking, these produce uncontrollable shifts in the position of the coupling lens. We rounded our own screws (McMaster 92196A048) and inserted small sapphire disks (Swiss Jewel W4.07) to circumvent this issue.

CHAPTER IV

EXPERIMENTAL APPARATUS

4.1. Vacuum System

Maintaining atoms in a MOT for an appreciable amount of time requires the trap to be sufficiently isolated from collisions with background gas. Trap lifetime is inversely related to the pressure [134], and one can actually use this to infer the pressure through lifetime measurements [135, 136]. Because of this sensitivity to background-gas collisions, an indispensable part of an atom-trapping apparatus is an ultra-high vacuum (UHV) system. This section discusses the design and construction of our UHV chamber, pictured in Fig. 4.1, and its associated peripherals. Vacuum technology is a mature field of physics, and there are many sources which cover in much greater detail the methods and components described here [137–139].

The chamber for our setup has two distinct regions: a high-pressure side (left) featuring a hot-oven atomic-beam source, and a low-pressure side (right) where cooling and trapping occurs. The pipe transitioning between the two regions acts as a differential pumping tube and is where preliminary cooling of the atomic beam takes place in a "Zeeman slower." In the low-pressure region, atoms are trapped in a "top MOT" at the center of a spherical octagon and can be delivered to a "bottom MOT" inside a pyrex cell (ColdQuanta CQMC0006), which provides increased optical access and isolation from the stream of hot strontium atoms coming from the oven.

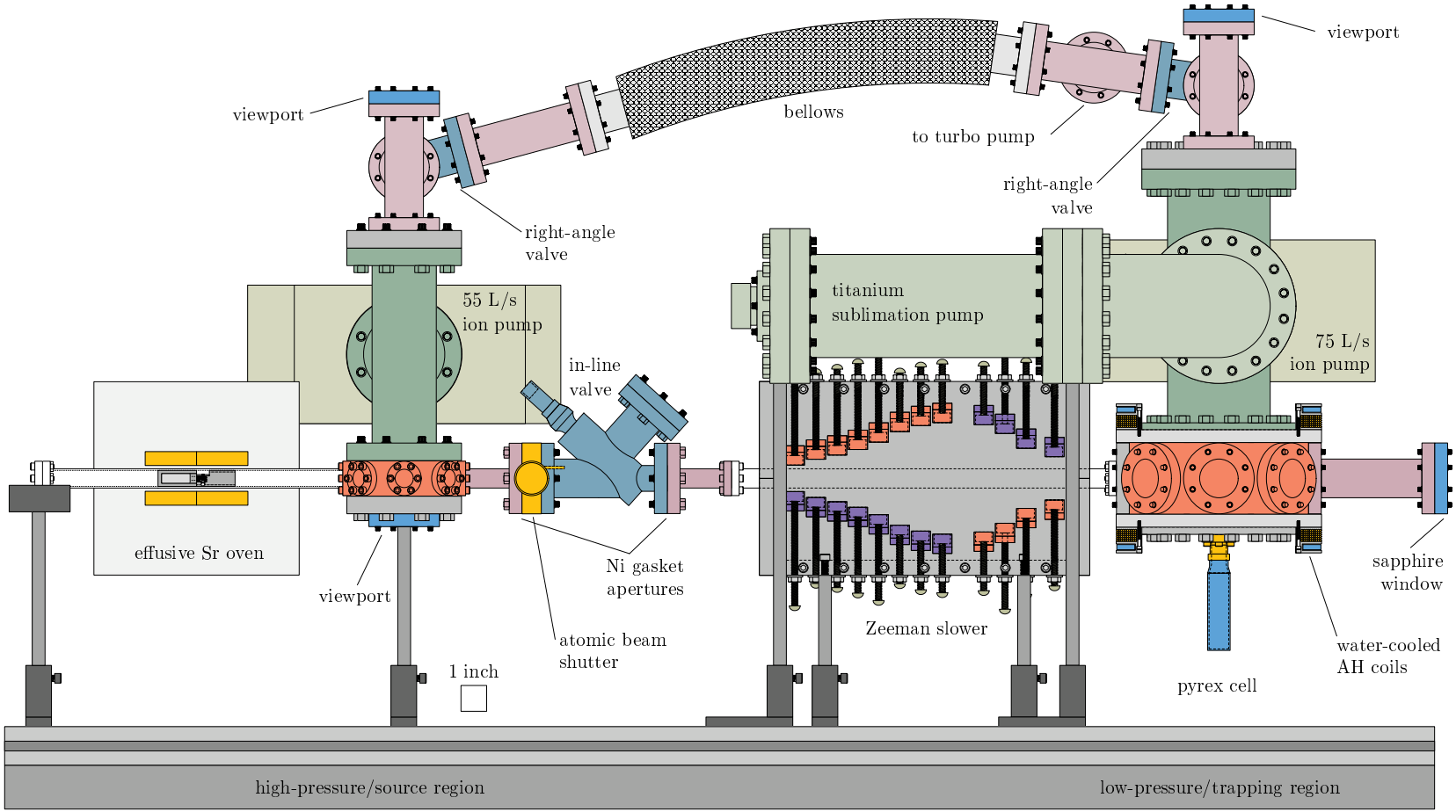

FIGURE 4.1. Schematic of the UHV chamber used for trapping and cooling strontium atoms. Atoms originate from the effusive oven (high pressure, far left), pass through a permanent-magnet Zeeman slower (center), and are trapped in a spherical octagon and a vertically oriented pyrex cell (low pressure, right). A pair of right-angle valves allow a turbomolecular pump to be connected to both sides of the chamber via temporary bellows.

4.1.1. Hot Strontium Source

4.1.1.1. Oven Design

A schematic drawing of our strontium oven is shown in Fig. 4.2. All internal parts are machined from 316L stainless steel, as this is inert with Sr vapor [140]. Solid strontium is placed in a crucible with a circular output aperture of 0.25″ diameter. Adjacent to the crucible, a collimating nozzle is made of a bundle of capillary tubes, which are 1-cm long with nominal 203 μm inner diameter (ID) and 414 μm outer diameter (OD). Capillaries are cut from long hypodermic tubing (Small Parts B000FN0TL2) using a narrow grinding wheel, and are then cleared of burrs with a wire brush and individually inspected for a clear aperture. The nozzle and crucible are sized to fit snugly in the center of a custom-length 12″ nipple, which has a smooth-bore, 0.620″ ID interior. (We first ordered the custom-length nipple from Kurt J. Lesker Company, but this tube was rolled and welded and had a 0.020″ ridge on the inside. The UO machine shop had some pipe with higher quality interior surface finish we used instead.) Four loose-fitting tubes (0.615″ OD) slide into the nipple and act as spacers to accurately position the location of the effusive oven.

Fortunately, we can achieve temperatures to create sufficient Sr vapor without using electrical feedthroughs and heaters inside the vacuum chamber. The yellow rectangles in Fig. 4.2 represent semi-cylindrical clamshell radiative heaters, which heat the crucible and nozzle from the exterior. Two custom-length pairs of heaters (Thermcraft RL106-S-L, 110 W) are imbedded in semi-cylindrical insulation housing (Thermcraft VIP-2.5-10-0.75-2) and secured around the 0.75″ OD oven pipe. Wired in series, the two heaters around the nozzle are heated to be 50°C warmer than those around the crucible to counteract clogging from condensing Sr. The heaters are

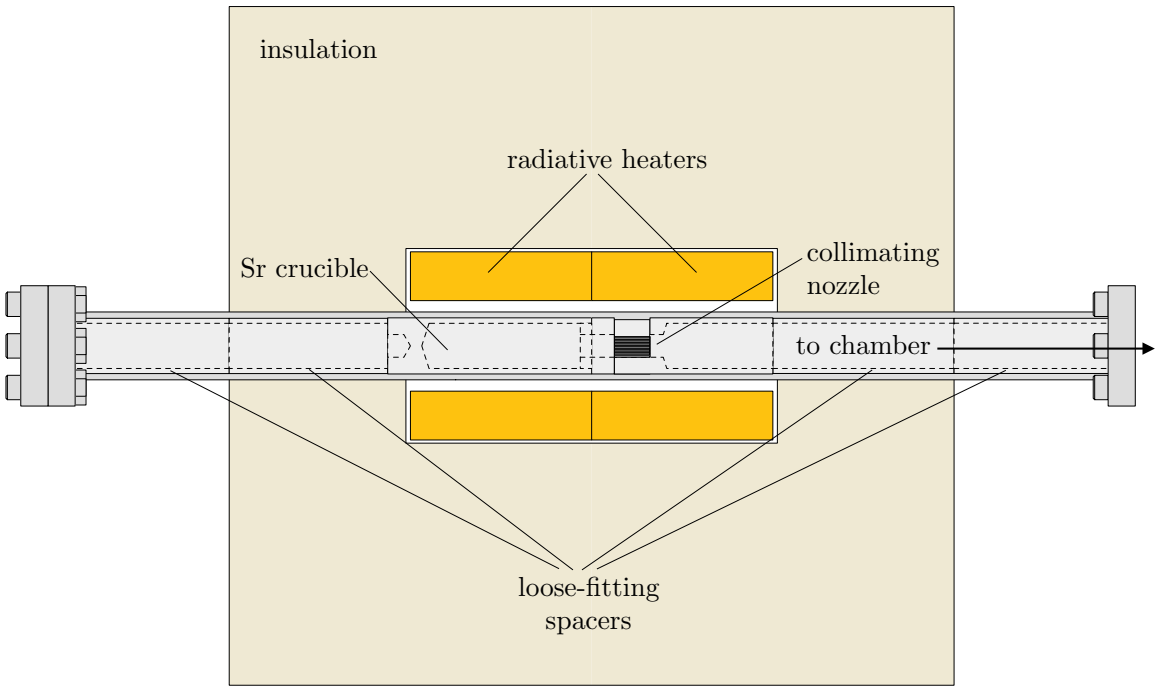

FIGURE 4.2. Schematic of the strontium source. A crucible and collimation nozzle are centered in a custom-length nipple and heated externally. The nozzle's temperature is maintained to be 50°C warmer than the crucible to prevent clogging.

connected to a Variac set to 38 V rms source, switched by solid-state relays (Omron G3NA-220B) that are driven by temperature controllers (Love Controls TCS-4011) which monitor the temperature using type-J thermocouples. We originally attempted to switch heaters with the Love controller directly, but its internal relay failed (in the closed position, effectively removing the ability to switch off the heater) after several weeks.

Inspecting a photo of the completed nozzle reveals $N = 184$ capillaries in our bundle, with an additional capillary that appears to be blocked at the input aperture. We loaded a total mass of 3.21 g of $\geq 99\%$ pure Sr (Sigma Aldrich 474746-25G) into the crucible and assembled the oven inside a glove bag filled with argon. The crucible is tapped on the rear end (left side in Fig. 4.2) for extraction when recharging the oven, although we anticipate that the crucible will fuse to the nipple and be irremovable.

In this case, before reproducing a new set of the aforementioned custom components, there are additional Sr oven solutions which are worth considering [141, 142].

4.1.1.2. Molecular Flow Conductance

Dynamics of molecular flow depends on the density of gas and geometry of its container. Typically, the Knudsen parameter $K_n = l/a$ defines two distinct regimes (here, l is the mean-free path of the gas and a is the characteristic length of the container, often the radius of a cylindrical pipe [137]). At high densities, $K_n < 0.01$, the dominant interactions are inter-particle collisions of gas molecules, and flow dynamics are that of a compressible, viscous fluid. Low densities, meanwhile, are governed by particle-wall collisions, and for $K_n > 1$ flow can be more simply determined from a statistical ensemble of non-interacting thermal particles. In the geometry of our oven, strontium atoms entering a 203 μm ID capillary will be in the latter regime (referred to as the molecular or effusive regime) for temperatures below 700°C.

Velocities in the oven are given by the Maxwell-Boltzmannn distribution $f(\mathbf{v})$, and we can find the distribution of atoms moving in the z-direction by integrating over the transverse components,

$$\begin{aligned} f(v_z) &= \int f(\mathbf{v}) dv_x dv_y \\ &= n \left(\frac{m}{2\pi k_\mathrm{B} T} \right)^{1/2} \exp\left(-\frac{m v_z^2}{2 k_\mathrm{B} T} \right). \end{aligned} \tag{4.1}$$

This is normalized to the number density n, so the flux of atoms with a particular velocity passing through an aperture of area A is then $b(v_z) := A v_z f(v_z)$, where $b(v_z)$ is the velocity distribution for a molecular beam with $v_z > 0$. Integrating $b(v_z)$ over

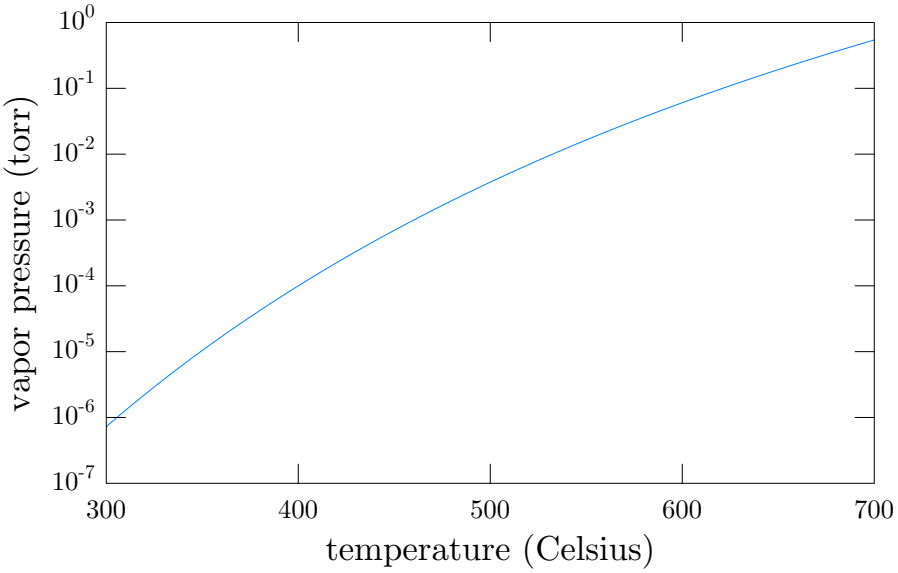

FIGURE 4.3. Vapor pressure of strontium. A larger version is given in Appendix B.

all positive velocities gives the total atomic flux through the aperture. The result is

$$\Phi_A = \frac{A p_{\mathrm{v}}}{\sqrt{2\pi m k_{\mathrm{B}} T}}, \tag{4.2}$$

where the number density n has been rewritten in terms of the vapor pressure p_{v}, assuming an ideal gas. The vapor pressure is determined using empirical data tabulated by C.B. Alcock [143],

$$\log_{10} p_{\mathrm{v}} = 5.006 + 9.226 - \frac{8572}{T} - 1.1926 \log_{10} T, \tag{4.3}$$

and is plotted in Fig. 4.3.

4.1.1.3. Operating Lifetime and Beam Flux

Conductance through a pipe or duct is the product of the aperture flux of Eq. (4.2) with a geometric transmission probability α. If we assume the nozzle has a

hexagonal close-packed arrangement of capillaries, then the gaps between capillaries are approximately triangular and we can estimate the transmission probability through these orifices [144]:

$$\Phi_{\text{total}} = \frac{p_{\text{v}}}{\sqrt{2\pi m k_{\text{B}} T}} \left(N\alpha_{\circledcirc} A_{\circledcirc} + N\alpha_{\Delta} A_{\Delta} \right), \tag{4.4}$$

where the symbols $\circledcirc$ and Δ refer to capillaries and gaps, respectively. This is an overestimate of the flux because the triangular gaps have an area which is nearly a factor of three larger than the area in a close-packed arrangement. (Furthermore, from the machine drawing of the nozzle, the full area of the aperture is measured to be 27.5 mm^2, while the combination of $N = 184$ capillaries and triangles covers 28.3 mm^2.) However, it could also be an underestimate if there are large gaps between capillaries (that is, the close-packed assumption is bad) or around the outside of the bundle. Given that we loaded 3.21 g of strontium in our oven, we find the temperature-dependent operating time plotted in Fig. 4.4. This assumes round-the-clock operation, but we typically only run the oven while we are in the lab tending the experiment.

The flux of atoms which is delivered to the top MOT trapping region is influenced by the geometry of the gaskets in our differential pumping tube, schematically shown in Fig. 4.5. Atoms which pass uninhibited through a capillary spread at a full-angle of about 2.3°. We further collimate this beam by using two nickel gaskets placed on either side of the all-metal angle valve which separates the high- and low-pressure chambers. Atoms entering the trapping region thus have limited transverse velocities: $v_{\perp} < a v_z / d$, where d is the distance between the beginning of the capillary and the final aperture of radius a [145].

With these new boundary conditions, we integrate out the transverse velocities of the Maxwell-Boltzmann distribution to find the velocity distribution for a collimated

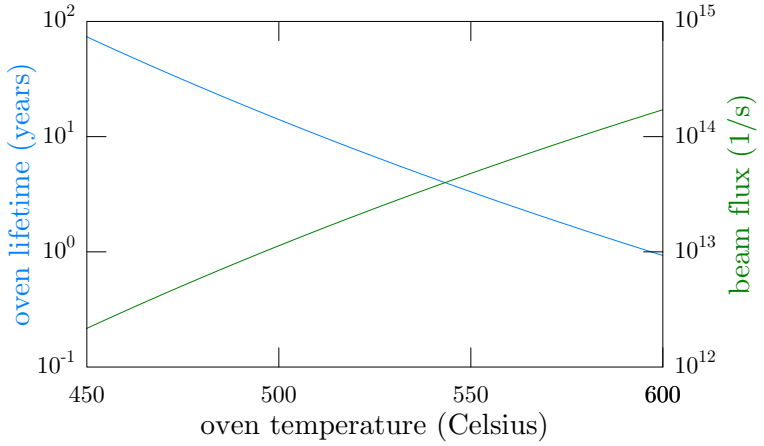

FIGURE 4.4. The estimated lifetime of the effusive oven under continuous operation (blue) and atomic beam flux delivered to the top MOT trapping region (green) as a function of temperature. We make conservative estimates for each (see text), so the curves represent a lower-bound of expected values. Running at a cooler temperature drastically improves how long we can operate before recharging the strontium crucible.

molecular beam,

$$\begin{aligned} b_{\mathrm{col}}(v_z) &= A v_z f(v_z) \\ &= 2\pi A v_z \int_0^{a v_z/d} v_\perp f(\mathbf{v})\, dv_\perp \\ &= An \left(\frac{m}{2\pi k_{\mathrm{B}} T}\right)^{3/2} v_z \exp\left(-\frac{m v_z^2}{2 k_{\mathrm{B}} T}\right) \left[1 - \exp\left(-\frac{m v_z^2}{2 k_{\mathrm{B}} T}\frac{a^2}{d^2}\right)\right] \\ &\approx An\pi \frac{a^2}{d^2} \left(\frac{m}{2\pi k_{\mathrm{B}} T}\right)^{3/2} v_z^3 \exp\left(-\frac{m v_z^2}{2 k_{\mathrm{B}} T}\right), \end{aligned} \tag{4.5}$$

where A is again the area of the capillary and the final approximation assumes $d \gg a$. Note that the mean, average, and rms velocities of $b_{\mathrm{col}}(v_z)$ are skewed to be higher than those from the typical Maxwell-Boltzmann distribution [146, 147]. The total

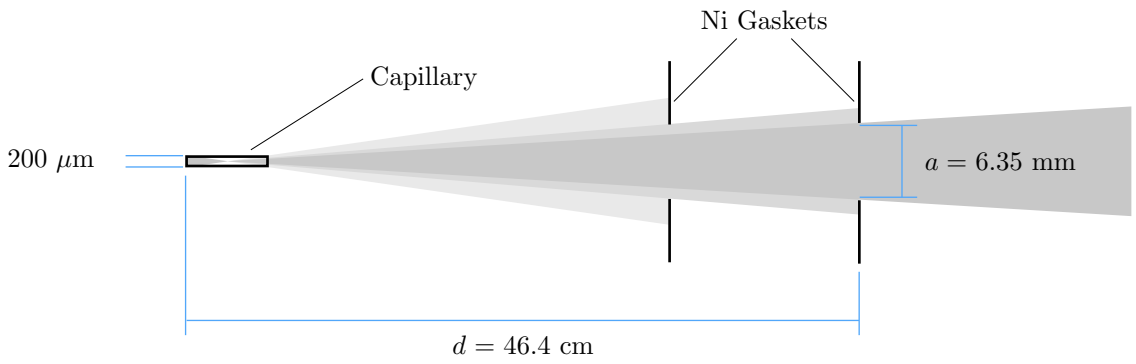

FIGURE 4.5. Sketch of atomic beam passing through a capillary and constricted by downstream nickel gaskets. Labeled dimensions are used to estimate the atomic flux delivered into the trapping region.

collimated flux is then approximately

$$\begin{aligned} \Phi_{\text{col}} &= N \int_0^\infty b_{\text{col}}(v_z) dv_z \\ &= N \frac{a^2}{d^2} \Phi_A, \end{aligned} \tag{4.6}$$

where we have made a conservative estimate by considering only atoms passing through the $N = 184$ capillaries (and ignored excess conduction through other gaps in the nozzle). The atomic flux delivered to the trapping region is plotted as a function of temperature in Fig. 4.4.

4.1.1.4. Atomic Beam Considerations

Because of the high vapor pressure, strontium atoms will readily stick to the cold surfaces of the chamber. Anything not directly in the oven's beam path is unlikely to accumulate large numbers of atoms, meaning that most windows and viewports will remain clear. We do, however, use a sapphire viewport (Larson VSZ-150-F2, exterior surface AR-coated for 461 nm) at the entrance of the Zeeman slowing beam to avoid the direct stream of strontium damaging a silica window. The atoms

will not react with sapphire [148], but will still deposit on the surface. To remove the condensed atoms, we heat the sapphire window, which is extended from the chamber on a 5″-long nipple. We wrap a one-inch-wide silicone rubber heater (Omega SRFG-108/10) around the 2.75-inch ConFlat (CF) joint, and heat it to 200°C, near the heater's maximum operating temperature. An infrared thermometer measures the temperature of the center of the window to be 175°C. Assuming evaporation into a perfect vacuum, the Hertz-Knudsen equation predicts the flux of atoms at temperature T leaving an area A to be the same as the flux of atoms passing through an orifice as in Eq. (4.2) [149]. In this limit, the evaporation rate is comparable to the flux of the atomic beam. In practice, we have noticed that running the oven at 600°C for several hours without loading a top MOT has produced a film on the sapphire window which takes a few days to evaporate.

To reduce strontium contamination on the sapphire window, we have an atomic-beam shutter which uses a magnetic vacuum feedthrough (Kurt J. Lesker DS275VPS). The shutter is actuated with timing pulleys and a stepper motor (ROB-09238, driven by the "EasyDriver" stepper motor, ROB-12779, both ordered from SparkFun), and can be controlled by the computer to be timed with the rest of the experiment. However, since opening or closing the shutter takes a few hundred milliseconds and creates substantial vibration, we typically close the shutter only when we do not intend to load any atoms into the top MOT for several minutes.

4.1.2. Chamber Design

Optical access to the atomic beam is provided via Kovar-sealed glass viewports (six of 0.75″ clearance on a 1.33″ CF flange [Larson VP-075-F1] and nine of 1.5″ clearance on a 2.75″ CF flange [Larson VP-150-F2], all AR-coated for 461 nm by

Spectrum Thin Films), most of which are attached to two spherical octagons (Kimball Physics MCF450-SphOct-E2A8 and MCF600-SphOct-F2C8). On the high-pressure side of the chamber, the smaller spherical octagon allows observation of the atomic beam and the option to cool atoms transversely as they exit the oven. We currently do not cool the beam in this manner, but this could be useful if a larger flux is necessary, as is the case for many groups who use strontium [17, 19, 150]. In the low-pressure spherical octagon, the six MOT cooling beams enter through the four ports diagonal to the atomic beam (in the plane of the optical table), a viewport at the top of the chamber, and the end of the pyrex cell (in the vertical direction). The only non-stock parts used in the chamber are the aforementioned oven pieces, a pair of nickel gaskets (discussed in more detail below), and the differential pumping tube (a 15-inch-long 1.33″ CF nipple).

Vacuum is maintained in our chamber using two rebuilt Varian Starcell ion pumps (Duniway RVIP-75-ST-M and RVIP-55-ST-M), a titanium sublimation pump (Duniway TSP-275-003), and two all-metal right angle valves (VAT 54032-GE02)—where we attach both sides of the chamber via temporary bellows to a turbomolecular pump for initial evacuation during bakeout. To simplify achieving UHV, we minimized the inner surface area and number of CF joints, and maximized conductance to the pumps. The titanium sublimation pump (TSP) is positioned so it will not sputter into any other pumps or onto any windows. We abstained from using dedicated pressure gauges, and instead used the ion pumps to monitor chamber pressures. Ideally, vacuum will only need to be broken when the strontium source is depleted. When this happens, an inline angle valve (Varian 9515052) can seal off the low-pressure side of the chamber to maintain vacuum during the refilling process.

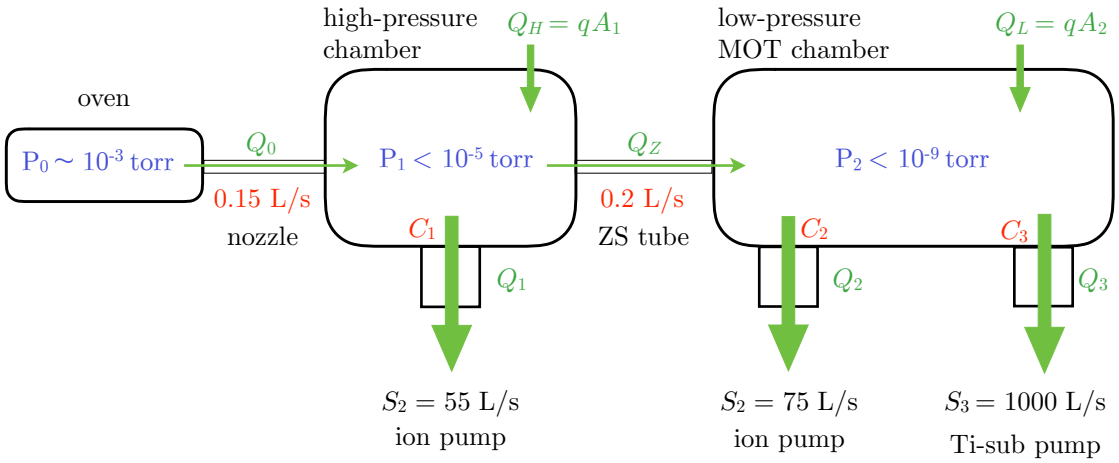

FIGURE 4.6. Model used to estimate expected initial pressures in the vacuum chamber. Conductances, in red, are calculated from chamber geometry, and throughtputs Q_L,Q_H, and Q_0 are estimated using expected outgassing rates in stainless steel [151]. From these and the pumping rates, S_i, pressures are calculated.

Before finalizing the design, we considered a model of the chamber with three pressure regions, depicted in Fig. 4.6. Conductances of the nozzle, differential pumping tube, and pipes leading to the pumps were calculated using Santeler's empirical formula [152], and outgassing rates $Q = qA$ were estimated in the chamber based on a post-bake value of $q = 10^{14}$ torr-L/s/cm^2 for stainless steel [151] over an area of $A_1 \approx 1400$ cm^2 and $A_2 \approx 4400$ cm^2 in the high- and low-pressure sides, respectively. Since the contents of the oven were not going to be baked before assembly, we assumed a higher outgassing rate from hydrogen diffusing out of the stainless steel [151], and calculated the expected initial rate for our oven and nozzle operating at $T = 550$°C (the outgassing area is roughly 160 cm^2, counting the capillaries). Pumping rates are 55 L/s, 75 L/s, and $\sim$ 1000 L/s for the two ion pumps and TSP, respectively (the TSP pumps at 20 L/s/in^2, which is multiplied by the inner surface area of the 6″ nipple). All these were combined in a system of molecular throughput and conductance equations (combinations of $Q = PS$ and

$Q = C\Delta P$, where Q is throughput, C is conductance, S is volumetric pumping rate, and P is pressure [144]). The resulting estimate for pressure in the MOT region was below 10^{-9} torr, and this value only decreases as hydrogen is depleted from the oven's steel. Thus the conductance in our differential pumping tube allows UHV operation even though the pressure in the oven region is quite high.

4.1.3. Assembly and Bakeout

During preparation and assembly of the chamber, components were handled with powder-free nitrile gloves and connected following standard procedure for CF flanges [153]. Stock vacuum parts from vendors made from 304L or 316L stainless steel were inspected for cleanliness and baked in air at 450°C for 24 hours. High temperatures increase the rate at which hydrogen—trapped monatomically inside the metal during production—diffuses out of the metal [151], thereby reducing the quantity which can outgas in the future. Additionally, by baking in air, an oxide layer forms on the surface, which can act as a barrier to hydrogen recombining and leaving the metal (with a caveat that the oxide layer will break down and increase outgassing if the part is subsequently heated to 250°C) [154]. After this pre-bake, parts were cleaned with spectroscopically-pure acetone and methanol, dried with canned air, and wrapped in UHV-grade aluminum foil. Custom-made parts, meanwhile, were machined with sulfur- and silicon-free cutting fluid (we have used Trim-sol and Kool Mist 78), and then sonicated in soapy water (Alcanox), deionized water, and isopropyl alcohol before final cleaning in the same manner as the stock parts. We chose not pre-bake the 316L stainless steel components of the oven since its normal operation quickly reduces the hydrogen content anyway.

Because the two sides of the chamber are mated via a long 1.33″ CF nipple, we built the chamber on an 80-20 support frame to increase rigidity and mobility. After separate construction, the two halves were joined by sliding the 80-20 pieces under the high-pressure side until the CF flange at the end of the differential pumping tube met the 6″ spherical octagon. Preliminary alignment of the chamber was performed before the contents of the oven were filled: by looking into the chamber through the sapphire window and adjusting the position of the two halves of the chamber on the 80-20 frame, we tried to make all circular features concentric—in particular, the two nickel gasket apertures, light from the far end of the oven, and the sapphire window. (Alignment was rechecked after bakeout with the oven activated to produce blackbody glow, confirming line of sight between the window and oven.)

Parts exposed to atmosphere have water vapor adsorbed on the surface, so achieving UHV requires an extended bakeout while evacuating with a turbomolecular pump. The 80-20 support frame enabled us to relocate the chamber during bakeout (this is necessary because we have space constraints with flammable materials above our optical table). We wrapped heater tape around the chamber and contained the heat using a combination of tented UHV aluminum foil and firebricks. We monitored the temperature with 16 thermocouples and used variable transformers to drive the heaters and brought the chamber to a target of 200°C. Changes in temperature were applied slowly (we aimed for less than 1°C per minute) to suppress stress from thermal expansion in CF joints and windows, and special care was taken to avoid overheating temperature-sensitive components, listed in Table 4.1. Since the TSP cartridge is at the center of a 6″ nipple inside the chamber, it is cooler than the surrounding walls during bakeout. Molecules outgassing from the walls adsorb on the filaments, only to outgas later when the pump is activated. To prevent this, we heated each filament by

Item	Manufacturer	Part Number	Limit (°C)
Right-angle valves	VAT	54032-GE02	300
Inline valve	Varian	9515052	450
Kovar windows	Larson Electronics	VP-150-F2	400
Sapphire window	Larson Electronics	VSZ-150-F2	450
Pyrex cell	ColdQuanta	CQMC0006	300
Magnet wire	MWS	40466	240
Epoxy	EpoTek	353ND	225
Ion Pumps	Varian	Starcell	350

TABLE 4.1. Maximum temperatures of various vacuum chamber components. The target temperature during bakeout is 200°C, but the ion pumps should not be switched on at this temperature since their operational max is 150°C. The most sensitive parts are the epoxy and polyimide-coated magnet wire used in the anti-Helmholz coil.

applying 30 A of current (we have three filaments and can only apply current through one at a time, so we switched every few hours).

After baking and pumping for several days, the pressure (measured near the turbo pump) approached 10^{-7} torr, and we flashed each TSP filament at 40 A for one minute. Several hours later, we cooled the chamber to a temperature that was safe to turn on our ion pumps, keeping the rest of the chamber a bit hotter than the pumps so that any outgassing was pumped away rather than adhering to the walls of the chamber. Next, we heated our strontium oven to 400°C (to outgas that part of the chamber while the turbo pump was still attached) and monitored the pressure using the ion pumps. (The first time we did this, the pressure rise was so sharp we thought a leak had formed. After cooling to room temperature and pumping overnight, however, the pressure dropped once more. Presumably, the rise in pressure was initial outgassing from the untreated stainless steel in the oven or a pocket of gas was released from behind the tightly fitting crucible. To assure ourselves that everything was okay, we performed a short bakeout and observed that the pressure

did not rise as abruptly when turning on the oven again.) We then cooled the chamber to room temperature and activated one of our TSP filaments for two minutes at 45 A. Finally, we sealed off the chamber using the right-angle valves and moved it back onto the optical table. Final readings of both ion pump controllers were off scale, meaning the pressure was well below 10^{-9} torr. Several years after sealing the chamber and regularly cycling the oven, the ion pumps measure pressures of about 1.0×10^{-9} torr and 6.5×10^{-9} torr in the low- and high-pressure sides, respectively, with the oven at 500°C (this is without engaging the TSP since the final bakeout).

In the future if vacuum needs to be broken (to refill the oven, for example), it might be possible to avoid such extensive bakeout. First of all, the inline valve can be closed to isolate the two halves of the chamber. The side to be opened can then be filled with a dry gas (e.g. argon) to atmospheric pressure using a venting valve in our turbo pump. The uppermost viewport can be replaced carefully by an argon source (with little agitation, hopefully no moist air will enter the chamber), and slight positive pressure applied after a lower seal is broken. If a bakeout of the high-pressure side of the chamber is in the end necessary, it is reasonable to do this portion in place and not move the entire chamber off the optical table as we did in the initial baking process.

During the process of assembling our chamber, we had difficulty achieving a reliable seal with nickel gaskets in a CF-flange assembly. (Since copper reacts with strontium, we have to use nickel gaskets in areas which are exposed to high beam flux [140]). Gaskets for smaller, 1.33″ CF flanges were purchased from MDC and sealed nicely, but larger, 2.75″ CF gaskets for the beam constriction apertures—blanks of Ni-200, purchased from Grass Manufacturing—were problematic. In the first assembly, small leaks detected at one flange improved after baking out, and it

seemed as if Ni flowed on a longer timescale than Cu, and that heating the gasket helped. However, after subsequent reassembly, leaks were still problematic, even after bakeout. We eventually realized that the gaskets were work-hardened (during the cold-rolling and stamping process), and that pressure from a CF knife edge only exacerbated this effect. Inspecting used gaskets, we found that dimples in a gasket's surface were pushed in by the knife edge and that the metal did not flow as well as copper. We settled on buying cold-rolled, water-cut gaskets which were slightly oversized. To prepare them for use, we machined them to the appropriate CF size, annealed in air at 1500 °F for 5 minutes, and then buffed off the resulting oxide layer using scotch pads. The first two gaskets prepared in this manner sealed nicely, and we have not had to break vacuum since. Incidentally (we discovered later) a Japanese group investigated the sealing reliability issue and developed a "concave" gasket [155].

4.1.4. Magnetic Coils

While not directly a part of the vacuum system, some experimental devices had to be determined during its conception. Because the top MOT is trapped inside the 6″ spherical octagon, we need a fairly large set of anti-Helmholtz (AH) coils that have clearance for the four-way cross flange. The coil forms attach to a pair of aluminum plates, which are connected to the spherical octagon on an exterior ring of tapped holes and provide stability by securing to the 80-20 support frame. Fig. 4.7 shows the support plates and one AH coil (not in its final position) to illustrate the geometry (note that the set of vacuum screws attaching the plate to the octagon in this particular photograph have washers which are too large to fit in the counterbored holes, but they ultimately do not protrude beyond the top of the plate). Clearly, the AH coil needs to be in place before the chamber assembly is finished and baked, and

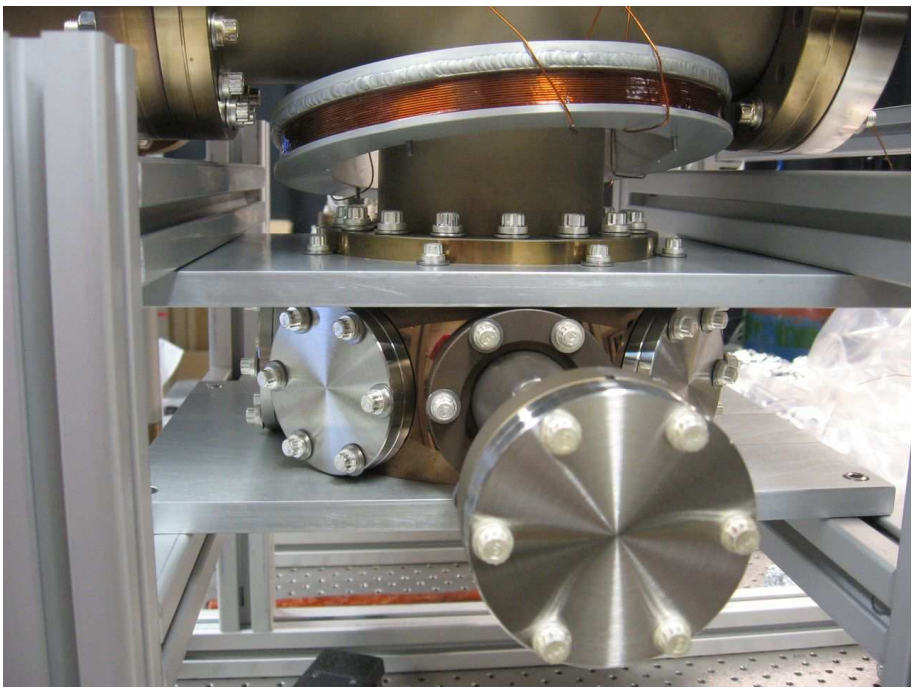

FIGURE 4.7. Photograph illustrating support structure for the 6″ spherical octagon and science cell. Aluminum plates are attached to the octagon and the 80-20 frame (the screws are countersunk in the final configuration), and the top-MOT anti-Helmholtz coils can clear the outer flange dimension.

we follow UHV procedure in machining and assembling the forms to mitigate possible contamination of viewports during bakeout.

A coil form is created by carving a 0.5″-wide, 0.75″-deep channel into an 8″-outer-diameter aluminum annulus. A second channel for water-cooling is carved and later sealed by welding a ring and threaded cooling-line coupling block into place. The coils are wound using 20 AWG insulated magnet wire (single-build Polyimide, MWS P/N 40466), and have 308 turns each (roughly 22 layers of 14 wraps). High-temperature epoxy is painted on the wire as the coils is turned to secure it in place and to assist in removing heat from the center of the bundle. Assuming all turns are overlapped at the center of the bundle—giving an AH pair of radius 9.15 cm and separation 11.25 cm—the axial field gradient is approximately $\partial B_z(I) = 3.83\, I$ G/cm,

where I is the applied current. The resistance of a coil, meanwhile, is estimated to be 6.3 Ω (constructed coils end up agreeing with this estimate, and we measure total resistance values of the two coils in series to vary between 12.0 Ω and 13.7 Ω because their temperatures change with operating current).

The trapping region in a MOT is roughly defined by the location where the Zeeman shift matches the laser's detuning, and an atom at rest is therefore resonant with the light. Setting the velocity equal to zero in the effective detuning, Eq. (A.3), we find the MOT's radius (along the axial direction of the AH coils) to be

$$R_{MOT} = \frac{\hbar\Delta}{\tilde{\mu}\,\partial B_z}, \tag{4.7}$$

where $\tilde{\mu} = \mu' - \mu = \mu_B(m'_{J'}g'_{J'} - m_J g_J)$ is the cooling transition's effective magnetic moment. Because the blue trapping transition in strontium has a relatively broad 30-MHz linewidth, a large field gradient is desirable to be able to form a tight MOT.

We use a Kepco ATE 100-10M power supply to drive the coils in series, and the 100-V maximum corresponds to a maximum field gradient of roughly 28 G/cm. The power dissipated in these coils is significant and requires water-cooling with a recirculating refrigeration bath. For these, we use two 400 W Neslab chillers—one for each coil—and isolate vibration on the cooling line by potting a few loops inside a concrete-filled plastic tub. To prevent possible overheating (we would be forced to break vacuum if the upper coil's insulating coating degrades to the point of shorting), we use a protection circuit which only enables current if signals from two flow switches (McMaster-Carr 2371K4) indicate that cooling is enabled. Originally, thermal switches (Digi-Key 480-3221-ND) were also in place, but a five-minute epoxy holding them to the coil forms failed with temperature cycling and they were not reinstalled. The Kepco supply, however, acts as a nice fail-safe since

it will automatically shut down if the load creeps beyond 100 V. This corresponds to a current of roughly 7.4 A, and the temperature of the wire is measured to be 160°C with an infrared thermometer in this extreme limit (compare this temperature to the wire's maximum rated temperature of 240°C given in Table 4.1). We typically load a top MOT using 6.8 A, corresponding to a field gradient of about 26 G/cm.

Anti-Helmholtz coils for the bottom MOT are positioned around the pyrex cell so that their longitudinal axes point in the north-south direction. We use a pair of coils wrapped around a machined Delrin form, which was decommissioned from a previous setup in the lab [123]. There are 216 turns per coil, and the coil diameter and separation are roughly 40 mm and 50 mm, respectively. These provide a field gradient of $\partial B_{\mathrm{z}}(I) = 24.6\, I$ G/cm.

4.1.5. Zeeman Slower

If we try to load atoms directly from the thermal beam into a MOT, only a subset will be trapped. The MOT's capture velocity is the limit where the energy dissipated by a trapping beam matches the atom's kinetic energy, and can be approximated by [156]

$$v_c = \sqrt{\frac{r_c F_{\mathrm{rad}}}{m}}. \tag{4.8}$$

Here r_c is the trapping radius, typically given by the size of the MOT beams, and F_{rad} is the radiative scattering force. Assuming a trapping radius of 1 cm and maximum force, $F_{\mathrm{rad}} = \hbar k \Gamma/2$ (which should, in principle, be smaller because the transverse MOT beams are at an angle to the atomic beam), the capture velocity is about 80 m/s. If we integrate the expression for the collimated beam flux up to this capture velocity [instead of to infinite velocities, as in Eq. (4.6)], the resulting flux of atoms

that can be trapped (given an oven operating temperature of 500°C, for example) is only 2.2×10^{10} atoms/s, or about 0.2% of the total collimated flux.

To increase the loading rate, we can use a counter-propagating slowing beam which interacts with the atoms as they travel from the oven to the trapping region. This beam is red-detuned in the same manner as Doppler cooling, but some tactic must be employed to enable continued interaction with the atoms as they slow and fall out of resonance with the light. One option is chirping the laser frequency to tune the laser and follow the shifting resonance [147, 157], and another alternative tunes the Doppler shift through a creative series of reflections of the slowing beam [158]. The simplest method experimentally is to use the Zeeman effect to spatially tune the atoms so they continually interact with a fixed laser frequency [2]. For a given laser detuning and magnetic field, a particular velocity class of atoms will scatter light and slow down. As the atoms proceed, the changing field decreases the velocity at which they are resonant. Additionally, a new group of atoms (which previously were not interacting with the light) will begin to be slowed as well. In this manner, a Zeeman slower effectively sweeps through the velocity distribution of the atomic beam, bunching atoms into the same velocity class.

Assuming the maximum scattering rate $F_{\max} = \hbar k \Gamma/2$, the minimum slower length required to bring atoms to rest from velocity v is determined by basic kinematic equations. To stop ^{88}Sr atoms with $v = 400$ m/s, this distance is less than 10 cm, which—because of the broad linewidth and higher-energy 461 nm photons—is much shorter than for alkali atoms. In practice, however, the length of a slower needs to be longer than this minimum distance, because it assumes perfect resonance. Small imperfections in the magnetic field profile cause decreases in the scattering force, and the atoms will not stay on the designed velocity profile, eventually becoming

unaffected by the slowing light. So to effectively slow atoms, the field should change monotonically and meet the condition,

$$\left|\frac{dB(z)}{dz}\right| < \frac{(\hbar k)^2\Gamma}{\tilde{\mu}\, v(z)}. \tag{4.9}$$

This expression is found by writing $a(z) = v(z)\, dv/dz$ and finding dv/dz by equating the Zeeman and Doppler shifts [159].

The magnetic field is commonly made using coils wrapped around the axis of the atomic beam in a tapered solenoid [160], which requires careful simulation and construction. In this geometry, the slower is an enduring structure built around a section of the vacuum chamber and needs to be bakeable. Furthermore, the assembly must be water-cooled because high currents are required to produce the magnetic field. These difficulties can be circumvented by using a permanent magnet Zeeman slower, and we chose to follow the design of a transverse slower in Refs. [161] and [162]. Such a slower consumes no energy and is easily adjusted in the future. The design can even be changed entirely if desirable; permanent-magnet Zeeman slowers have become popular in the last few years, and have evolved since we chose our design (for example, there are permanent magnet slowers producing longitudinal fields [163, 164], slowers which cleverly mount the magnets [165, 166], and even a computer-controlled slower which allows dynamical configuration for multiple atomic species [167]).

Fig. 4.8 shows our completed Zeeman slower. Stacks of magnetic dipoles are glued in color-coded mounts and are positioned using threaded brass studs. The surrounding box is made from nickel-plated cast iron, and is normally closed on all sides. We use combinations of three different thicknesses of $5/8''$-diameter N42 neodymium magnets (K&J Magnetics DA1, DA2, and DAH1) to create individual dipole stacks. Locations and dipole moments of the magnets are given in Table 4.2.

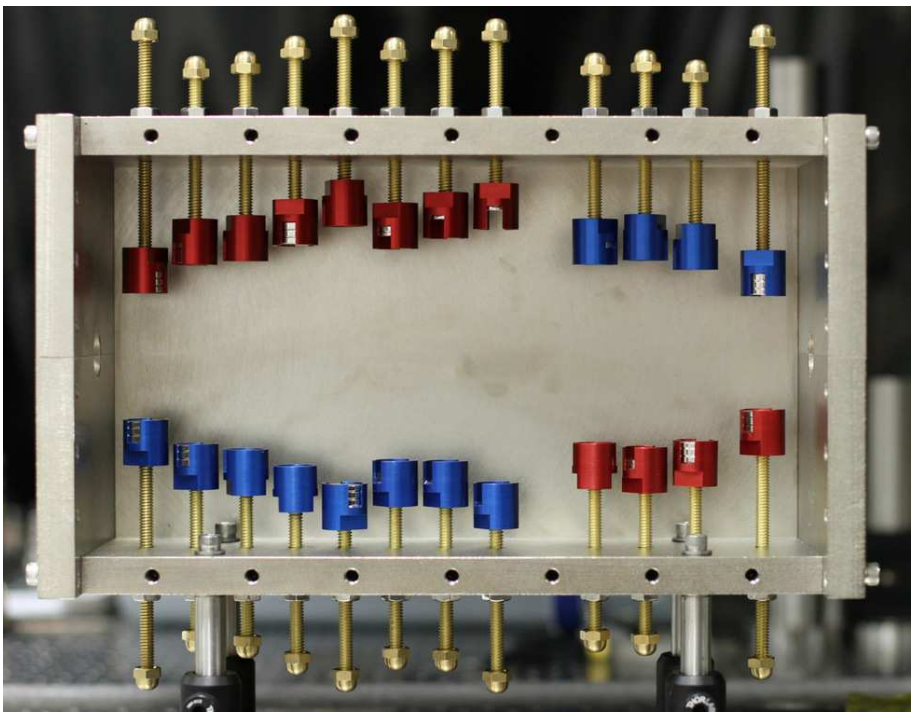

FIGURE 4.8. Photograph of the permanent-magnet, transverse-field Zeeman slower. The atomic beam enters from the left and experiences a monotonically increasing magnetic field. Magnet holders are color-anodized to indicate polarity (the field points from red to blue)

(We chose to use cast iron to better mimic the results in Refs. [161] and [162], but a mild steel would also work well and be much easier to machine.)

As evidenced by the color reversal, the magnetic field switches polarity in the latter half of the slower. This zero-crossing feature allows the use of smaller magnetic field magnitudes, but would be problematic for atoms with magnetic sublevels in the ground state. Since the resonance condition matches the tuning of only one pair of excited- and ground-state sublevels, an atom ending up in a different ground-state sublevel after the degeneracy at zero field will no longer be slowed. A zero-crossing slower works nicely for ^{88}Sr, though, because $S = L = J = I = 0$ in the ground state.

Note that this slower has a transverse magnetic field, so the cooling laser does not propagate along the atoms' quantization axis. This means that in order to couple

z (mm)	Stack thickness (in)	$\|\mathbf{m}\|$ (A-m^2)	x (mm)
0	1/10 + 2(1/8)	1.85	31
21	1/10 + 2(1/8)	1.85	42
42	1/10 + 2(1/8)	1.85	44
62	1/10 + 2(1/8)	1.85	50
83	1/10 + 2(1/8)	1.85	58
104	1/10 + 1/16	0.86	51
125	1/16	0.33	55
146	1/16	0.33	62
163	no magnets		
187	1/10	0.53	45
208	1/10 + 1/16	0.86	46
229	1/10 + 2(1/8)	1.85	40
257	1/10 + 2(1/8)	1.85	28

TABLE 4.2. Magnet size, location, and strength in the permanent magnet Zeeman slower. Distances in the x-direction are measured from the axis to the center of the stack of magnets, and atoms travel through the slower in the $+z$-direction. Magnetic moments $|\mathbf{m}| = B_r V/\mu_0$ are calculated using $B_r = 1.32$ T as the residual induction in N42 magnets. Each position along the slower has two symmetric magnet stacks, so in total we use fifty-six magnets. The cast-iron shield has boundaries at $z = -20$ mm, $z = 277$ mm, and at $x = \pm 80.5$ mm.

from the $m_J = 0$ ground state to the $m'_J = 1$ excited state, the light needs to be linearly polarized so that it can be decomposed into σ_+ and σ_- components along the quantization axis. Because only one of these components interacts with the appropriate transition, ultimately half of the laser power does not contribute to the cooling process. The correct polarization of the laser is orthogonal to the direction of the magnetic field, because the other orientation would only drive π-polarized transitions (and the $m'_J = 0$ excited state is not tuned by the slower).

The field was modeled based on the positions of the dipoles and their first-order images in the magnetic shield, and measured at several locations (before the slower is placed around the vacuum chamber) to confirm accuracy. A subset of these data are shown in Fig. 4.9 along with the model which terminates at the shield boundary. For

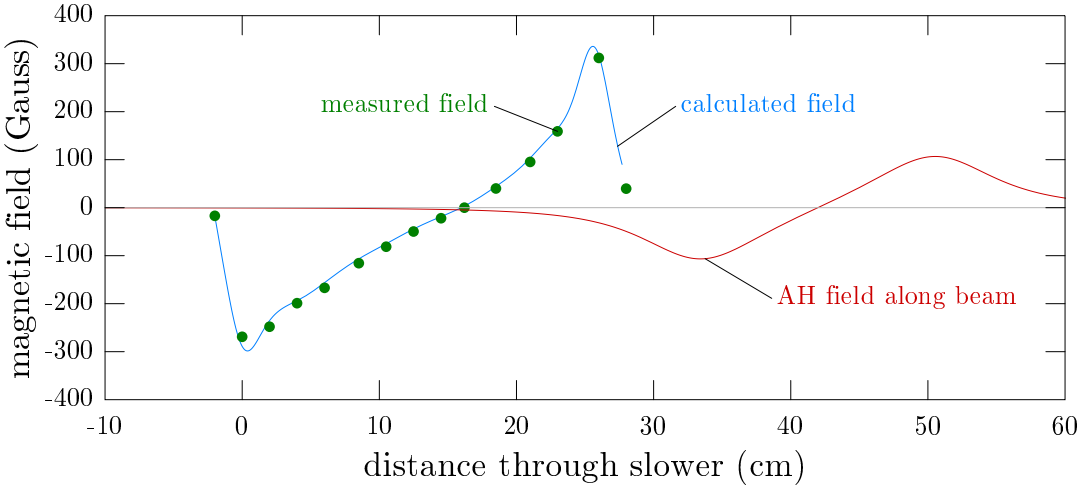

FIGURE 4.9. Magnetic field profile experienced by atoms as they pass through the Zeeman slower and into the trapping region. Note that the two curves represent different quantization axes: the Zeeman slower field is transverse to the atomic beam, and the anti-Helmholtz (AH) field points along the atoms' velocity.

reference, the field produced by the AH coils operating at $I = 7$ A is also plotted along the atomic beam's trajectory (elliptic integrals are used to calculate the off-axis AH field [168], but the effects of the chamber or cast-iron shield are not considered). The extreme field values are -300 G at the slower's entrance and $+330$ G at its exit. For a laser detuning of $\Delta = -500$ MHz, these correspond to capture and exit velocities of 424 m/s and 18 m/s, respectively. The final velocity is well within the range that can be caught by the MOT, and integrating the collimated velocity distribution up to the slower's capture velocity shows that 35% of atoms in the beam can now be loaded from an oven at 500°C—a substantial increase from 0.2% with no slower.

To conservatively estimate the required power, we assume that all atoms are slowed from capture to exit velocity, corresponding to about 41300 recoil events apiece. For 500°C, the beam flux is 3.9×10^{12}, and 140 mW of laser power is required in this estimate (including the fact that twice the power is needed for the transverse slower). Of course, not all atoms require this many photon recoil events in the slowing process,

and we still observe decent loading in our MOT for less than 20 mW of power in our Zeeman-slowing beam. Normally we use $\sim$ 45 mW in our beam, which would cool 1.3×10^{12} atoms/s in the above assumption.

Transverse heating of the atoms is dissuaded by slightly focusing the slowing beam [147, 161]. We use a pair of lenses (50.2 mm and 300 mm, Newport KPX082AR.14 and KPX112AR.14, respectively) to expand the beam (which has an initial waist of 0.38 mm) and focus it near the oven crucible. The beam requires a periscope to reach the level of the atoms, and we initially set this up beside the chamber to fine tune the position of the lenses. In particular, we checked that the beam would not clip on the aperture where the differential pumping tube connects to the trapping chamber (preventing unnecessary loss of slowing beam power) and that the beam was roughly the same size as the bundle of collimating capillaries at the oven's output. Once the relative positions were determined, we shifted the periscope and lenses into final position and directed the beam down the length of the chamber. As mentioned previously, the atomic beam deposits strontium on the sapphire window at the end of the chamber, and we overlapped the entry of the light with the visible buildup. Loading of the upper MOT is fairly robust to the exact positioning of the slowing beam, but we often check the pointing alignment using a camera looking into the small spherical octagon.

4.2. Laser Systems

Trapping and cooling alkali atoms, like rubidium (780 nm) and cesium (852 nm), is convenient because of widespread diode-laser technology at the necessary wavelengths. Manipulation of strontium atoms, however, demands several substantially different wavelengths which are unfortunately not as cheap or convenient

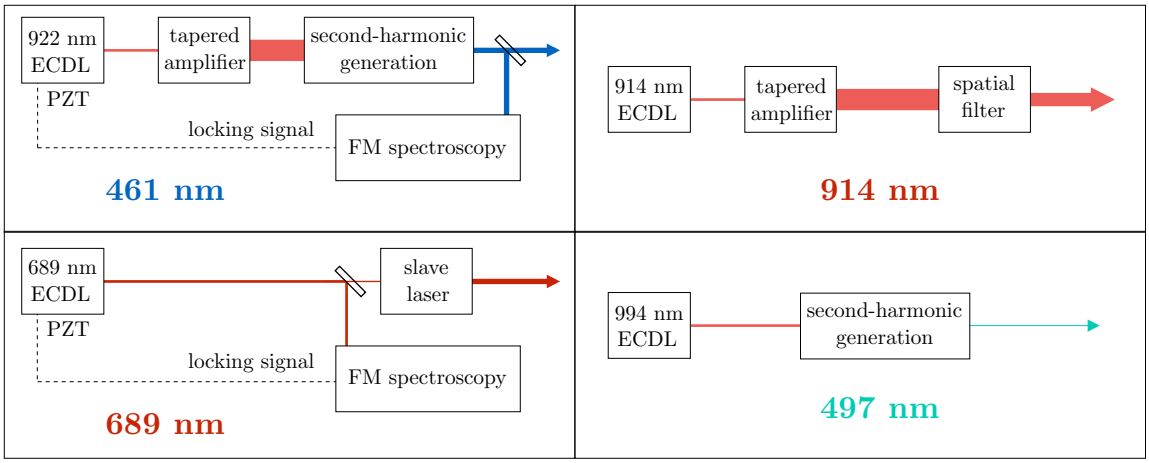

FIGURE 4.10. Basic block diagram of lasers required in the cold strontium experiment.

to realize. As a result, we have had to add several layers of complexity to create the required light. A basic block diagram of the four lasers we have made is shown in Fig. 4.10, and associated atomic transitions are labeled in Fig. B.1 in the appendix. The strong cycling transition, which we call the "blue MOT" transition, is at 461 nm; a secondary cooling transition, the $5s^2\,{}^1S_0 \longrightarrow 5s\,5p\,{}^3P_1$ intercombination line we call the "red MOT" transition, is at 689 nm; the "magic wavelength" for the red MOT transition is at 914 nm (this is different than the 813 nm magic wavelength used in the strontium clock, which operates on the doubly forbidden $5s^2\,{}^1S_0 \longrightarrow 5s\,5p\,{}^1P_0$ transition [19]); and a repumping scheme operates at 497 nm [17]. While each laser system is unique, there are several shared components and techniques that can be discussed individually. The starting point of each laser is the novel ECDL, which has been described in detail in Chapter III. In this section, light amplification, second-harmonic generation (SHG), and frequency stabilization and control will be addressed.

4.2.1. Tapered Amplifier

In situations where ECDLs do not generate enough power it is common to boost power by injection-locking a second diode laser [95, 169]. Here a 'master' seeds the lasing process in the injection-locked 'slave,' which can operate with higher intracavity powers. However, the *single-mode* power that can be achieved is limited by the geometry of the device. In particular, the transverse dimension of the gain medium must be smaller than roughly the wavelength of the laser light, or higher-order transverse modes will be supported within the cavity. To overcome this limitation in applications which require even more power, a diode with a tapered gain region—called a tapered amplifier (TA)—can be used [170–172] (often the term master-oscillator power amplifier [MOPA] is also used to describe the setup). Like ECDLs, TAs are becoming ubiquitous in atomic physics laboratories, and we worked with collaborators to create a tutorial in how to successfully implement them [173].

Inside the TA device, illustrated in Fig. 4.11(c), seed light is coupled into the single-mode rear facet, which has similar geometry to the active region of a laser diode. After some length, L_1, the gain medium begins to expand at roughly the diffraction angle of the design wavelength (the spatio-temporal dynamics of the gain medium are actually quite sensitive to the details of this expansion [174]). The light adiabatically expands over a length L_2, and is amplified due to the increased area in the diode's active region before exiting at the front facet. Higher-order transverse modes threaten single-mode operation, and the use of diffraction expansion rather than explicit waveguide structures helps suppress them. Additionally, cavity-spoiling grooves deter resonances in the injection portion, and it is likely that a lack of these geometric considerations added difficulty to early attempts in creating TA diodes [172]. Note that, unlike laser diodes, the front- and rear-facet are not coated

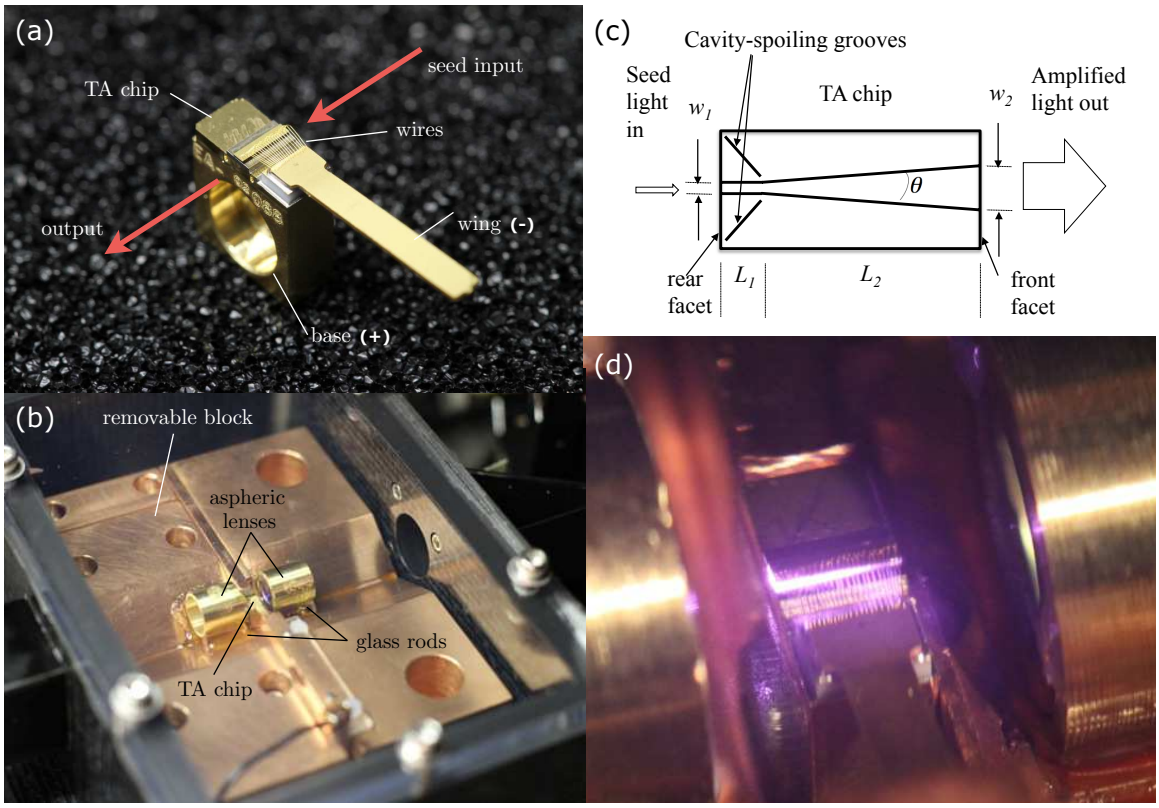

FIGURE 4.11. Details of the tapered amplifier (TA) chip and housing. (a) chip purchased from Eagleyard Photonics with relevant parts labeled, (b) our homebuilt housing for aligning optics, (c) schematic of the chip illustrating tapered gain medium, (d) TA operating at 922 nm. Note that in all but (c) the input side is to the right. Portions of this figure were adapted from Ref. [173]. Photographs by Dan Steck.

to be reflective: the TA is a single-pass device which can provide gain as high as 27 dB [175] and maintain the narrow-linewidth properties of a master laser [176].

We purchased TA chips from Eagleyard Photonics (EYP-TPA-0915-01500-3006-CMT03-0000), which have dimensions $w_1 = 3$ μm, $w_1 = 190$ μm, and $L_1 + L_2 = 2750$ μm. The chips have a nominal output power of 1.5 W at 3 A operating current and center wavelength of 915 nm, though the particular diodes we were sent are instead centered at 905 nm. A 50 nm FWHM, however, means they are able to amplify our master ECDLs operating at 914 nm and 922 nm. The TA chip, pictured in Fig. 4.11(a), comes in a C-mount package; electrical current is applied

through the base (anode) and an isolated 'wing' (cathode), which is connected to the semiconductor device with a series of small wires. The diode has TE polarization, meaning that the electric field is in the plane of the junction—or parallel to the optical table—and the diode's elliptical output is oriented vertically.

TA diodes are susceptible to catastrophic failure [173], and we follow several practices to reduce the chances that this occurs. First of all, as a semiconductor device, the TA can be shocked electrostatically, and is handled with the same grounding considerations as a regular laser diode [97]. It is also easy to accidentally create high power in the single-mode region and burn out the chip. This can happen from directly injecting too much seed power [177] or from a back reflection seeding the TA in reverse. These situations are avoided by being aware of the seed power, slightly tilting optics placed in the output beam, and by using a high degree of optical isolation after the TA. Somewhat more subtle, however, is the problem of amplified spontaneous emission (ASE). If the TA is powered on while it is not seeded, ASE generates light which travels both forward and backward in the diode, and can also cause damage at the interface between the tapered and single-mode regions. ASE is not harmful when driving the TA at low current (and can actually be quite useful as discussed below), but high current should not be used unless the presence of a seed and proper alignment is confirmed [178]. We employ a seed-monitoring photodiode (see Fig. 4.13[a]) and a relay to turn off the TA's current controller if the seed light is switched off or blocked [179].

We house the TAs in homebuilt structures, originally discussed in Ref. [177] and pictured in Fig. 4.11(b). The walls and lid are laser-cut from Delrin and acrylic, respectively, and the inside of the structure is sealed so that dust and debris do not land on the high-power output of the TA chip. Small air gaps resulting from

the kerf of the laser cutter are sealed with epoxy around the walls, and the lid and baseplate interfaces have a soft, silicon rubber gasket (McMaster 86435K452). Brewster windows are attached at the input and output (again sealed with a silicon gasket and oriented for light polarized parallel to the optical table). The main body is made from oxygen-free high conducting (OFHC) copper since it is both the positive electrical contact and the thermal reservoir for the C-mount diode, and it is mounted on two TECs (Laird 56460-501) wired in series for temperature regulation. The TECs are on an aluminum baseplate that has channels for optional water-cooling, which has not been necessary. The negative electrical contact, meanwhile, is created by clamping the chip's wing between a piece of copper and a polycarbonate spacer. We have thus avoided using a soldering iron in the vicinity of the chip. We control the temperature and current of the TA using modified versions of controllers used in our lab for ECDLs. The originals are described in previous theses [95, 123], and the modified versions have been documented on our lab website [179].

Coupling and collimating aspheric lenses (Thorlabs A230TM-B, $f = 4.51$ mm) are threaded into brass sleeves which are epoxied into place in a 120-degree 'v-groove' after alignment (see below). The output of a TA, however, is highly astigmatic (500–700 μm in our diodes), and the output lens will only collimate the fast (vertical) axis. The slow axis is refocused by the lens, and is separately collimated using a 75 mm cylindrical lens (CVI RCX-30.0-20.0-38.1-C-633-1064) outside the housing (see figure 6 in Ref. [172] for an illustration of the output beam geometry). If a TA chip needs to be changed, the output v-groove block can be removed to access the M2 screw securing the TA on the main OFHC base. Hopefully, the replacement diode will have a similar position as the original and alignment of the aspheric lenses will not have to be repeated anew.

Initial positioning and alignment of the aspheric lenses was performed by attaching the brass sleeves (with a five-minute epoxy) to posts hanging from a pair of towers which could be positioned using a three-axis translation stage. To align the seed laser into the TA, we adapted a procedure outlined in an Eagleyard application note [180] (another alignment procedure is also discussed in Ref. [173]). First, we used ASE straight out of the TA to roughly align the path along the row of holes where the master ECDL fiber launcher would be placed and then collimated the ASE with the input coupling aspheric lens (leaving it slightly diverging). We then put in the seed-light fiber launcher and used steering mirrors to couple the ASE into an optical fiber to ensure alignment. It was helpful to use a pair of anamorphic prisms to spatially mode-match the Gaussian fiber output with the roughly elliptical output of the ASE. (We magnified the vertical dimension with a 2:1 prism pair in the 922 nm TA setup and a 3:1 pair for the 914 nm. That was what we had on hand at the time, and both seem to work okay.) Next, we connected an ammeter to the TA, essentially using it as a photodiode to maximize the current produced by the seed light. For a seed power of 7.5 mW, initial current values were around a few μA, and by moving the coupling lens closer to the TA and using the steering mirrors—illustrated in Fig. 4.13(a)—current was maximized to be nearly 2 mA. After this preliminary alignment, we connected the current supply to the TA, switched it on, and finally made small changes in the alignment of the seed light and coupling lens to maximize the output power. At this point, the output aspheric lens was adjusted to minimize the vertical spread of the beam in the far field, and the cylindrical lens was inserted and positioned to finish the collimation. Note that the collimating lenses should be positioned while running the TA at the desired operating current since the astigmatism changes with current-dependent refractive index. With alignment optimized, we then secured the aspheric

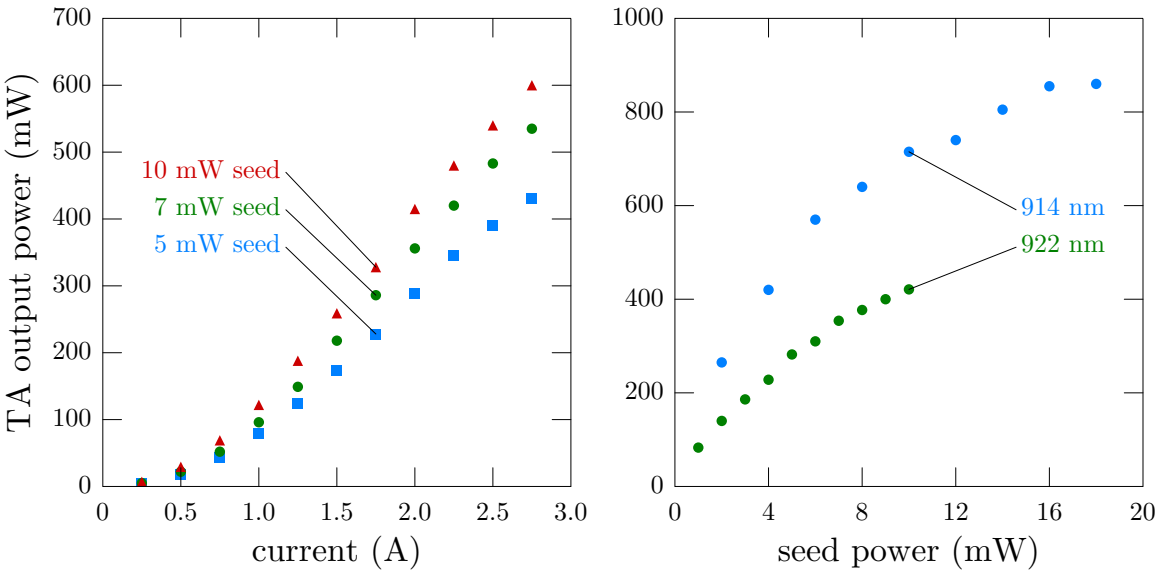

FIGURE 4.12. Output power of tapered amplifiers (TAs) as a function of drive current (left) and seed power (right). Seed power data are taken with an operating current of 2 A. Data for the left plot are taken with the 922 nm TA, which has lower output power than the 914 nm TA, as evidenced by the right plot.

lenses in place by placing 3 mm diameter glass rods between the brass sleeves and v-grooves and epoxying them in place (with Epotek 353ND). After allowing the epoxy to set for 60 hours, we broke the translation-stage assembly free from the brass sleeves (residue from the five-minute epoxy can be seen on the output lens in Fig. 4.11[b])

Output power from the TA depends on both the supplied current and the power of the seed light, as shown in Fig. 4.12. These data were taken before the aspheric lenses were epoxied in place and do not include any losses from sending the output through the optical isolators shown in Fig. 4.13(a). As mentioned previously, too much seed power could damage the TA (our chips are rated for a 50 mW maximum seed), and we ideally would like to operate at levels where the output power begins to saturate. For these diodes, we have found this to be around 15 mW. Note that the output power for the 922 nm TA is significantly lower than for the 914 nm TA. This is because, as mentioned previously, the TA's gain curve is centered at 905 nm

and it is less efficient at amplifying the 922 nm light (the same inefficiency in the master lasers explains why less seed power is available for that laser as well). We were able to tune the temperature of the chip, shift the gain curve, and increase the output power slightly. However, this required heating to several degrees above room temperature—potentially shortening the lifespan of the TA—and we elected to accept the reduced power output rather than operate in this regime. We typically run the 922 nm TA at 21.3°C with 2 A of current, which results in $\sim$ 350 mW of power after the optical isolators (when injected with about 10 mW of seed power). The 914 nm TA, meanwhile, produces nearly 900 mW of power after the isolators with a seed power of 13 mW and operating current of 2.9 A.

Finally, after setting up the TAs and working on the 461 nm doubling cavity, we noticed that a small amount of ASE—even with the diode seeded—appeared to couple back through the optical fiber and destabilize the 922 nm ECDL. We solved the issue by adding a second optical isolator to the output of the master laser before the fiber coupler.

4.2.2. Second-Harmonic Generation

At the time we started work on this project, laser diodes were not a viable option at 461 nm or 497 nm, which led us to develop lasers based on frequency doubling near-infrared ECDLs.[1] Crystals with $\chi^{(2)}$ nonlinearity can produce higher-order optical harmonics when illuminated with a single pump laser [183]. Since the power output of the second harmonic depends on the square of the power of the fundamental laser,

[1] As of this writing, 497 nm is still a difficult regime, but it is possible to find laser diodes which can operate at 461 nm. Nichida's NDB4216, for example, has a nominal wavelength of 450–460 nm and is not absurdly expensive, priced at $3300. It has been shown that using two of these diodes in a master-slave configuration can produce more than 100 mW of 461 nm power [181]. Additionally, it is possible to use a master ECDL to seed a cheaper, multimode slave to generate high powers for applications which are less sensitive to linewidth, such as Zeeman slowing [182].

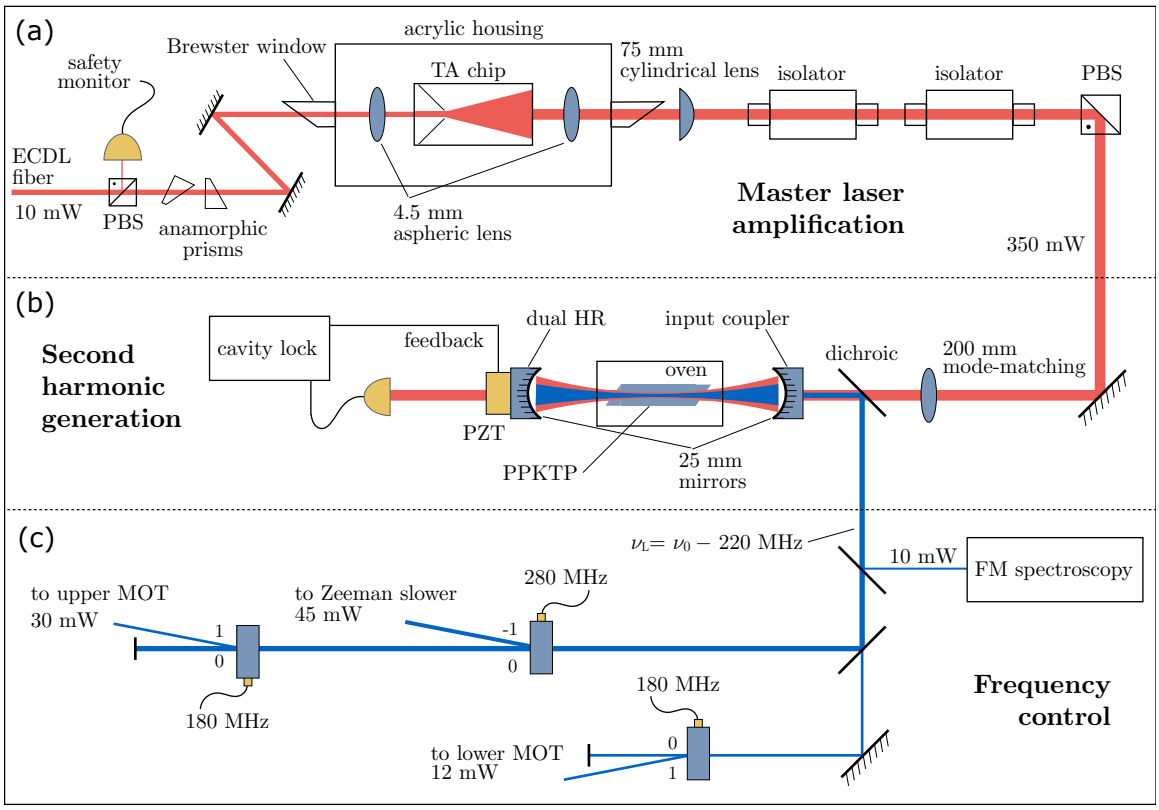

FIGURE 4.13. Schematic showing how 461 nm blue light is prepared for interaction with strontium atoms. A 922 nm master ECDL is amplified in a tapered gain medium (TA) before interacting with a periodically poled potassium titanyl phosphate crystal (PPKTP) in a build-up cavity to generate frequency-doubled light. The 461 nm light is sent to an atomic reference for frequency-stabilization of the master laser (see Fig. 4.15), and frequency adjustments are made using several AOMs.

it is advantageous to focus a Gaussian beam at the center of a crystal in an optical resonator [184, 185]. We chose to use a periodically poled potassium titanyl phosphate (PPKTP) crystal inside a linear build-up cavity, essentially a hybrid of two previously published SHG setups [186, 187]. The design will be discussed briefly here, but it is a rather complicated part of our experiment and will be covered in detail in Eryn Cook's thesis [188].

Fig. 4.13(b) shows a simplified schematic of our SHG setup for the 461 nm laser. Vertically polarized fundamental light comes from the 922 nm TA, and is coupled into

a linear cavity with a 200-mm mode-matching lens. The cavity mirrors have radius of curvature of 25 mm and are separated by about 5 cm, producing a fundamental waist of roughly 60 μm at the center of the 10-mm-long PPKTP crystal. The cavity's rear mirror is highly reflective for both wavelengths, while the input coupling mirror is AR-coated at 461 nm and coated for $\sim 9\%$ transmission at 922 nm for proper impedance matching (all coatings were performed by Spectrum Thin Films). The result is a Fabry–Pérot resonator at 922 nm and a double-pass configuration for the blue light, which is extracted by a dichroic mirror after exiting the cavity. The PPKTP crystal (5.5 μm poling period, manufactured by Raicol) is housed in a homebuilt OFHC oven, which is temperature-stabilized to be 29.7°C, and placed on a four-axis tilting kinematic mount (New Focus 9071) for position adjustments. The crystal is angle-polished (nominally 8 mrad) to allow the thickness of the final poling period to be adjusted by translating the crystal. This provides a mechanism to optimize SHG efficiency by controlling the phase relationship between the forward- and reverse-traveling blue light, although we never saw as clear an effect of this translation as in Ref. [186].

The length of the cavity is stabilized to be resonant with the fundamental by monitoring 922 nm transmission and feeding back to a piezo behind the rear cavity mirror. The mirror and piezo are rather massive, and the cavity is susceptible to being unlocked by mechanical noise. To improve utility, we have modified a circuit [189] that automatically reengages the lock, and our improved circuit is described in Ref. [188]. Locking the cavity has also been difficult because of thermal effects similar to what was seen in Ref. [190], and we frequently need to reposition the crystal slightly to find a location that both produces high blue power and remains locked. The dichroic mirror is slightly reflective for 922 nm, and we spatially separate the second harmonic using

a Pellin–Broca prism (not pictured in Fig. 4.13). Since small changes in the cavity's alignment change the pointing direction of the output beam, a pair of steering mirrors and irises are used to frequently realign the path through the Pellin–Broca. A well-aligned cavity can produce powers over 150 mW (at times the conversion efficiency has been over 50%, even with the poor spatial mode of the TA output limiting mode-matching into the cavity), but the thermal effects seem to be more significant when more blue light is being produced. We typically have 120–150 mW of useable blue power to send to the experiment, and we have found that atoms are still efficiently slowed and trapped with as little as 100 mW total power (this is the power measured before the first beamsplitter after the cavity in Fig. 4.13, so it includes all necessary power for stabilizing the laser and loading both MOTs).

Frequency-doubled light for the 497 nm laser, meanwhile, is created using a periodically poled lithium niobate (PPLN) crystal (Covesion MSHG976-0.5-20, mounted in an oven, PV20). Much less second-harmonic power is required at this wavelength than the main cycling transition since the saturation intensity of the $5s\,5p\,{}^3P_2 \longrightarrow 5s\,5d\,{}^3D_2$ transition is only 2.2 mW/cm^2 (compared to 42.7 mW/cm^2 for the 461 nm line). Additionally, we only need to send a single beam into the trap to influence population and lifetime, and that beam does not need to be much larger than the MOT (for example, 500 μW would be enough to saturate a MOT with 5 mm diameter). Because of the low power requirements, we do not use a TA to amplify the output of the 994 nm master ECDL, and we have constructed a linear cavity using a spare set of mirrors which were coated for the 922 nm SHG process. So, while certainly not optimized, the cavity is good enough to produce a small amount of 497 nm light.

4.2.3. Frequency Stabilization

To ensure that a laser is tuned to an atomic transition, absorption is monitored in a reference sample. Typically, Doppler-free lineshapes are created through a process called saturated-absorption spectroscopy (SAS), in which an opposing pump-probe scheme isolates a particular velocity class of the atomic sample [129, 191]. A dispersive lineshape, convenient for electronic feedback, can be created by modulating the frequency of the laser and using lock-in amplification to analyze the signal from a photodiode (frequency modulation [FM] can be performed through electro- or acousto-optic effects [192] or—in the case of laser diodes—through controlling the applied current [123]). Alternatively, a clever use of light-induced birefringence can create Doppler-free lineshapes in a process called polarization spectroscopy [193], and combining this with a magnetic field (used to create a dispersive lineshape in the dichroic-atomic-vapor laser lock [DAVLL] scheme [194]) yields lockable signals which require no frequency modulation [195]. This Doppler-free DAVLL technique can be used to stabilize lasers to strontium in a "see-through" hollow-cathode lamp [196], but such an atomic reference is costly. We instead, use a different method to produce strontium vapor samples and stabilize the lasers with FM spectroscopy.

4.2.3.1. Heat-Pipe Vapor Cell

As discussed in Sec. 4.1, strontium needs to be heated to several hundred Celsius to create an appreciable vapor pressure and it reacts unfavorably with vacuum viewports and copper gaskets. Thus, simple glass vapor cells, like those typically used for alkali atoms, are not a viable option. Instead, we have made heat-pipe vapor cells [197, 198] that use an inert buffer gas to prevent Sr vapor from reaching windows. If the mean-free path of the buffer gas is small compared to the distance between a

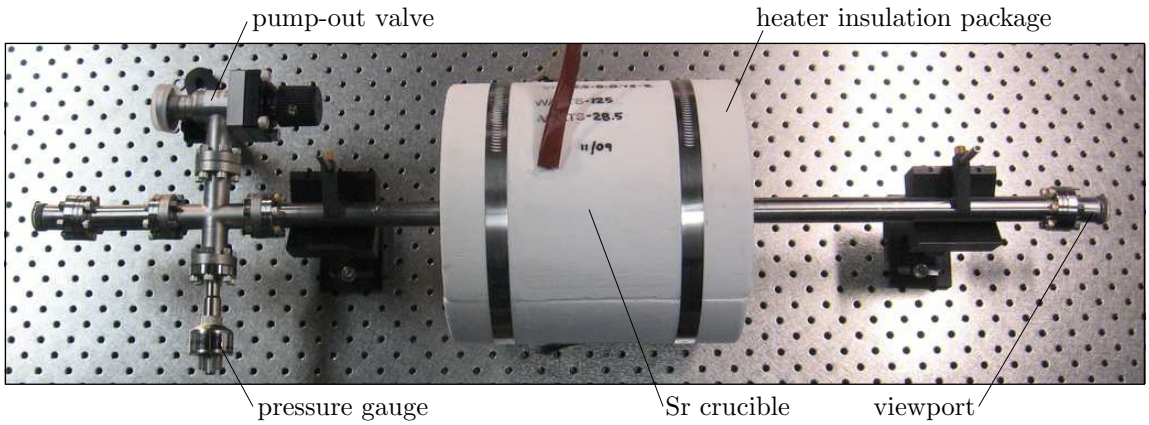

FIGURE 4.14. Photograph of a completed heat-pipe vapor cell. Radiative heaters at the center of an insulation package heat strontium contained in a nickel crucible, and an argon buffer gas prevents strontium vapor from reaching the windows. For a scale reference, the holes in the optical table are on a double-density 1″ grid.

central heated region and the windows, the Sr gas is well-contained. One of these devices is pictured in Fig. 4.14. Using an argon-filled glove bag as in Sec. 4.1.1.1, several grams of Sr were loaded into a 10-cm-long nickel crucible which has a 0.25″ hole in the base and end cap to pass light. A fine, nickel mesh is also placed inside the crucible to encourage wicking back into the center, but this is not needed unless the Sr is actually melted. The crucible was placed in a smooth-bore, 0.62″ ID stainless steel pipe, roughly centered between two viewports (Larson VPK-075-F1). One viewport is attached to a 1.33″ CF flange that was welded by the UO machine shop to be tilted by 3° (right side in the picture) to suppress resonant reflections between the two windows. Nickel gaskets are used in joints nearest the Sr sample (MDC 191060), and we did not have the same troubles with these that we had with the gaskets in the UHV chamber (Sec. 4.1.3). A compact vacuum valve (HPS CV16-C1C1-MKKCV) and thermocouple sensor (Duniway DST-531) allow us to pump out the vapor cell and monitor the pressure, respectively.

Heat is applied to the Sr sample using two semi-cylindrical ceramic heaters wired in series (Thermcraft RL106-S-L, with insulation package VIP-2.5-8-0.75-2). The signal from a type-J thermocouple is monitored by an on-off temperature controller (Love Controls TCS-4011), which we originally used to directly switch voltage from a Variac to drive the heaters. This simple setup was problematic since the relays inside the Love controllers failed after running the heaters for about a week (they failed in the closed position, and the temperature would run away to whatever maximum that could be attained by the Variac voltage). Initially, we thought this was an issue of switching inductive loads, which would cause arcing as the mechanical component switched between leads, eventually welding the switch in place. We upgraded the relays inside the Love controllers (to something with a higher load capacity that would fit the same printed circuit board [PCB] footprint, Omron G2RL1EDC12) and added transient-voltage suppressors (TVS) to limit the strength of the inductive kick. This seemed to solve the issue, but the relays again failed after about three months of operation. This time, however, we realized they had reached their rated maximum number of switching events. The final iteration—which has worked without issue for several years—used the Love controller to switch a 5-V dc signal that controls a solid-state relay (SSR) with built-in varistor (Omron G3NA-220B-DC5-24), which in turn switched the Variac voltage. This is the same temperature controlling scheme used with the Sr oven in Sec. 4.1.1.1.

We attached a turbomolecular pump to evacuate the chamber and used the venting valve to backfill with argon gas. Originally, we did not bake the assembly, but after it was sealed for several months, outgassing caused the pressure to rise and we performed a gentle bake at 150°C for about a week. It was difficult to control the pressure of the argon during backfilling, but we ended up with about 10 mTorr in

one heat pipe and 140 mTorr in the other. When we turned on the heaters, however, the pressures rose due to outgassing (as high as 450 mTorr in one of the pipes) but eventually fell to be about 25 mTorr in each chamber, presumably because the Sr vapor was acting as a getter pump [199].

4.2.3.2. Frequency-Modulation Spectroscopy

A laser can be stabilized to an atomic reference in a rather simple SAS setup, such as the one we used in Fig. 3.5(b). The pump-probe interaction creates Lamb dips [145] on a Doppler-broadened background, and through FM techniques, the laser can be locked to them. However, the presence of the Doppler-broadened background means there is a slight offset in frequency between the locking point and the actual atomic resonance. This by itself would not be so annoying, but the difference is coupled to the laser's power and to background light levels, meaning the actual frequency of the laser would drift slightly in an uncontrolled manner. In SAS, the Doppler-broadened background is commonly removed by using differential photodetection on two probe beams [129], where only one of them has interacted with atoms affected by the pump. This method is not easily realized in our setup because the heat pipe is long and thin, making the necessary beam geometry difficult to achieve. Instead, we use a collinear pump-probe geometry and an extra layer of lock-in detection to remove the background. A diagram of the setup we use to stabilize the 461 nm and 689 nm lasers is shown in Fig. 4.15.

We use an AOM to chop the pump beam at 175 kHz, thereby modulating the saturation of the atoms. The probe's absorption spectrum will always have the same Doppler-broadened background, but the Lamb dips are only present half the

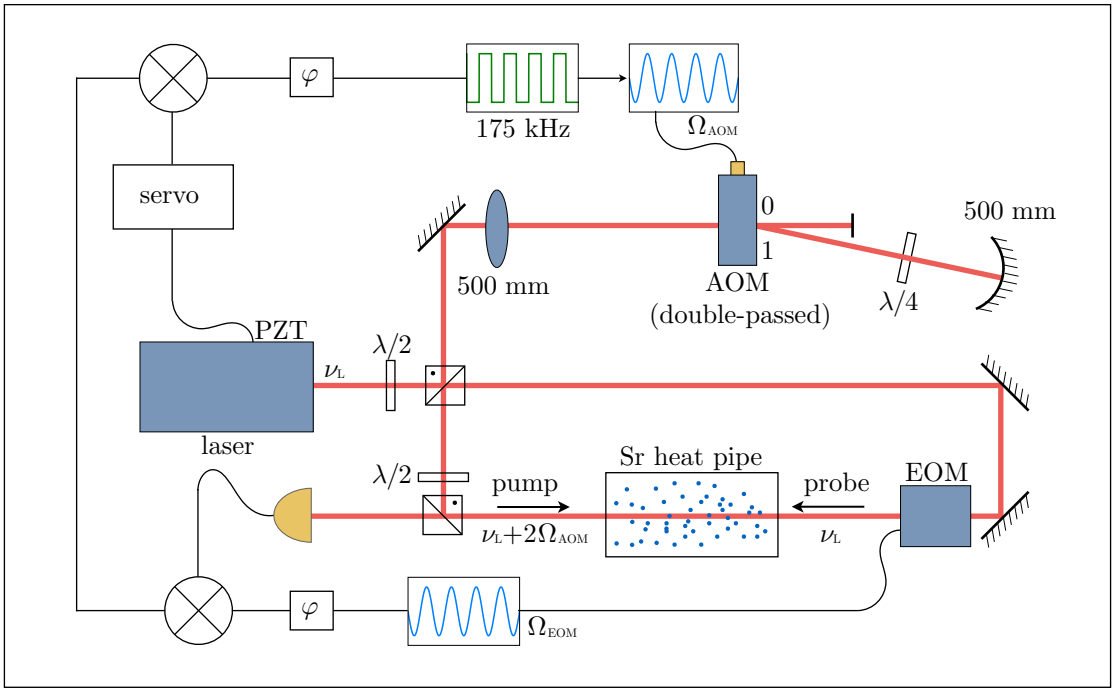

FIGURE 4.15. Schematic of frequency-modulation spectroscopy used to stabilize the blue 461 nm and red 689 nm lasers to an atomic reference. Values for the blue setup are $\Omega_{\mathrm{AOM}} = 220$ MHz and $\Omega_{\mathrm{EOM}} = 8.773$ MHz, while they are $\Omega_{\mathrm{AOM}} = 80.5$ MHz and $\Omega_{\mathrm{EOM}} = 3.161$ MHz for the red.

time. Lock-in detection at this frequency therefore isolates the non-broadened atomic features, and all that remains is turning these into lockable signals.

We do not want to modulate the frequency of either of our lasers using the master diode's current (for the 922 nm master this would complicate locking the SHG cavity, while we want the frequency of the 689 nm laser to be as stable as possible to best interact with the narrow intercombination line), so we instead use an electro-optic modulator (EOM) to modulate the phase of the probe. Driving the EOM with frequency Ω_{EOM} puts sidebands on the laser. Interference of the sidebands and carrier at the photodetector create a signal, which—after locking in on frequency Ω_{EOM} and selecting the correct phase shift—when swept across a resonance produces a dispersive lineshape [192].

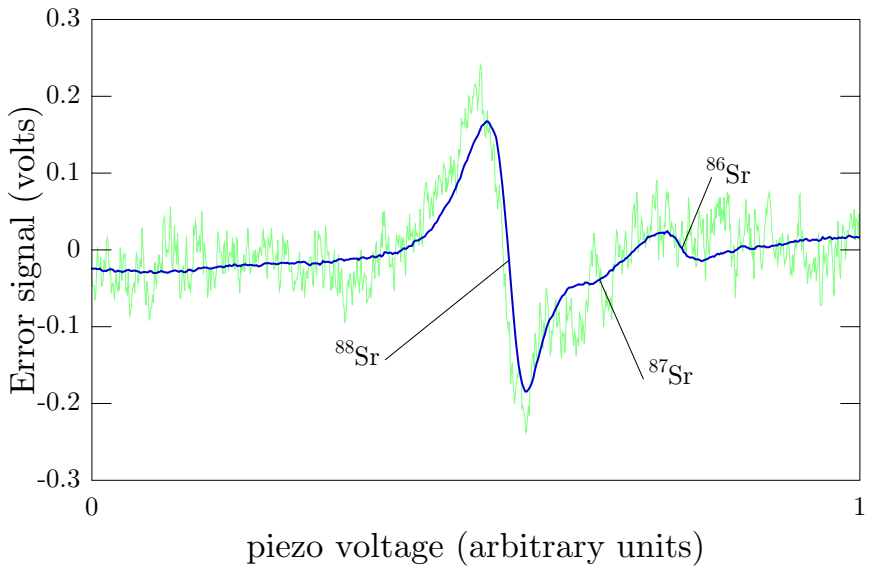

FIGURE 4.16. Error signal produced in FM spectroscoy of the $5s^2\,{}^1S_0 \longrightarrow 5s\,5p\,{}^1P_1$ "blue MOT" transition in strontium. Both a single trace (light green) and averaged signal (blue) are presented. The three individual hyperfine transitions in ^{87}Sr cannot be distinguished, but a feature caused by $F' = 9/2$ and $F' = 11/2$ is pointed out.

The AOM functions in the +1 order and is double-passed [95], shifting the frequency of the pump to be $2\,\Omega_{\rm AOM}$ larger than that of the probe. This means that atoms that are resonant with both the pump and probe are traveling to the right with a velocity corresponding to a Doppler shift of $\Omega_{\rm AOM}$. The resonance condition is then $\nu_0 = \nu_{\rm L} + \Omega_{\rm AOM}$, and a locked laser will be red-detuned from the atomic transition by $\Omega_{\rm AOM}$. Thus, the 461 nm laser is red-detuned by 220 MHz (*after* frequency doubling), and the 689 nm laser is red-detuned by 80.5 MHz.

Fig. 4.16 shows the error signal produced in the FM spectroscopy setup for the 461 nm laser. The largest feature is the ^{88}Sr isotope, which is where we usually lock the laser. ^{86}Sr is visible as a smaller zero-crossing feature to which the laser can also be locked. The ^{87}Sr triplet produces both the highlighted shoulder and narrows the right-side of the ^{88}Sr feature. The signal-to-noise ratio is not fantastic because, as shown in Ref. [200], the ratio of the sideband splitting to the linewidth of the atomic

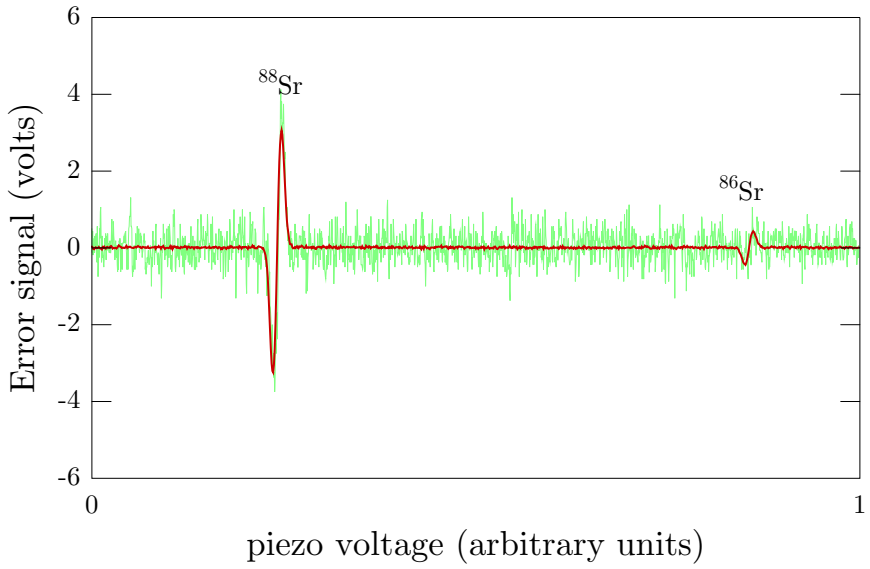

FIGURE 4.17. Error signal produced in FM spectroscoy of the $5s^2\,{}^1S_0 \longrightarrow 5s\,5p\,{}^3P_1$ "red MOT" transition in strontium. Both a single trace (light green) and averaged signal (red) are presented.

transition is important. Because the blue MOT linewidth is so broad, we actually had to increase the EOM drive frequency (which was not trivial, see Sec. 4.2.3.3) to $\Omega_{\text{EOM}} = 8.773$ MHz to improve the error signal. Using a commercial low-noise fast photodetector (New Focus 1801-FS) produces a significantly nicer signal than the homebuilt photodiode used to record Fig. 4.16. The homebuilt photodiode circuit is essentially a buffered transimpedance amplifier, and we can increase the gain at the expense of the frequency bandwidth. A decent signal was attained by using a Hamamatsu S5973 photodiode with a transimpedance gain of 40 V/mA (which is the same as the commercial unit).

We made the same adjustment to the photodiode used in stabilizing the red MOT laser, and the error signal produced in this case is shown in Fig. 4.17. The ability to see two isotopes here allows us to estimate the width of the ^{88}Sr feature. We convert the error signal amplitude into frequency deviation and estimate that the locked signal has rms frequency uncertainty of 250 kHz. This is likely caused by noise

in the detection and demodulation process and by pressure-broadening of the line in the 420°C heat-pipe oven.

4.2.3.3. Helical Resonators

We inherited a free-space EOM (Conoptics 350-50) and borrowed another (Conoptics 350-52) to use as phase modulators, but do we not have the associated high-voltage driving electronics. To generate modulation voltages that are large enough to put significant power into the sidebands, we need to amplify an RF signal. To do this, we have built resonating circuits similar to what ion-trapping groups often use to make their trapping RF fields [201, 202]. These resonators are coaxial devices whose core is wrapped in a helix, and yield high quality factors in a relatively small size. Photographs of the helical resonators we built are presented in Fig. 4.18.

We used the empirical formulae from Ref. [203] to design a resonator that used standard-sized copper pipe and a helix wrapped from AWG 23 magnet wire we had on hand. Unlike Ref. [201], we are not restricted to build a resonator at a particular frequency, which allows for this cost-saving simplification. We used a 5″ length of 2″ ID copper pipe, and a 4″-long coil with 1.1″ ID. The helix was wrapped around a slotted-section of polyvinyl chloride (PVC) pipe, following the build-your-own-inductor method of an amateur radio enthusiast [204]. The helix has 88 turns which are separated by the thickness of the wire, and consistent spacing was achieved by inserting notched, laser-cut ribs into the PVC slots before wrapping the coil. These were epoxied in place to provide rigidity before the coil was removed from the wrapping pipe. The helix was suspended within the copper pipe using nylon screws, and electrical connections are made through 2″-pipe end caps (McMaster 5520K49). Coupling to the resonator can be made through antennae [202] (which also allows

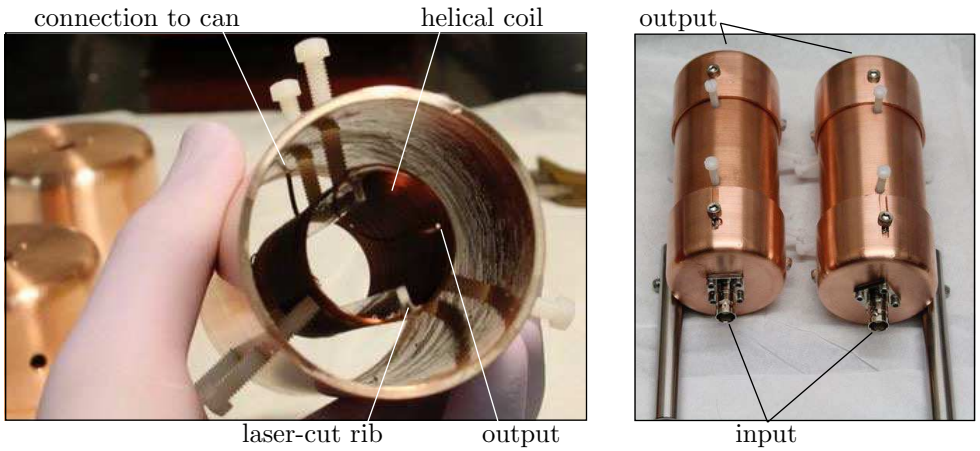

FIGURE 4.18. Photographs of the helical resonating cans used to amplify RF signals for the EOMs. The left picture shows the inner-coil of the coaxial resonator, which is wound by hand with the help of a laser-cut spacing tool. Inputs and outputs are connected via BNC jacks at the bottom and top of the vertically-standing can, respectively.

fine tuning impedance matching), but we simply tapped and grounded the helix at the about the third turn to inductively couple primary and secondary coils which were connected to the input and output, respectively. To realize and maintain a high-Q resonator, we attempted to limit oxidation and therefore maximize the can's conductance (in principle, OFHC copper would work even better than the stock pipe we used, but this would be a custom, costly part). We polished the pipe with Brasso, painted the inside with a thin layer of Q-dope, and sealed the completed resonator with clear nail polish.

Based on the geometry, the resonant frequency of the unloaded amplifier should be about 30 MHz and has a Q of 550, but when loading with a capacitive EOM these should be smaller. Using the Conoptics 350-50 EOM and a directional coupler (Minicircuits ZDC-10-1), we measured $f_1 = 3.2$ MHz and $Q_1 = 180$ for the first resonator and $f_2 = 3.16$ MHz and $Q_2 = 220$ for the second. As mentioned earlier, we realized that we had to increase the resonant frequency of the first can, and we

rewrapped the helix, skipping two notches in our laser-cut ribs (so that the separation between coils was five times the thickness of the wire). With the number of turns in the coil reduced to 30, we measured the altered (loaded) resonator values to be $f_1 = 8.76$ MHz and $Q_1 = 50$. We confirmed that sidebands were produced with the amplified EOM signal by interfering the pump and probe on a photodiode and looking at the RF spectrum centered around $2\,\Omega_{\mathrm{AOM}}$. The amplitude of the RF source is increased until we see second-order sidebands begin to appear.

4.2.4. Slave Laser

To amplify the 689 nm, red-MOT light, we injection-lock a slave diode laser (Hitachi HL6738MG) in a homebuilt housing [95]. We use the rejection port of an optical isolator to seed the slave diode [205], and monitor both the master and slave on an FP cavity to confirm if the slave is locked. The diode's temperature was tuned to bring its free-running wavelength close to the stabilized master's, which enabled locking over a broader range of diode current. Output from the slave is passed through an AOM to provide fine control of the laser's detuning when it interacts with atoms in the MOT.

The master ECDL in this case is the special, long laser we constructed, which we power using the commercial low-noise current supply from Vescent photonics. In the locking circuit, we use low-gain proportional and slow integral feedback to avoid injecting noise into the laser. We have monitored the output of the slave in a delayed self-heterodyne measurement and confirmed that the linewidth is not noticeably increased by the seeding process. While we have not at this point fit the data to characterize the linewidth, the self-heterodyne traces are qualitatively similar to those of the long ECDL (see Fig. 3.11), and we measured the HWHW on

a spectrum analyzer (which as discussed in Appendix C gives the upper bound of the linewidth) to be less than 40 kHz with $T_{\mathrm{obs}} = 1$ ms (the spectrum analyzer has a 1 kHz Gaussian resolution bandwidth).

4.3. Electronics

Most of the electronics used to operate the experiment are homebuilt. Each ECDL and slave laser has its own dedicated current and temperature controller [95, 122, 123], and the TAs use slightly modified versions [179]. Another refashioned version of the laser current driver is used to control current in a magnetic coil [123]. This uses a push-pull arrangement of two OPA549 chips (from Texas Instruments) and features a thermal-protection section that can disable current if a monitored temperature reaches a user-defined threshold. An analog and digital input can set the current target and disable output, respectively, allowing computer control of the magnetic fields used in the experiment. We use these to control current in pairs of coils, wired in series, including the field-canceling Helmholtz (HH) coils and the bottom-MOT AH coils.

We also have homemade analog feedback and control electronics, packaged together in what we refer to as a laser "lockbox." These include a phase-adjustable coupled-oscillator circuit to generate modulation signals at 175 kHz; gain, demodulation, and filtering stages for a photodiode input signal; low-frequency proportional and integral feedback to the tuning piezo (which can also be manually tuned or ramped with an onboard triangle-wave function generator); and optional high-frequency feedback to the laser current with a feed-forward stage. The degree of front-panel adjustability is high, but we have occasionally made a few custom changes to the general design typically used in the lab. In the lockboxes which stabilize the

ECDLs to the heat pipes, we have used a comparator to convert the sinusoidal 175 kHz modulation into the TTL pulse train shown in Fig. 4.15. The lockboxes controlling the SHG cavities, meanwhile, have been modified to modulate at 68 kHz, which is the resonant frequency we measured for the piezo/mirror combination in these setups. The small modulation signal is added to the overall signal applied to the piezo, and we needed to drive on resonance to increase the effects of the modulation and create a nice error signal. Finally, in the lockbox for the 922 nm master ECDL, we have added an input which allows the SHG cavity's automatic relocking circuit [188] to temporarily disable the integral feedback. This prevents the controller from driving the laser frequency too far from resonance while the blue cavity restabilizes.

4.3.1. Radio-Frequency Electronics

To drive our electro- and acousto-optic devices, we have built our own custom PCB wrappers for commercial surface-mount RF components. These are less costly than packaged solutions, and they also allow us to parallelize and organize our RF-electronics chains in a clean and compact manner, as seen in Fig. 4.19(c).

The sequence of electronics we use to drive an AOM is given in Fig. 4.19(a), and the frequencies, powers, and modulators we use are listed in Table 4.3. We begin with a function generator, which uses a voltage-controlled oscillator (VCO) (Minicircuits JTOS-100+, JTOS-200+, or JTOS-300+, depending on the frequency) and a voltage-controlled attenuator (VCA) (Minicircuits RVA-2500+) to produce a customizable RF signal.[2] The frequency and amplitude can be set with manual adjustment knobs or controlled by analog signals controlled by a computer. The

[2]Frequencies of the two AOMs used in the red MOT beam path are set by direct digital synthesizers since this gives us better control of the frequency, important for interacting with the narrow, intercombination linewidth.

Model	Purpose	Ω_{AOM} (MHz)	P_{RF} (W)	η (%)
NeosTech. N15200-0.67-KD	blue lock	220	0.58	20*
Isomet 1250C-829	Zeeman	280	1.45	50
Crys.Tech. 3200S	top MOT	180	0.92	63
Crys.Tech. 3200-121	bottom MOT	180	0.39	47
Isomet 1205C-2	red lock	80.5	0.32	2*
Isomet 1205C-2	red MOT	various	1.25	38
Brimrose TFM-80-30-.800	lattice	80	0.94	80

TABLE 4.3. List of AOMs currently in use in the experiment, including the manufacturer and part number, purpose, operating RF power P_{RF} and frequency Ω_{AOM} (MHz), and efficiency η. The asterisk denotes double-pass efficiency.

RF signal can then be switched (Minicircuits MSWA-2-20) with a digital signal (for example, this is where the TTL pulse in the FM-spectroscopy setup chops the AOM) before it is sent on to a preamplification stage (Minicircuits ERA-3SM) and an RF power amplifier. The power amplifier is an SOT-115J package CATV amplifier in a shielded box (Compac R51160-100-0) with appropriate thermal management. We use two different CATV amplifiers: the MHW1345 component from Freescale has 34.5 dB gain and 10–200 MHz bandwidth, and the CGD1044H from NXP has less gain at 25 dB gain but a wider 40–1000 MHz bandwidth. Like Minicircuits power amplifiers, they are sensitive to RF reflections and can be destroyed if powered on while an input or output is disconnected. Unfortunately, this particular package seems to be obsolete and we have purchased large quantities of each CATV amplifier to have a lifetime supply.

The electronics chain for the EOMs is shown in Fig. 4.19(b). The frequencies we use are $\Omega_{\text{EOM}} = 8.773$ MHz for the blue laser and $\Omega_{\text{EOM}} = 3.161$ MHz for the red, and sources for these are the direct digital synthesizer (DDS) controllers, described below in Sec. 4.3.2. Note that most of the components are not pictured in Fig. 4.19(c). Out of the DDS, the small-amplitude signal is split to a homebuilt phase shifter (φ) and

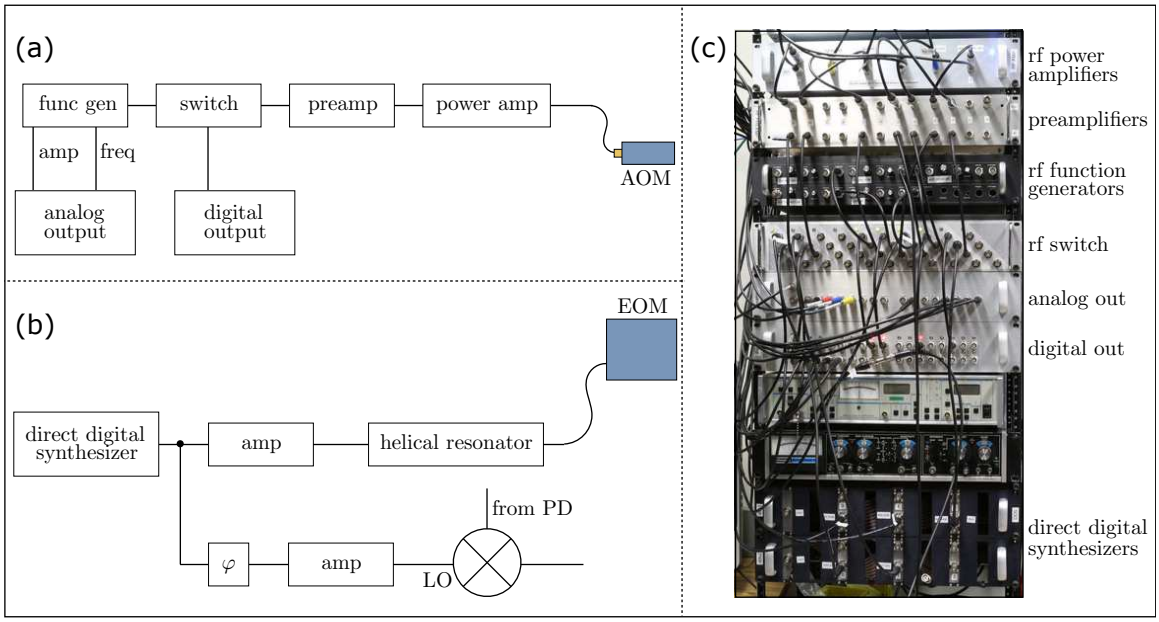

FIGURE 4.19. Overview of electronics used to control RF devices in the experiment. Block diagrams are shown for (a) AOM signals and (b) EOM signals, and a photograph of an electronics rack (c) shows homebuilt packaging of electronics.

amplifier (amp). The phase shifting circuit uses two first-order all-pass filters [206] to shift the phase by more than 180°, but the op-amps rail if too large a signal is used. The amplification stages used in the EOM sequence consist of a pair of cascaded inverting LM7171 op-amps, which have a unity gain bandwidth of 200 MHz and a high slew rate of 4100 V/μs. The amplifiers increase the DDS signal before sending it on to the helical resonator (with an amplitude as large as 20 V peak-to-peak), and also increase the phase-shifted signal used as the local oscillator (LO) in the mixer (Minicircuits ZP-10514+) used to demodulate the photodiode signal.

4.3.2. Computer Control

We interface the experiment with a computer for precise timing of electronic signals. Designs for hardware that produce digital and analog outputs were created by Todd Meyrath when he helped develop a parallel bus control system as a graduate

student in Mark Raizen's group at The University of Texas at Austin [168]. The digital output channels can each drive a 50-Ω load, and we have built two boards for a total of 32 channels. The analog boards use DAC7744 chips by Texas Instruments and produce output voltages between ±10 V with 16-bit accuracy. Each channel here has an output driven by a BUF634 and can drive a maximum of 250 mA. We have built two of these boards, totaling 16 analog channels. Finally, we have six DDS boards, each built around an AD9852 from Analog Devices. Fully digitized signals can be created up to 135 MHz. In principle, arbitrary waveforms can be created, but our software does not currently allow for reprogramming the DDS in time with the rest of the experiment. We can, however, program two frequencies and then switch or ramp between the two via frequency-shift keying (FSK). Timing of the switching is controlled with an external digital signal which *is* well-timed.

Computer control is enabled using software communication with open-source embedded ethernet devices [207]. The project is discussed in detail in Ref. [208]. A computer programs a 'box' via the ethernet-enabled controller, and an interface board loads data into first in, first out (FIFO) memory so they can be read out to the parallel bus hardware. The analog output box is designated to be the 'master,' and one of its channels sends a start pulse to other boxes, marking the beginning of an experimental run. Subsequent synchronization is maintained through the use of a shared clock signal at 10 MHz, derived from a rubidium standard.

CHAPTER V

TRAPPING AND COOLING STRONTIUM

With all the components described in the previous two chapters, we can now discuss our progress in trapping and cooling strontium with our apparatus. The geometry of the cooling setup is pictured in Fig. 5.1. Cooling beams are delivered to the vacuum chamber with free-space optics, and the top and bottom six-beam MOTs are each created via retroreflection of three beams. Top-MOT beams are split from a single beam, which has a waist of 0.55 mm and is detuned to the red of 461 nm resonance by 40 MHz. The transverse beams are expanded with telescopes using 50.2 mm and 500 mm lenses (Newport KPX082AR.14 and KPX211AR.14) to largely fill the 1.5″ clear aperture viewports. These beams are raised to the level of the top MOT with periscopes and directed through the spherical octagon using mirrors on an elevated breadboard, attached to the vacuum chamber's 80-20 support frame. The axial beam for the top MOT is delivered through the bottom of the pyrex cell, and is thus smaller, expanded by a telescope using 100 mm and 300 mm lenses (Newport KPX094AR.14 and KPX112AR.14).

Beams for the bottom MOT—also detuned by 40 MHz—are sized to fill as much of the pyrex cell as possible without clipping. All three retroreflected beams are expanded with 24.5 mm and 100 mm achromat lenses (Newport PAC022AR.14 and PAC052AR.14) from an initial waist of 0.69 mm. As shown in Fig. 5.1, the AH coils are placed on either side of the hanging pyrex cell, and the transverse MOT beams are directed diagonally through the cell. The imaging camera (not pictured) views atoms in the lower MOT from the left side of the illustration.

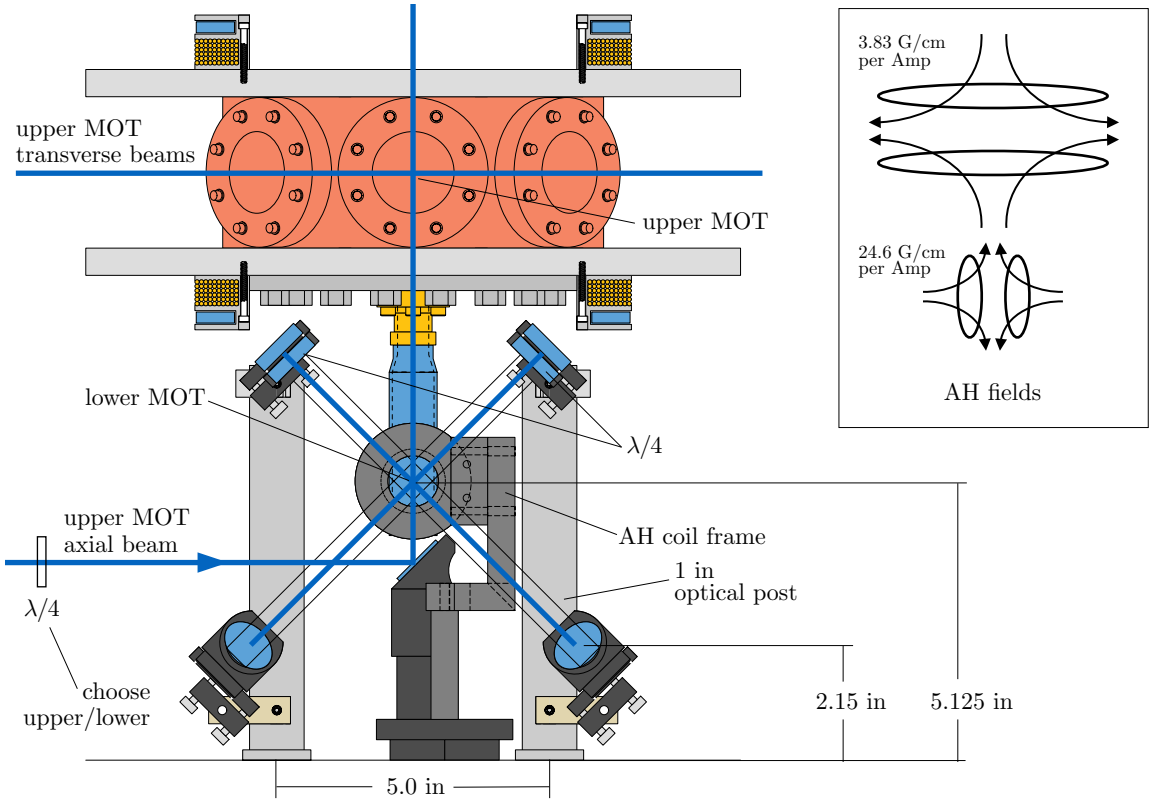

FIGURE 5.1. Schematic of the arrangement of MOT beams for both the top and bottom traps, viewed from the high-pressure side of the vacuum chamber. The transverse top-MOT beams are in the plane of the optical table, and the axial beam is oriented vertically. Beams for the bottom MOT point into the page, with the transverse beams reflected diagonally through the pyrex cell and the axial beam passing through the lower AH coils on either side of the cell. The inset shows the orientation of magnetic quadrupoles, with approximate field gradients for each AH pair.

We use polarizing beamsplitter (PBS) cubes (Photop Technologies BPS0201) and dual-wavelength $\lambda/2$ waveplates (also from Photop Technologies, but with no part number) to divide each of the top- and bottom-MOT beams. We have found that when trying to reflect vertical polarization that is a small fraction of the overall power, there is significant residual horizontal polarization also reflected, and that the beam needs to be cleaned up with an additional polarizer. We use equal power in each MOT's transverse beams, which each have twice the power of the axial beam.

Circular polarization is created using dual $\lambda/4$ waveplates (Photop Technologies, $\lambda/4$ at both 461 nm and 689 nm; $\oslash$38.1 mm for the top-MOT transverse beams, and $\oslash$25.4 mm for the rest).

Repumping light at 497 nm is combined on a dichroic beamsplitter (Semrock LM01-480-25) with the upward, axial top-MOT beam. Thus, it passes through both trapping regions, reducing the power budget. The 689 nm light is combined with the lower-MOT beams before splitting and expansion, also using a dichroic beamsplitter (Semrock FF495-Di03-25x36). The red light's frequency is controlled with a single-passed AOM, so it is steered slightly when we make adjustments to the detuning (a frequency change of 10 MHz deflects the beam by only a couple of millimeters at the MOT). Finally, we have used a dichroic beamsplitter in the beam path for the top MOT in case we want to use red light there as well.

5.1. Double-MOT Scheme

We have successfully cooled atoms in both the top and bottom regions, and photographs of our MOTs are shown in Fig. 5.2. The top MOT is loaded directly from the slowed atomic beam and loads large numbers of atoms quickly (for comparison, we can load a MOT in several tens of milliseconds, but the one-way-barrier experiments in rubidium in our lab used a 20-s loading time). By tuning the piezo of the 922 nm master laser, we are able to trap all four naturally occurring isotopes of strontium, but we lock the laser to the ^{88}Sr resonance and work exclusively with this isotope.

Our first observation of cold atoms occurred when the top-MOT axial beams had incorrect circular polarization. Rather than confining the atoms in the top MOT, the vertical beams were ejecting them (see the middle picture in Fig. 5.2), and we saw a faint fluorescent beam of atoms inside the pyrex cell. This happened because we did

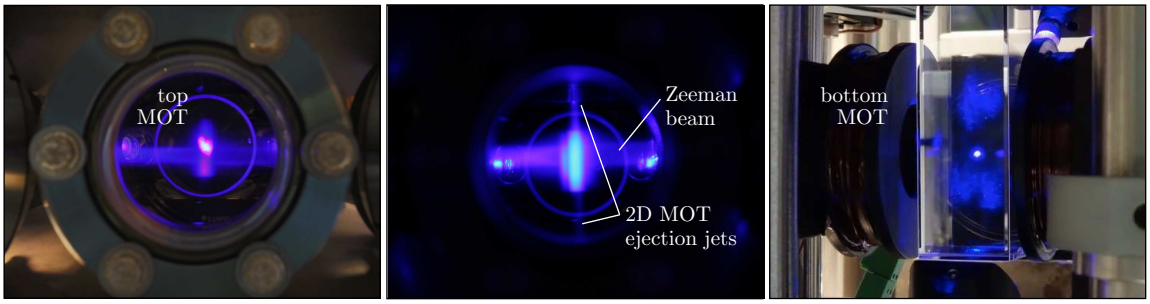

FIGURE 5.2. Pictures of cold strontium atoms: top MOT (left), top MOT in the bottom-MOT-loading configuration (center), and bottom MOT (right). These photos were taken with the atomic source oven operating at 600°C. Photos by Dan Steck, Paul Martin, and Eryn Cook with a Canon EOS 6D, Canon EOS REBEL T5i, and Sony DSC-RX100M3, respectively.

not account for an inversion in handedness from the reflection off the dielectric mirror below the pyrex cell (we have since switched to metallic mirrors for MOT beams after their polarizations are circularized [Newport 10D20ER.1]). Observing this ejected, 2D MOT was serendipitous, however, in that it gave us an efficient method to load the bottom MOT. We had planned on cooling atoms in the spherical octagon, releasing them, and allowing them to fall into the pyrex cell. This would be inefficient because of the high temperature of the blue MOT; a small cloud of atoms at 1 mK would spread to over 3 cm before entering the constricted entrance of the pyrex cell (which is only about ⌀1.5 cm). By ejecting atoms from the 2D MOT, we are able to load more atoms in a continuous fashion.

We are able to switch between loading a top or bottom MOT by rotating a $\lambda/4$ waveplate to change the vertical beam's polarization from confining to ejecting, respectively. Notice from Fig. 5.1 that the bottom trapping region is fairly close to the top MOT's lower AH coil. This means that when the top MOT coils have high currents ($\sim$6.8 A for loading a top MOT) the zero-crossing of the magnetic field in the lower region is shifted downward significantly. We therefore must also decrease the

current in the top AH coils when loading a bottom MOT. Typically, we use a current of around 2 A (roughly 8 G/cm, resulting in a 2D MOT that is much more diffuse than pictured in Fig. 5.2) and use z-axis Helmholtz (HH) coils to shift the magnetic zero to be at the center of the lower AH coil pair. The relative orientation of the top- and lower-AH coils is important because the vertical beam should be polarized to eject atoms from the top MOT but not the bottom.

We find that the repump significantly increases the MOT's brightness and lifetime, as expected from previous observations in strontium [16, 17]. Since we only have a small power available, we keep the beam compact to have maximum impact on the atoms. The brightness of the bottom MOT is fairly sensitive to the alignment of the repumping beam. We carefully overlap it with the vertical MOT beam, then misalign it slightly to maximize the brightness we observe with a security camera (EverFocus EQH5102). The misalignment is likely helpful because the repump is most effective when it overlaps the bottom MOT, which does not necessarily form within the vertical ejection beam. We do not stabilize the 497 nm light to an atomic transition, but rather use the brightness of the atoms to frequently confirm that the light is resonant. In the future if more power is produced at 497 nm (either by getting more power from the master 994 nm ECDL or improving the reflectivity of the mirrors in the SHG cavity), the light could be actively stabilized to the transition using the optogalvanic technique [209, 210].

5.2. Blue MOT Temperature Measurements

To measure the temperature of the atoms in the MOT we can release the trapped cloud, allow it to ballistically expand, and then image it using molasses beams to 'freeze' the atoms in place [211, 212]. This is somewhat simpler than the original

methods used to measure the temperature of optical molasses because MOTs have the additional benefit of spatial confinement.[1] After releasing and allowing the atoms to evolve for t_{delay}, the measured spatial distribution of the cloud will be the convolution of the MOT's initial spatial distribution and a second spatial distribution—created by expansion over t_{delay} due to the initial velocity distribution. Assuming the atoms exhibit a Maxwell–Boltzmann distribution and a Gaussian spatial profile, the resulting expanded cloud will also be Gaussian, with width

$$\sigma_x(t_{\mathrm{delay}}) = \sqrt{\sigma_{x_0}^2 + (\sigma_{p_x} t_{\mathrm{delay}}/m)^2}. \tag{5.1}$$

Here, $\sigma_{p_x} = \sqrt{m k_{\mathrm{B}} T}$ is the width of the atoms' momentum distribution before release. By varying t_{delay}, the hyperbolic form of Eq. (5.1) can be fit to find the temperature of the cloud (for large values of t_{delay}, the initial size of the MOT is negligible and a linear fit suffices).

The duration of the imaging pulse is important because the cloud will still be expanding—albeit diffusively—under the influence of molasses beams. While imaging atoms from a cesium MOT, experimenters in Ref. [211] varied the temporal extent of the freezing molasses. They observed that significant diffusion did not occur for times less than about 20 ms. Since the scattering rate in strontium is roughly a factor of 6 larger than that in cesium, we should use an imaging pulse of only a few milliseconds to avoid artificial broadening of the expanded cloud width.

[1] The "release-and-recapture" method uses the same experimental mechanics as the freezing method we use, but it can have large uncertainties due to sensitivity to molasses spatial distribution [213]. The "time-of-flight" method, on the other hand, is less geometrically sensitive, but requires an extra (resonant) laser—used to probe the absorption of released atoms as they fall and pass through it [2].

5.2.1. Imaging System

We take fluorescence images using a charge-coupled device (CCD) camera ("MicroLine" camera from Finger Lakes Instrumentation—we call it the "FLI camera") which was used in previous experiments and is also described Ref. [123]. We use a Micro-Nikkor 55 mm $f/3.5$ lens from Nikon at its closest focus and block background light (especially 689 nm and 914 nm light which could scatter into the camera) using a color filter (Schott BG40, part number FGB37 from Thorlabs). The colored glass is not AR-coated and transmits roughly 89% of 461 nm light, meaning the quantum efficiency of our camera (which has a Kodak KAF-0402ME sensor) is about 45%. We used a scaled target reticle (Edmund NT39-460) and measured a size conversion factor for our images to be ~ 23.75 μm/pixel.

The shuttering system in our CCD camera is problematic in a number of ways. In the past the shutter blades would often stick or break, requiring frequent cleaning and repair. A small change to the actuating mechanism [123] seems to have helped (we have only had to replace one shutter blade, and have not noticed significant sticking since). Additionally, in its original use, the mechanical vibrations produced by the camera could cause the "bronze" lasers in the rubidium experiments to come unlocked. Previous graduate students resolved this issue by mounting the camera on a large, heavy damping plate that was connected to a second base with a strip of $0.125''$-thick Sorbothane sandwiched in between. On our optical table, however, the SHG cavities are quite sensitive to vibrations and the damping solution unfortunately was not as effective. We learned through an informal conversation with Luis Orozco—who has used Sorbothane to reduce vibrations in cavity QED systems [128]—that Sorbothane is much more effective at damping vibrations when it is cut into smaller pieces. The reduced size allows for more transverse expansion of the viscoelastic material,

which is the mechanism for extracting vibrational energy. The ratio of the loaded to unloaded surface area (called the "shape factor" in Sorbothane's Engineering Design Guide [214]) should be between 0.3 and 1 for good damping, and the strip we were using had a ratio over 10. We cut up small 0.25″ square pieces (shape factor of 0.5), and the improvement was dramatic: before, the disturbance of taking a picture was so severe that the SHG cavities would often come unlocked, but now the response of the error signal is greatly reduced.

Temperature measurements of the blue MOT are difficult given our camera shutter's finite opening time. By varying the timing of an exposure pulse in relation to the camera trigger pulse, we determined the timing of the shutter response. The observed intensity as a function of time was roughly an error function, as suggested by the camera profile in Fig. 5.3. The camera shutter begins to open 10 ms after the triggering pulse and is fully open about 20 ms after the trigger. This means that we cannot image the expanded cloud for $t_{\mathrm{delay}} < 10$ ms without also partly imaging the MOT before it is released. Unfortunately, since ^{88}Sr does not experience sub-Doppler cooling effects, the temperature of the blue MOT is quite hot ($T_{\mathrm{doppler}} = 770\ \mu$K), and 10 ms is too long to wait and still have an appreciable signal. (The cesium atoms in Ref. [211], for comparison, were on the order of 10 μK and were measured with expansion times of 15 ms $\leq t_{\mathrm{delay}} \leq$ 40 ms.)

5.2.2. Expansion Data and Temperature Estimate

Despite the issues of the slow shutter, we attempted to make a temperature measurement by including the partial image of the loaded MOT in our background signal. The experimental timing sequence used in this measurement is shown in Fig. 5.3, with timing referenced to the release of the trapped atoms. AH fields and

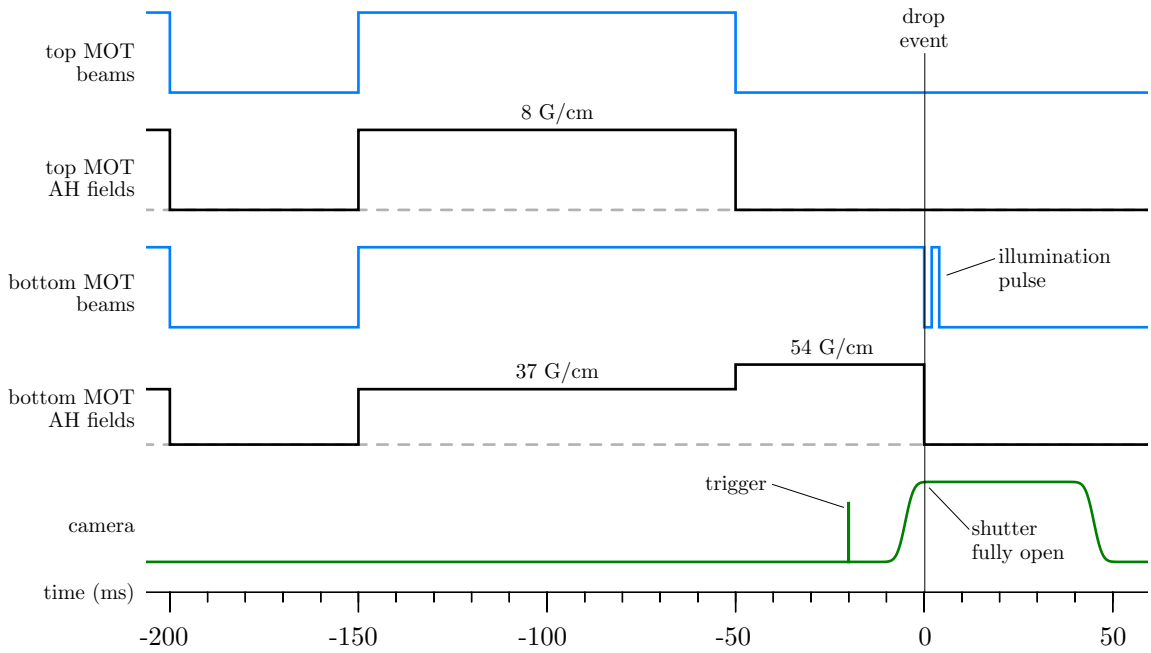

FIGURE 5.3. Control timing sequence used to trap and image the bottom MOT during temperature measurements. The delay between triggering the CCD camera and the aperture fully opening is roughly 20 ms. The time between the drop event and the illumination pulse t_{delay} is varied between 0.25 ms and 2.00 ms in Fig. 5.6.

MOT beams were initially turned off to dump atoms before loading a bottom MOT for 100 ms. After this, we turned off the top-MOT cooling beams and magnetic fields and adjusted the lower HH fields while increasing the AH field gradient to 54 G/cm to tighten the trap. These changes spatially shift the MOT, and we waited for 50 ms to let magnetic field transients decay. Finally, we released the bottom MOT by inhibiting the AH fields while switching off the cooling beams with an AOM. The camera is triggered so that its shutter is fully open at the time the atoms are released. A 2-ms-long illumination pulse images the atoms after t_{delay}, which we vary between 0.25 ms and 2.00 ms. A "background" sequence is identical, but does not have an illumination pulse.

We had hoped that subtraction of the image of the loaded MOT would provide distributions that could be fit with Gaussians to extract the temperature.

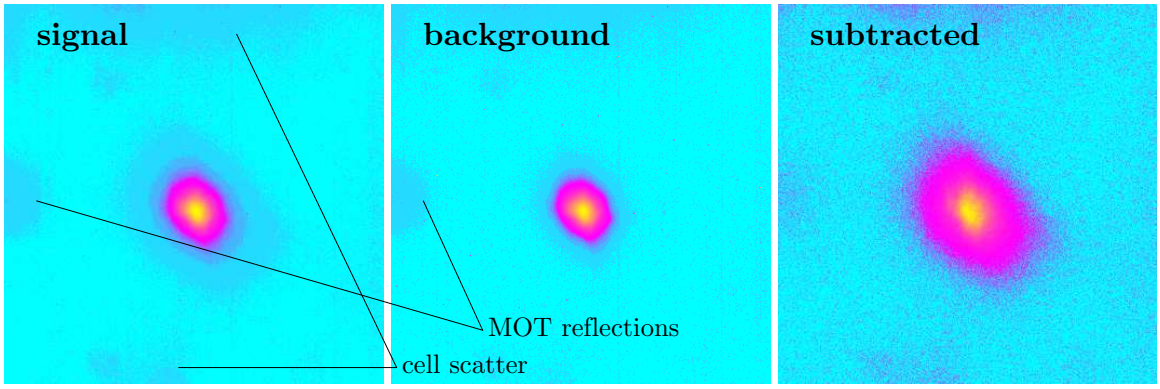

FIGURE 5.4. CCD images for a drop delay of 50 ms using 100 repetitions of the timing sequence in Fig. 5.3. Some sources of light pollution are identified and can be seen to persist in the subtracted image.

Unfortunately, variations in MOT brightness make this difficult. These variations have several underlying causes, including fluctuations in the number of atoms loaded in the MOT (from unstable power of the repumping beam), slight changes in the timing of the opening of the camera shutter (exposing the MOT for an uncontrolled amount of time), and changes in the intensity of the MOT beams. Even with the improved Sorbothane damping, the blue laser can have small changes to its intensity as the shutter opens, and the output power of the SHG cavity can also have long-term drifts. We attempted to remedy these fluctuations by using a pulse-stabilizer circuit [215] that was built for absorption imaging in the previous rubidium experiments in our lab [123]. This circuit compares an analog voltage to the integrated power it receives from a picked-off portion of the bottom-MOT beams. When the two are equal, a digital output is sent to the RF switch controlling the beam's AOM. We set the analog voltage to correspond to a roughly 2 ms pulse length, but the pulse-stabilizer circuit ultimately controls the timing, ensuring that a consistent illumination energy is used from run to run.

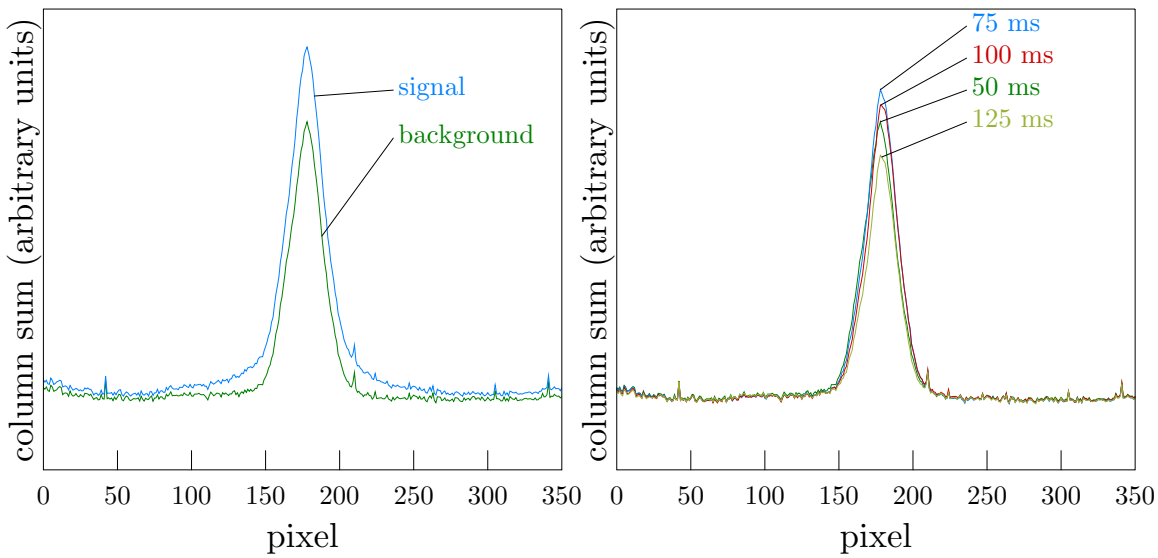

FIGURE 5.5. Sum of pixel values along columns of the signal and background images in Fig. 5.4 are shown on the left. The signal has a broader tail than the background due to expansion of the atomic cloud during the delay time. Similar sums of the background images are shown on the right for several delay times. The peak of the background images varies, showing the volatility in the brightness of the MOT during these measurements.

An example of the image subtraction process is shown in Figs. 5.4 and 5.5 for $t_{\text{delay}} = 50$ ms. We alternate between "signal" and "background" sequences and average together 100 images of each before subtracting. Pixel values can be integrated along the rows or columns of an image to produce a distribution from which the width can be extracted. It is clear from the signal's broad tails in the left plot in Fig. 5.5 that a larger Gaussian shape is hidden by the bright MOT. Ideally, the central MOT image can be removed perfectly, but the variation in MOT brightness (even with 100 images averaged) is problematic. This is illustrated in the right plot in Fig. 5.5, where averaged background images have been integrated for several delay times (the delay time serves simply as a label, of course, since the background images have no illumination pulse). Since the variation of the peak amplitude of the background

MOT is on the same order as the amplitude of the expanded cloud's distribution (in the left plot), this clearly is problematic.

Subtracted images for a sequence of expansion times are pictured in Fig. 5.6 and the integrated distributions are shown in Fig. 5.7. CCD images have been individually normalized before applying a color scaling, so the size in the subtracted image is not necessarily representative of the width of the expanding cloud. The problems of fluctuations in MOT brightness is clear in these images: the amplitude of the integrated distribution at $t_{\mathrm{delay}} = 0.25$ ms is much smaller than at 0.50 ms or 0.75 ms. It is also apparent that the atoms expand rapidly, and images after about 1.50 ms are not useful. Moreover, the contributions of extra scatter on the pyrex cell are significant with the small subtracted signals, complicating the prospect of fitting data. Ultimately, however, we will be performing temperature measurements on much colder atoms in a red MOT, and these complications will be avoided.

To make a very rough estimate of the temperature, we can use the size of the unexpanded MOT and estimates of the restoring force. From the equipartition theorem, the size of the MOT in one dimension is related to the temperature via $k_{\mathrm{B}}T = \kappa z_{\mathrm{rms}}^2$, where κ is defined in Eq. (A.8) [147]. The FWHM of the MOT is typically between 22 and 25 pixels, and the axial bottom-MOT beam (which confines the atoms roughly in the horizontal direction as viewed by the camera) has a power of ~ 2 mW over approximately a square centimeter. This corresponds to a temperature range of 3–4 mK, which is reasonable, given blue MOT temperatures measured by other groups using ^{88}Sr [16, 17].

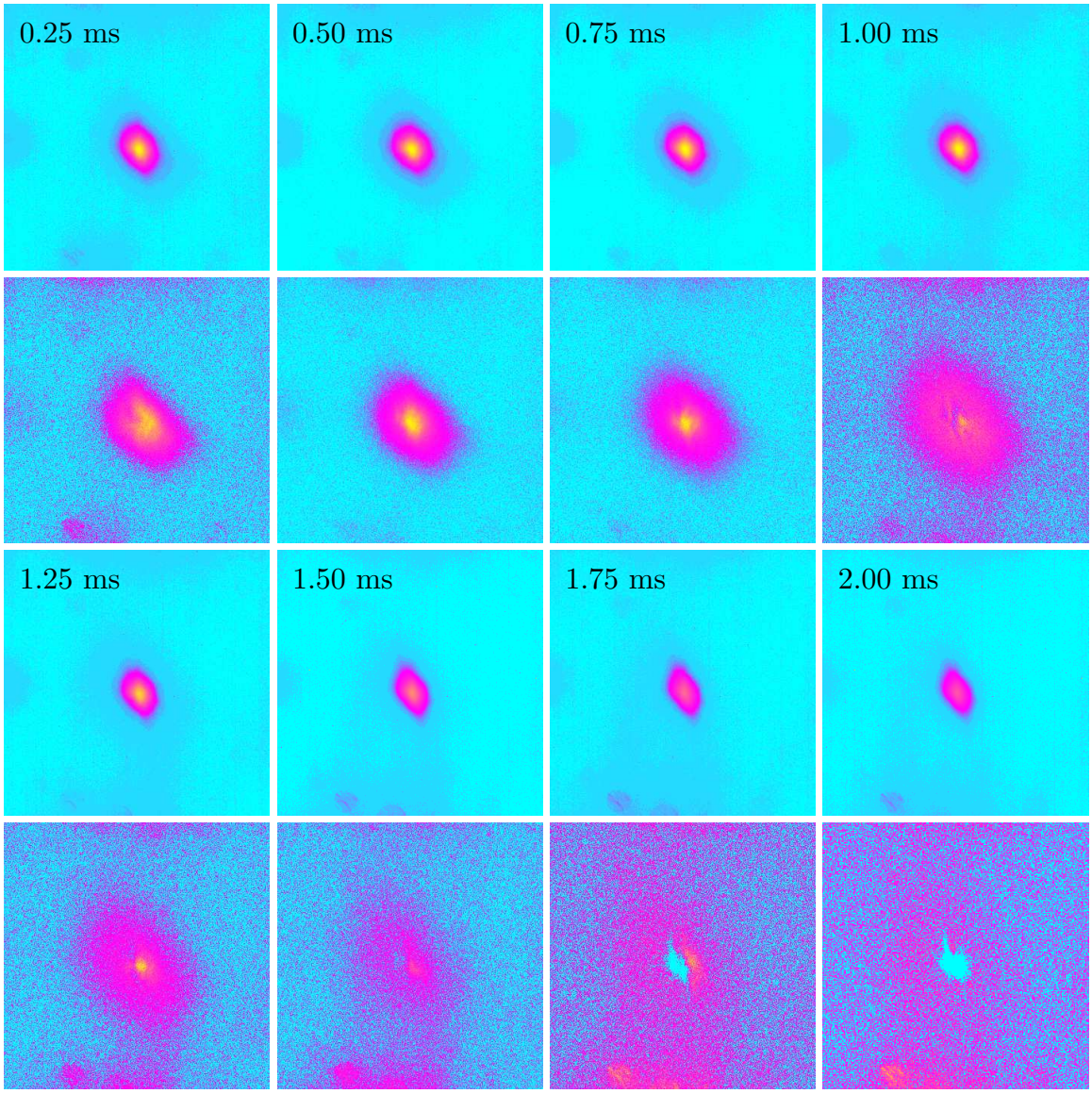

FIGURE 5.6. Series of images taken in an attempted temperature measurement of the blue MOT. For each delay time, the signal image (average of 100 runs) is shown above the subtracted result. Each image is normalized to itself, so false color levels are not necessarily comparable.

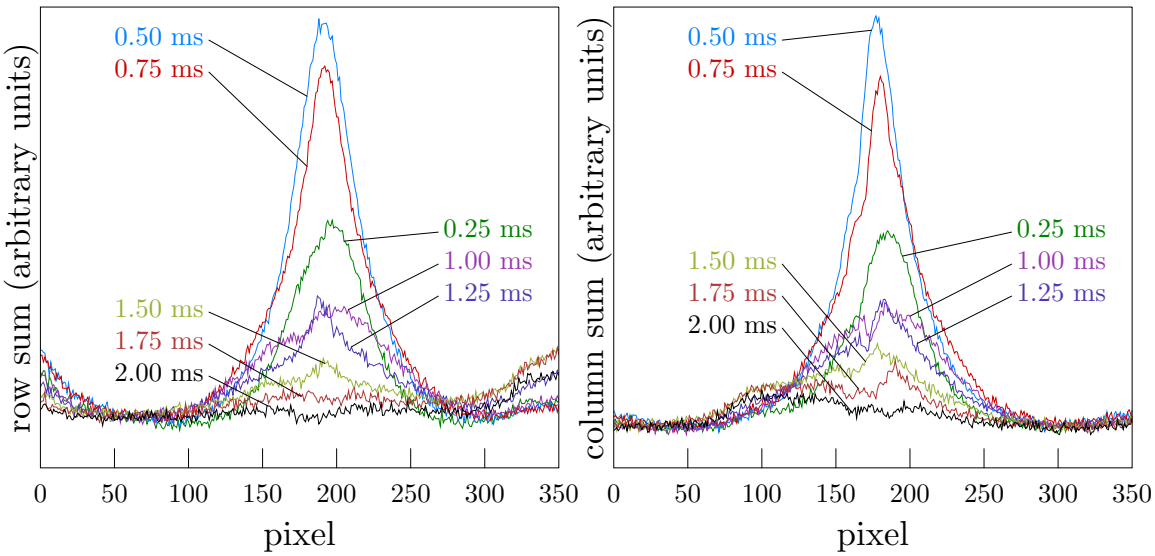

FIGURE 5.7. Integrated pixel values of the series of subtracted images shown in Fig. 5.6. Pixel values are independently totaled horizontally (left) and vertically (right). Contributions of scatter in the cell can be seen as increases in the summed value at small and large row number and as a feature near column 100.

5.3. Cooling in a Red MOT

Narrow-band cooling is interesting because it can be a regime where single photon scattering events are important in MOT dynamics. Usually atomic cooling is performed on a broad, cycling transition where $\Gamma \gg \omega_{\text{recoil}}$. In this limit, individual recoil events do not significantly change the effective detuning δ_{eff}, and a semiclassical treatment of the field involving scattering rates suffices. Here atoms in molasses beams can be considered to be in Brownian motion, leading to the concept of the Doppler-cooling temperature limit [147]. The recoil frequency shift of the 7.6-kHz-wide intercombination line in ^{88}Sr, however, is 4.7 kHz ($\Gamma/\omega_{\text{recoil}} = 1.6$), and a quantized model of the field is needed to develop a Doppler-cooling theory [216]. In this regime, atomic temperatures are much smaller than the traditional Doppler limit, even reaching values *below* the single-photon recoil level [27].

If a transition is too narrow, however, then a traditional MOT operating on the line is infeasible. Calcium, for instance, has a 408-Hz-wide $^1S_0 \longrightarrow ^3 P_1$ transition at 657 nm. This linewidth is so narrow that the maximum scattering force is not much larger than gravity ($\hbar k\Gamma/2mg = 1.5$), and atoms literally fall out of the MOT. (Despite this issue, cold ^{40}Ca samples have been created by quenching the excited state to artificially decrease the lifetime [217] and by using an alternate narrow-band transition connected to the long-lived $^3P_2$ state [218].) Strontium is convenient because the intercombination line is narrow, yet broad enough that the radiation pressure can overcome the gravitational force ($\hbar k\Gamma/2mg = 16$). Images of a red MOT show the atoms sagging to the bottom of the trapping region, where the position-dependent force is maximum [27].

The narrow transition is also quite sensitive to power broadening because the saturation intensity is so small (3 μW). This means the effective linewidth $\Gamma_{\text{eff}} = \Gamma\sqrt{1 + I/I_{\text{sat}}}$ can be increased significantly, entering the broadband cooling regime once more. Cooling-beam intensity and detuning thus have a profound impact on final temperatures reached in the red MOT, and this has been explored in depth by the Ye Group [19, 27, 89, 219]. We plan to use intensities for our 689 nm laser that are large enough to capture many atoms at several μK.

5.3.1. Transfer Process

Cooling in a red MOT is complicated by the narrow transition because atoms will only be resonant in a small velocity window. At 1 mK, for instance, the average atomic speed is 0.5 m/s, but a velocity change of only 0.005 m/s gives a Doppler shift equal to the transition's linewidh—meaning that most atoms are out of resonance with the laser. In order to combat this effect, the red molasses beams can be frequency-

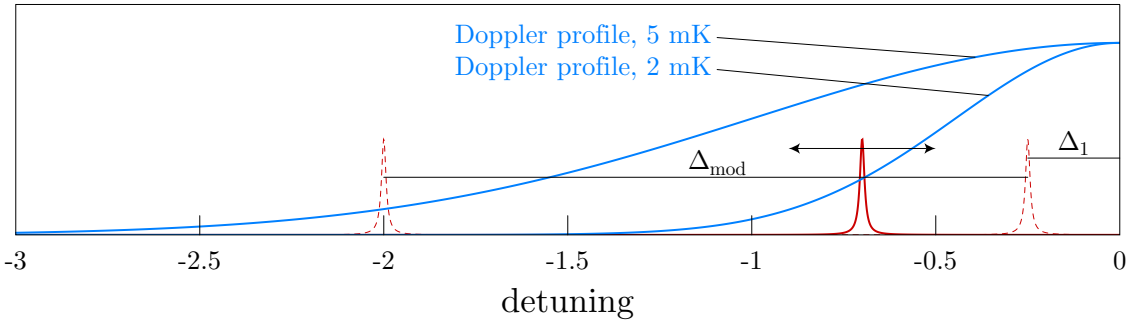

FIGURE 5.8. Modulating the detuning of the red MOT beams to interact with atoms at blue MOT temperatures. Doppler-broadened distributions of atoms are shown for temperatures of 2 and 5 mK. The narrow laser—pictured here with a 7.5 kHz linewidth—will only interact with a small number of atoms, so to cool the entire population it is artificially broadened by ramping the detuning between Δ_1 and $\Delta_1 + \Delta_{\text{mod}}$.

chirped [220] or artificially broadened [15] to address and cool more atoms. This idea is illustrated in Fig. 5.8, where a narrow cooling laser is shown alongside the frequency spread of Doppler-broadened distributions of atoms at 2 and 5 mK. By ramping the laser's detuning between $\Delta_1 + \Delta_{\text{mod}}$ and Δ_1, the narrow lineshape sweeps across a significant fraction of the thermal atoms, increasing the transfer efficiency from blue MOT to red.

Additionally, for a given magnetic field gradient, the boundaries of the blue and red trapping regions are also quite different. Using Eq. (4.7) again as intuition, we can estimate the expected size discrepancy. The detuning of the blue MOT is $\Delta_{\text{blue}} = 40$ MHz, and the largest detuning in Fig. 5.8 is $\Delta_{\text{red}} = \Delta_1 + \Delta_{\text{mod}} = 2$ MHz (note that the boundary of the red MOT is ramped along with the frequency). The effective magnetic moments for the two transitions, meanwhile, are $\tilde{\mu}_{\text{blue}} = \mu_{\text{B}}$ and $\tilde{\mu}_{\text{red}} = 3\mu_{\text{B}}/2$. Thus, at its largest extent the red MOT will be a factor of 30 smaller in the same magnetic field. This again means that many of the atoms will be lost unless we also significantly decrease the magnetic field gradient to encompass the atoms within the red MOT's trapping region.

As a starting point, we have followed the procedure of the Katori and Ye Groups [15, 27], where transfer efficiency from the blue to red MOTs can be as high as 50% [19]. After loading atoms in a lower blue MOT (by following the sequence of events for $t < 0$ in Fig. 5.3, we simultaneously turn off the blue light, lower the magnetic field gradient from 54 G/cm to 3 G/cm, and turn on modulated red light. After the atoms are cooled for roughly 10 ms, we ramp the magnetic field gradient up to 10 G/cm over 50 ms. This serves to compress the red MOT, which can then be cooled further with the unmodulated red laser operating at detuning Δ_1. We achieve modulation of the red light through the ramped FSK ability of the DDS boxes. In the computer we can set the final detuning Δ_1 , the modulation depth Δ_{mod}, and the frequency at which the laser sweeps back and forth between the two extremes. The computer controls a digital signal which ramps the DDS frequency up and down linearly.

5.3.2. Current Progress

At the end of the described sequence, we turn off the AH field and pulse on the blue imaging light to observe the atoms. Unfortunately, we do not see any evidence that we have successfully loaded a red MOT, and are still debugging the process. We have observed that shining the modulated red laser into a blue MOT reduces the brightness of the atoms, which can be seen in both our security camera monitor and in the FLI CCD images (this is true even if the light is blue detuned). This presumably happens because the laser is driving population to the $^3\mathrm{P}_1$ state, reducing the number of atoms that can fluoresce at 461 nm. The red light is therefore successfully locked to the 689 nm transition.

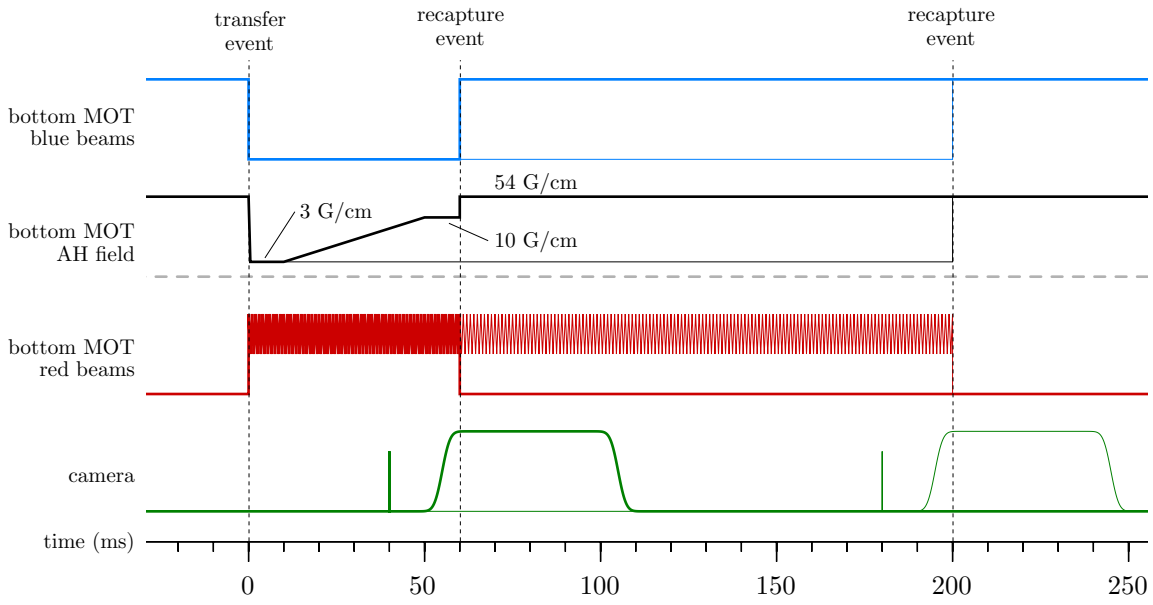

FIGURE 5.9. Control timing sequence used to test if the red laser is affecting the atoms. Atoms are released from the blue trap at $t = 0$ and allowed to interact with modulated red light for some time before the blue trap is reengaged. Two testing scenarios are shown: recapture event (a) occurs after ramping the AH field from 3 G/cm to 10 G/cm (thick lines), and recapture event (b) occurs after leaving the AH field low for long timescales (thin lines).

Additionally, we have tried to recapture remaining atoms in a blue MOT after interaction with the red light. Two timing sequences are shown in Fig. 5.9: the first (a) goes through the cooling sequence described above (save for ceasing modulation in the final cooling stage) before recapture, while the second (b) leaves the field at a low value, allowing the modulated red light to interact with the atoms for some time before recapture. We have found that we can recapture some of the atoms in each case, evidence that the red light is inhibiting some atoms from leaving the trapping region. We find that we can recapture a larger fraction of the atoms for smaller values of Δ_1 (on the order of 100 kHz) and moderate modulation depths of $\Delta_{\mathrm{mod}} \sim 1$ MHz. (The signal is greatly reduced both when the modulation is disabled and when $\Delta_{\mathrm{mod}} > 2$ MHz. We have typically ramped the frequency between the

extreme values at a rate of 25 kHz, and we might need to increase this rate if we want to modulate over a broader range of frequencies.) For parameters which yield large recapture fractions, we find that the scenario in (b) can load atoms more than 500 ms after the release event.

We currently overlap the lower blue and red MOT beams on a dichroic *before* using polarization optics to split the beams into three paths. This assumes that the dual waveplates are actually $\lambda/4$ for both wavelengths, like we specified in our order from Casix. The Ye Group, however has waveplates which are $\lambda/4$ for 461 nm and $3\lambda/4$ for 689 nm, calling into question the retardance of our waveplates.[2] We have tested the waveplates by alternating the polarity of magnetic fields during the red-laser-interaction times of the timing sequences in Fig. 5.9. We have found that atoms are recaptured for each polarity, but that consistently more are recaptured when the sign of the magnetic field matches what we use in the blue MOT. Thus, we think our waveplates are indeed $\lambda/4$ for each wavelength.

So, given that the laser is resonant with the atoms and that we are using the correct field gradient polarity, why are we unable to load the red MOT? It's possible that background magnetic fields are not nulled well enough, and the zero-crossing of the AH field is displaced significantly far from where the blue MOT forms. Atoms in a red MOT that are shifted away from the focal plane of the FLI camera would then be harder to see unless 'recaptured' by again turning on the high field gradient of the blue MOT. Another possible issue is related to the geometry of our setup. The orientation of the axis of the AH coils in Ref. [27] is perpendicular to the optical table, and the vertical trapping beam directly opposes gravity. Our vertically-oriented beams,

[2]Investigating further, we found that the material shipped with the waveplates indicated that they were indeed $\lambda/4$ at each wavelength, but the vendor—after we recently asked directly—said they were $3\lambda/4$ at 689 nm.

however, are diagonally positioned (as shown in Fig. 5.1), so the radiative force is reduced by $\sqrt{2}$ (having two beams does not double the upward force since they are well above saturation intensity). This means the maximum scattering force is now only 11.3 times the force of gravity, and it's possible that atoms are not well spatially confined. For either of these, a potential debugging tool is to attempt to load the red MOT in the spherical octagon, where we have both better control over the magnetic fields (the HH coils here are closer to optimal spacing) and a trapping beam directly opposing gravity. Alternatively, we could add an additional red MOT beam, oriented vertically to test the latter possibility in the lower trapping region.

CHAPTER VI

CONCLUSION

This dissertation has detailed the development of a strontium MOT for future use in measurements of atom–surface interactions. Strontium is a promising candidate for such measurements because, as an alkaline earth element, it offers spectroscopically narrow spin-flip transitions which have helped enable unprecedented timekeeping in strontium optical lattice clocks. These narrow transitions provide ample resolution to make direct measurements of CP-induced level shifts when atoms are near a surface.

A secondary benefit of using strontium is the ability to confine atoms in a magic wavelength optical lattice that eliminates light-shift systematics while providing good spatial resolution of atom–surface separation. We propose using test surfaces which are partially transparent at the magic wavelength so that one of the lattice beams comes from behind the surface. In this configuration the locations of the lattice minima are not fixed by the boundary of the surface, like they would be in a reflected lattice scheme. Strontium atoms could therefore be loaded far away from the test surface and controllably translated into position for measurement of the CP shift. In such a lattice scheme, atoms could be brought as close as 200 nm before the trapping potential is overwhelmed by the CP effect, and this technique would join Ref. [84] as a rare experimental investigation into intermediate-range CP potentials.

The experimental apparatus needed for such measurements requires extensive development and construction. Our lab embraces a cost-effective, do-it-yourself approach, and during this nascent project we have produced several complex laser systems, numerous control electronics, and a UHV system with a hot-strontium source. We have been fortunate to be able to share some of our achievements

in a pedagogical and open-source fashion [116, 126, 173], and our passively stable ECDL design has been adopted by many groups in the atomic physics community (in addition to some labs pursuing their own machining solutions, the University of Oregon Technical Science Administration machine shop has shipped more than fifteen sets of components to groups from around the world). With our stabilized 461 nm laser, we can slow strontium atoms from an atomic beam, load them into a primary MOT, and transfer them to a secondary MOT that is more isolated from background gas collisions and offers better optical access.

Atoms in this blue MOT are still quite warm, however, and further narrow-line cooling on the 689 nm intercombination line is necessary before they can be efficiently loaded into an optical lattice. We have been able to confirm recently that our stabilized 689 nm laser is resonant with the atoms: We can release the blue MOT, switch on a red molasses, and recapture many of the atoms a few hundred milliseconds later. Unfortunately, we have not observed evidence that we are successfully loading a red MOT, and addressing this issue is the next step in the continued maturation of the apparatus.

Once methods for loading a red MOT have been developed, proof-of-principle experiments can begin to be pursued. For simplicity, these will probe the relatively broad intercombination line and use the side of the hanging pyrex cell as a test surface. Short-term work that needs to be done includes integration of the air-bearing translation stage, alignment of the optical lattice, and possibly some narrowing of the 689 nm interrogation laser by stabilizing it to a high-finesse optical cavity. Impact of these initial measurements will be significant because relatively few schemes exist for measuring vacuum-induced potentials, and additional experimental avenues are valuable.

Moreover, the apparatus can be improved after initial measurements to enable more ambitious CP investigations. First, much finer resolution can be obtained by probing an ultranarrow clock transition instead of the intercombination line. This will involve building a pair of new lasers—one to serve as the optical lattice at the new transition's magic wavelength, and one that is extremely narrow to probe the CP shifts. Additionally, investigations of test surface geometry and composition can be pursued since the lattice technique only requires some transparency at the magic wavelength. In contrast to alkali atoms, ^{88}Sr presents high flexibility in surface choice because it has no nuclear spin and has a higher ionization energy (for metallic surfaces these characteristics reduce trap losses and ionic character of adsorbed atoms, respectively).

A better understanding of CP potentials could impact engineering of small-scale cold-atom sensors and quantum information processing devices. We believe that cold strontium can be a useful resource for probing atom–surface interactions in novel regimes, and the apparatus we have developed is an important first step in realizing such an investigative tool.

APPENDIX A

TRAPPING BASICS: MECHANICAL FORCES OF LIGHT

Light can influence the motion of an atom through radiation pressure. Consider an isolated atom that is illuminated by a monochromatic plane wave, nearly resonant with the atom. Both absorption and emission of a photon changes an atom's momentum by $\hbar k$, where k is the magnitude of the wavevector, $k = 2\pi/\lambda = |\mathbf{k}|$. The direction of the momentum change is fixed for absorption but random for emission. A single absorption–emission scattering event is therefore not very meaningful, but after many such interactions, the momenta from emitted photons have no net effect. Thus, the light source can "push" an atom in the same direction as $\mathbf{k}$.

In a semiclassical treatment, we consider a two-level atom to be at rest while interacting with a classical plane-wave light source via the dipole potential [39, 147]. The mean radiation force is a quantum of momentum times the rate of scattering events,

$$\langle \mathbf{F}_{\mathrm{rad}} \rangle = \hbar \mathbf{k}\, R_{\mathrm{scatt}} = \hbar \mathbf{k}\, \Gamma \rho_{ee}. \tag{A.1}$$

The scattering rate is expressed in terms of ρ_{ee}, the excited state population, and Γ, the rate of decay from $|e\rangle$ to $|g\rangle$ (also called the linewidth). The excited state population is found by solving the optical Bloch equations under the rotating wave approximation (RWA) [39], and the radiation pressure force becomes

$$\langle \mathbf{F}_{\mathrm{rad}} \rangle = \frac{\hbar \mathbf{k} \Gamma}{2} \frac{s_0}{1 + s_0 + (2\Delta/\Gamma)^2}. \tag{A.2}$$

Here, s_0 is the on-resonant saturation parameter, $s_0 = I/I_{\rm sat} = 2|\Omega|^2/\Gamma^2$, where $I_{\rm sat}$ is the saturation intensity and the Rabi frequency Ω is the rate at which resonant light causes the atom's population to oscillate between the ground and excited state. The detuning is the mismatch of the laser's frequency with the atomic resonance, $\Delta = \omega_{\rm L} - \omega_0$, and light is said to be "red detuned" for $\Delta < 0$ and "blue detuned" for $\Delta > 0$. As we might expect, the force is a Lorentzian function of $\omega_{\rm L}$, and the maximum amplitude of $F_{\rm max} = \hbar k\Gamma/2$ for high intensity resonant light (for large intensities, the atom is equally likely to be in the ground and excited states and $\rho_{ee} = 1/2$).

In general, however, a laser of frequency ω_0 will not produce the maximal scattering force because the atom's resonance can be shifted away from ω_0. It is better to consider an *effective* detuning in Eq. (A.2),

$$\begin{aligned}\Delta_{\rm eff} &= (\omega_{\rm L} + \Delta_{\rm Doppler}) - (\omega_0 + \Delta_{\rm Zeeman}) \\ &= \Delta + \Delta_{\rm Doppler} - \Delta_{\rm Zeeman},\end{aligned} \tag{A.3}$$

which includes a shift of the laser frequency due to the velocity-dependent Doppler effect, $\Delta_{\rm Doppler} = -\mathbf{k}\cdot\mathbf{v}$, and a shift of the atomic resonance by the magnetically-induced Zeeman effect, $\Delta_{\rm Zeeman} = \tilde{\boldsymbol{\mu}}\cdot\mathbf{B}/\hbar$ (where $\tilde{\boldsymbol{\mu}}$ is the difference in the atom's excited- and ground-state magnetic moments). For simplicity, we will restrict our discussion to one dimension and examine the influence of the detuning modifications individually.

A.1. Optical Molasses

The Doppler shift in 1D has a magnitude of kv, with the sign being determined by the relative directions of the laser and atom. If the laser opposes atomic motion, the frequency is shifted to the blue, $\omega_{\rm L}+kv$. Thus, a laser that is red-detuned is more likely to scatter photons for atoms traveling toward it, extracting energy in a dissipative process. This is the basic idea of an "optical molasses," in which counter-propagating, red-detuned lasers damp atomic motion and reduce their kinetic temperature [213]. In our 1D picture, consider two beams, one with $k > 0$ and the other with $k < 0$. Their combined force on an atom of velocity v is

$$F_{\rm molasses} = \frac{\hbar k \Gamma}{2} \left(\frac{s_0}{1 + s_0 + [2(\Delta - kv)/\Gamma]^2} - \frac{s_0}{1 + s_0 + [2(\Delta + kv)/\Gamma]^2} \right). \qquad \text{(A.4)}$$

This force is shown for low illumination intensity ($s_0 \ll 1$) in Fig. A.1, where the x-axis is the atom's velocity. Atoms which move to the right (left) with a positive (negative) velocity are shifted into resonance with the left-going (right-going) beam, and are correspondingly slowed. The detuning of the lasers moves two Lorentzians away from the origin, and for $\Delta = -\Gamma/2$, the momentum transfer is uniform over a maximum range of velocities. In practice, however, there is some power broadening of the transition because s_0 is not negligible, and it is reasonable to use a larger detuning. The figure shows lineshapes using $\Delta = 1.25\,\Gamma$, which is what we use for our blue strontium trap, described in Chapter V.

In the limit of $kv \ll \Gamma$, Eq. (A.4) reduces to

$$F_{\rm molasses} = 4\hbar k^2 s_0 \, \frac{2\Delta/\Gamma}{\left[1 + s_0 + (2\Delta/\Gamma)^2\right]^2} \, v =: -\beta v. \qquad \text{(A.5)}$$

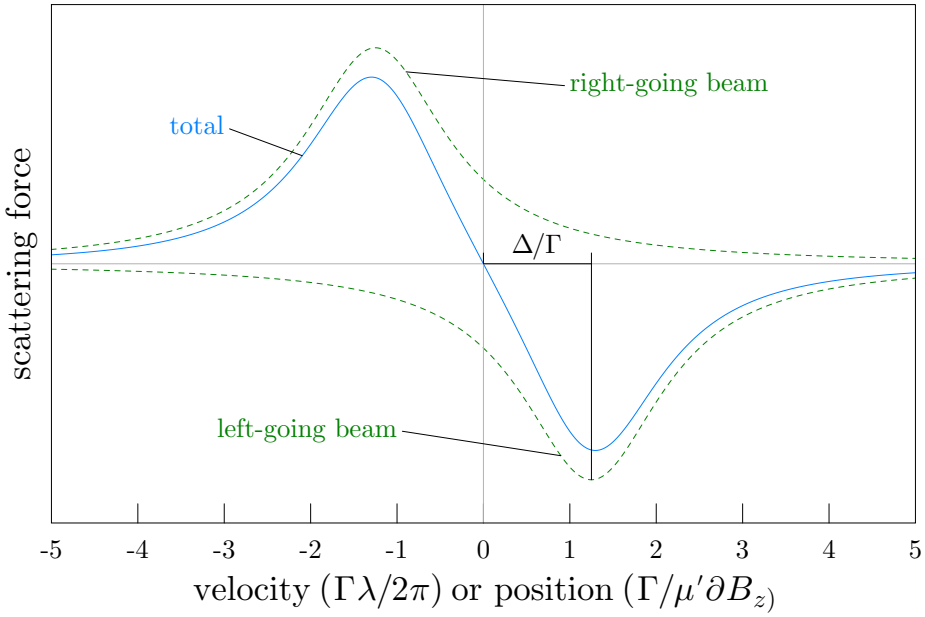

FIGURE A.1. Net scattering force of two beams traveling in opposite directions. The x-axis can either be considered to be velocity (corresponding to viscous damping) or position (harmonic restoring force), as discussed in the text.

This limit corresponds to atomic velocities which are 'contained' within the two Lorentzian lineshapes, and since $\Delta < 0$ for red-detuned light, the coefficient of v is strictly negative. The positive parameter β is defined to emphasize the linear dependence of the force on velocity, clearly consistent with viscous damping (as implied by the term 'molasses'). This cannot damp an atom's velocity all the way to zero, however, since the mechanism for removing energy relies on scattering photons in a random direction. This acts as a heating process—where the atom experiences a random walk in velocity, mediated by photon recoils—which balances the cooling in the molasses at a point called the Doppler cooling limit. For $\Delta = -\Gamma/2$ the temperature value is [221],

$$T_{\text{Doppler}} = \frac{\hbar\Gamma}{2k_{\text{B}}}. \tag{A.6}$$

	λ (nm)	$\Gamma/2\pi$ (MHz)	T_{Doppler} (μK)	T_{recoil} (μK)
^{23}Na	589	10	235	2.4
^{87}Rb	780	6	146	0.362
^{133}Cs	852	5.2	125	0.198
^{88}Sr	461	32	770	1.0
^{88}Sr	689	0.0075	0.180	0.460

TABLE A.1. Doppler and recoil temperatures for several atomic species. Also included are the cooling transition's wavelength and linewidth. The Doppler temperature for the 689 nm transition in ^{88}Sr is not well defined, as suggested by the fact that it is smaller than the recoil temperature.

This defines one temperature of significance in cold-atom physics, and when optical molasses were first formed, researchers were surprised to find the atoms were substantially cooler than this [221].[1]Another useful temperature reference is defined by the velocity of a single recoil event, and is called the recoil temperature,

$$T_{\text{recoil}} = \frac{\hbar^2 k^2}{k_{\text{B}} m}. \tag{A.7}$$

Example Doppler and recoil temperatures are listed in Table A.1 for several atomic species. Of special note for this thesis are the temperatures for the two transitions in ^{88}Sr. Because of the large linewidth, Doppler-cooling on the 461 nm transition results in a fairly hot sample of atoms. The 689 nm transition, on the other hand, is so narrow the $kv \ll \Gamma$ assumption in Eq. (A.5) does not apply and Doppler temperature is not a well-defined concept. In fact, the transition is so narrow, the change in frequency due to a single recoil is 4.8 kHz, on the same scale as the linewidth. The process of cooling in this regime are clearly a bit strange, and will be discussed more in Sec. 5.3

[1]Since mechanisms for sub-Doppler cooling do not apply to atoms with a spinless ground state, they are outside the scope of this thesis, but nice descriptions can be found in Refs. [222] and [2].

A.2. Magneto-Optical Trap

If we ignore velocity, and instead focus on the 1D Zeeman shift in Eq. (A.3), the mathematical analysis used above is similar except the magnitude of the frequency shift is replaced by $kv \rightarrow \tilde{\mu}B_z/\hbar$. Again, $\tilde{\mu}$ is effective magnetic moment of the transition, which is found by taking the difference of the ground and excited state moments, $\tilde{\mu} = \mu' - \mu = \mu_{\mathrm{B}}(m'_{J'}g'_{J'} - m_J g_J)$. Here, μ_{B} is the Bohr magneton, m_J is the magnetic quantum number of the atom (whose quantization axis is oriented with the magnetic field along the z-direction), and g_J is the level's Landé g-factor. Throughout this document, the prime shorthand is used to indicate the excited state.

To simplify discussion a little, let's assume that $m_J = 0$ and $-1 < m_{J'} < 1$ (which is actually true for ^{88}Sr), so the frequency shift is then $\Delta_{\mathrm{Zeeman}} = \mu_{\mathrm{B}}m'_{J'}g'_{J'}B_z/\hbar$. Spatially tuning the magnetic field can thus create a potential landscape where atoms are shifted into resonance with a laser and feel an increased scattering force. We can use this idea to create a 1D "trap" that uses the light force to confine atoms in a particular region. Using Fig. A.1 again for intuition, consider a positive magnetic field gradient with zero field at the origin, $B_z = (\partial B_z)z$ (where shorthand for the derivative is used, $\partial B_z := \partial B/\partial z$). When an atom has position $z > 0$, we want it to scatter light from the left-going beam to force it back toward the origin. This happens by ensuring the red-detuned laser light is coupled to $m_{J'} = -1$ to bring Δ_{eff} closer to zero. In contrast, an atom with position $z < 0$ should become resonant with a laser coupling to a sublevel $m_{J'} = +1$. Note that the lasers interact with different sublevels, which has the added benefit of *increasing* Δ_{eff} when a laser would be pushing the atoms away from $z = 0$.

The total force on an atom from the two laser beams is again the sum of two Lorentzians,

$$\begin{aligned} F_{\text{trap}} &= \frac{\hbar k \Gamma}{2} \left(\frac{s_0}{1 + s_0 + [2(\Delta - \mu_{\text{B}} g'_{j'} B_z/\hbar)/\Gamma]^2} - \frac{s_0}{1 + s_0 + [2(\Delta + \mu_{\text{B}} g'_{j'} B_z/\hbar)/\Gamma]^2} \right) \\ &\approx 4\hbar k^2 s_0 \, \frac{2\Delta/\Gamma}{\left[1 + s_0 + (2\Delta/\Gamma)^2\right]^2} \, \frac{\mu_{\text{B}} g'_{j'} \partial B_z}{\hbar k} \, z \\ &= -\kappa z, \end{aligned} \tag{A.8}$$

where the approximation is made for $\Delta_{\text{Zeeman}} \ll \Delta$ (again, the linear region near $z = 0$ contained between the two Lorentzians in Fig. A.1). This is a linear restoring force with spring constant κ. Thus the red-detuned lasers used in Doppler cooling can be extended to create a spatially confining potential by adding a linear magnetic field gradient and using circularly polarized light which couples to the appropriate magnetic sublevels. In the example above, the left-going and right-going beams should have polarizations of σ_- and σ_+, respectively. Note that these polarizations are with respect to the atom's quantization axis, however, and that the two beams will actually *both* have right-hand circular polarization in this case.

This is the simple 1D version of the magneto-optical trap (MOT), which is generalized to three dimensions by using six laser beams and anti-Helmholtz (AH) coils [223]. The lasers are typically derived from the same source, and thus have the same detuning, but their polarization requires some special attention. The magnetic quadrupole field created by the AH coils enters through the axis of the coil pair and exits uniformly in the lateral space between the two (or vice-versa, depending on the direction of current). Because $\nabla \cdot \mathbf{B} = 0$, the axial field gradient has the opposite sign of the transverse gradients and twice the magnitude. This means that if the lateral

confining beams are right-hand circularly polarized, then the axial beams must be left-hand circular.

A.3. Dipole Force and Optical Lattices

Thus far we have only considered actual absorption and emission events. This is not complete, however, because an off-resonant light field can create mechanical effects without directly driving excitations. In the two-level atom, the dipole interaction in the RWA produces an ac Stark shift of the ground state [39],

$$V = \frac{\hbar|\Omega|^2}{4\Delta}. \tag{A.9}$$

This is called the dipole potential, which—in contrast to the radiative pressure force—is largely conservative. *Confinement* of an atom in the ground state is therefore possible by creating gradients in intensity of a red-detuned beam, with deeper trap depths provided by higher intensity fields. Since detuning of the trapping beam is much larger than the atomic linewidth, relatively few photons are scattered and heating effects are small. These traps have long lifetimes and are useful for holding pre-cooled atoms during the course of an experiment.

One-dimensional traps are created by focusing a single beam to a small waist (often called a dipole trap) or by using two counter-propagating beams in a standing-wave configuration (called an optical lattice) [93]. An optical lattice can be created by overlapping two dipole traps via reflection, and because of interference, the lattice depth is four times greater than a single dipole trap with the same laser power. The resulting potential is modulated in space by half the laser's wavelength, and has an

the intensity envelope of a Gaussian beam [104],

$$V(r,z) = 4V_0 \ \cos^2(kz) \ \frac{w_0^2}{w^2(z)} \ \exp\left[-\frac{2r^2}{w^2(z)}\right], \tag{A.10}$$

where $w(z) = w_0\sqrt{1+(z/z_0)^2}$, and w_0 and z_0 are the minimum waist and Rayleigh length, respectively. The potential of each lattice site can be approximated as harmonic in both r and z, and the frequencies at the center of the lattice are [224]

$$f_z = \frac{2}{\lambda}\sqrt{\frac{2V_0}{m}} \tag{A.11}$$

$$f_r = \frac{2}{\pi w_0}\sqrt{\frac{V_0}{m}}. \tag{A.12}$$

Note that the spatial confinement in a lattice can be quite narrow in the z-direction. For instance, consider 1-μK ^{88}Sr atoms that are in a 10-μK-deep lattice at 914 nm. A rough estimate of the half width of the cloud of atoms is given by equating the harmonic and thermal energies, $m\omega_z^2 z^2 = k_{\mathrm{B}}T$, and for these parameters $2z \sim 30$ nm.

APPENDIX B

STRONTIUM DETAILS

This appendix presents some basic details about strontium which are used in calculations and discussions within the body of the thesis. The energy levels which are relevant to the trapping and cooling schemes we use are shown in Fig. B.1. A strong transition at 461 nm provides primary cooling in the Zeeman slowing and blue MOT stages, but the atoms have some probability to decay to the $J = 1$ and $J = 2$ fine structure states of the $5s\,5p\,{}^3P_J$ manifold. Unfortunately, the $J = 2$ level is quite long-lived, and atoms are lost to the blue cooling process if they are not pumped out of that state. There are several schemes in which to do this [225], and we use a turquoise beam at 497 nm to couple to the $5s\,5d\,{}^3D_2$ state.

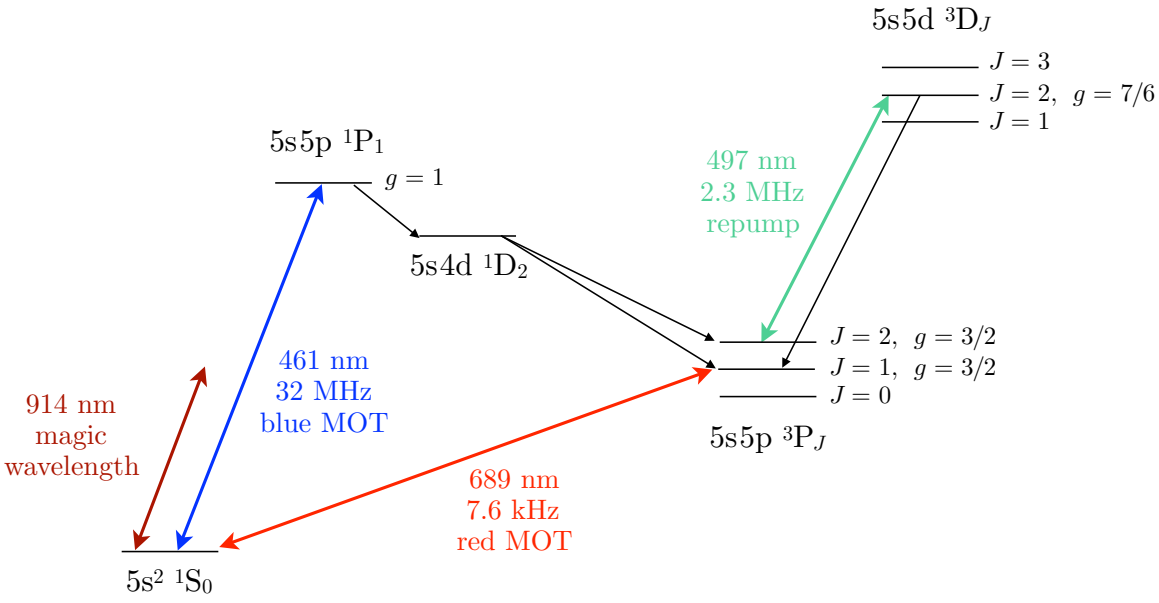

FIGURE B.1. Relevant energy levels used in trapping and cooling of neutral ^{88}Sr, including transition wavelengths, linewidths, and Landé g-factors. Also included is the 914 nm magic wavelength for the $5s^2\,{}^1S_0 \longrightarrow 5s\,5p\,{}^3P_1$ intercombination line.

Isotope	Abundance (%)	Mass (amu)	I	F'	$\Delta\nu_{461}$ (MHz)	$\Delta\nu_{689}$ (MHz)
^{88}Sr	82.58	87.905612	0	1	0	0
^{87}Sr	9.86	85.909260	9/2	7/2 9/2 11/2	-9.7 -68.9 -51.9	1352.0 221.7 -1241.5
^{86}Sr	7.00	86.908877	0	1	-124.8	-163.8
^{84}Sr	0.56	83.913425	0	1	-270.8	—

TABLE B.1. Principal isotope data for strontium [226], including abundance, mass, and isotopic shifts of the $5s^2\,{}^1S_0 \longrightarrow 5s\,5p\,{}^1P_1$ and $5s^2\,{}^1S_0 \longrightarrow 5s\,5p\,{}^3P_1$ transitions—labeled $\Delta\nu_{461}$ and $\Delta\nu_{689}$, respectively. Shifts are presented relative to ^{88}Sr, and are taken from Ref. [227] for the 461 nm transition and Refs. [228] and [229] for the 689 nm intercombination line. These data are presented visually in Fig. B.3.

Since Sr is an alkaline earth element, it has triplet states where the two valence electrons have aligned spins. The ${}^3P_J$ manifold has two transitions to the ground state which are doubly forbidden (they are forbidden both by total angular momentum consideration and because $S \neq S'$), offering extremely narrow linewidths that are exploited in the strontium optical lattice clocks in ^{87}Sr [19]. The semi-forbidden $J = 1$ intercombination line used for secondary cooling is only 7.6-kHz wide, and can cool atoms to sub-recoil temperatures [27].

The vapor pressure of Sr is significantly lower than that of alkali atoms, and is plotted in torr in Fig. B.2 using empirical data tabulated by C.B. Alcock [143],

$$\log_{10} p_{\mathrm{v}} = 5.006 + 9.226 - \frac{8572}{T} - 1.1926 \log_{10} T. \tag{B.1}$$

There are four naturally occurring isotopes of strontium [226]. Some of their properties are detailed in Table B.1, and frequency shifts of the 461-nm and 689-nm transitions are shown in Fig. B.3

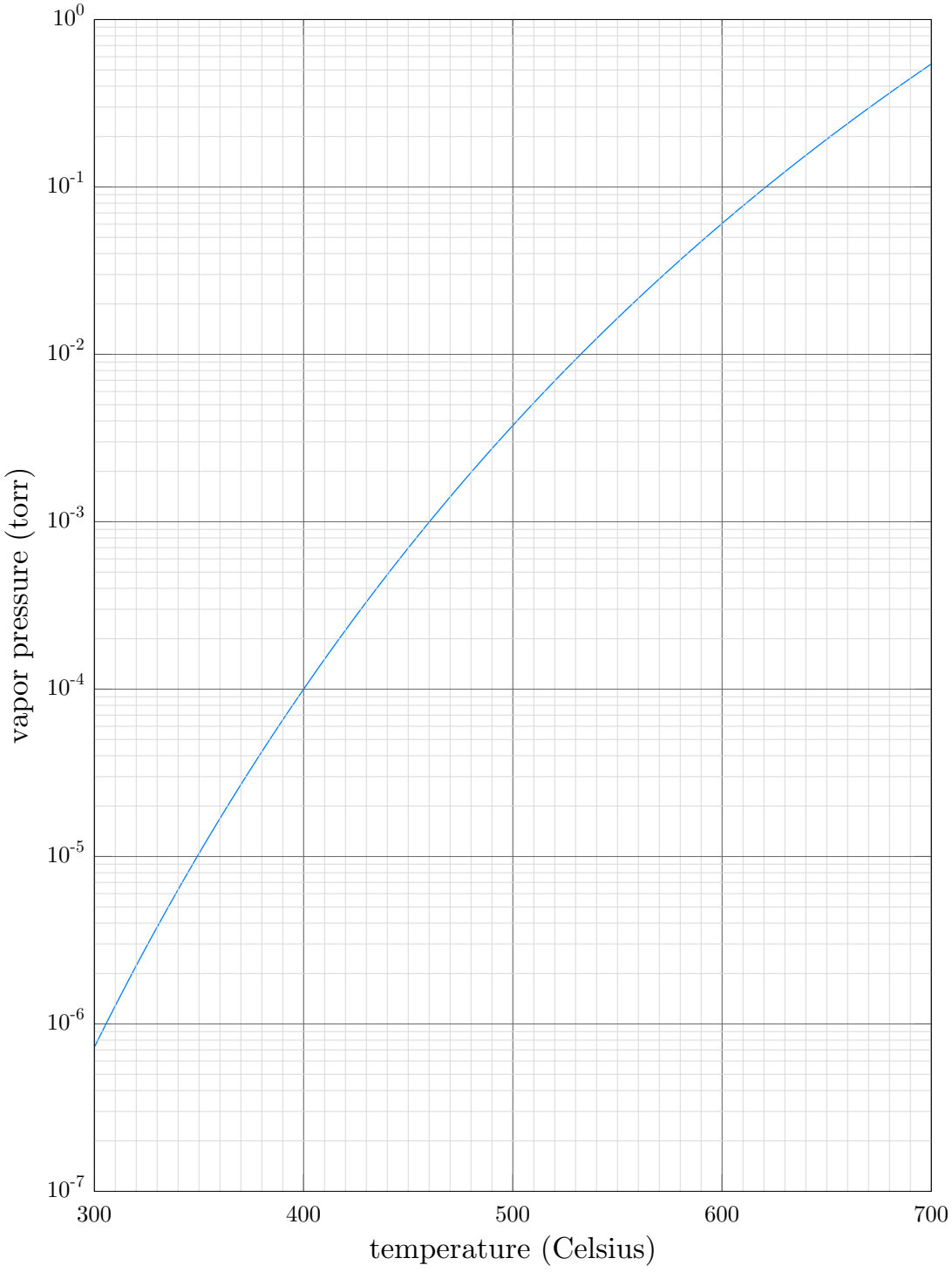

FIGURE B.2. Vapor pressure of strontium using empirical data from Ref. [143].

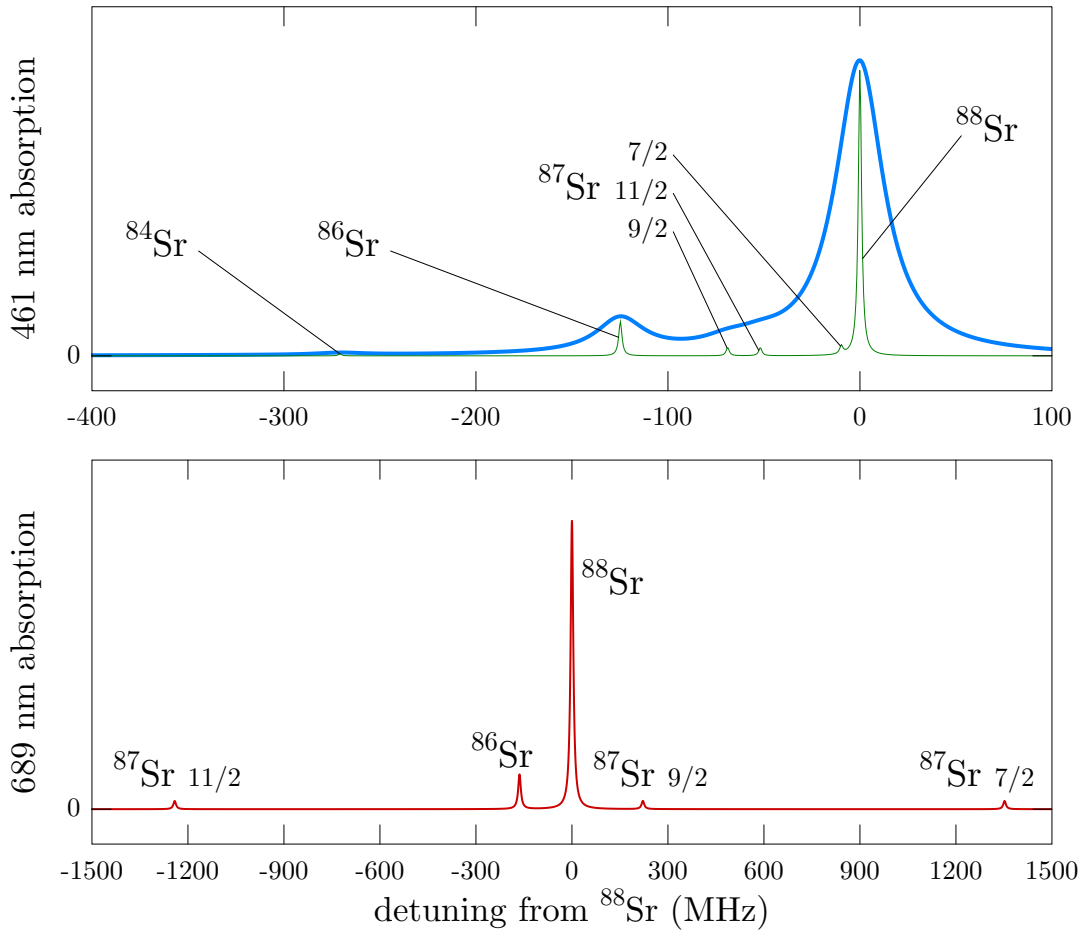

FIGURE B.3. Isotopic shifts of the blue MOT $5s^2\,{}^1S_0 \longrightarrow 5s\,5p\,{}^1P_1$ and red MOT $5s^2\,{}^1S_0 \longrightarrow 5s\,5p\,{}^3P_1$ transitions (top and bottom plots, respectively). Frequency differences are presented relative to ^{88}Sr, and to illustrate the absorption profile, lineshapes are plotted as Lorentzians whose heights are weighted by the abundance of each isotope. For the transition at 461 nm, a realistic curve (thick blue) uses linewidths of 32 MHz, but a version with linewidths of 2 MHz is also included (thin green) to more clearly show the individual isotopes. At 689 nm, meanwhile, the peaks shown are much broader than the actual transition (10 MHz compared to 7.6 kHz) for aesthetic appeal.

B.1. Dipole Matrix Elements

Calculations of quantities involving the Rabi frequency $\Omega(\mathbf{r})$ require the ability to compute dipole matrix elements. In general a sum over several transitions is necessary, and this Appendix lays some groundwork for performing calculations for strontium. The Rabi frequency is given by the dipole interaction between the atom and the electric field,

$$\Omega_q = \frac{-\langle F\ m_F|er_q|F'\ m'_F\rangle E_q}{\hbar} = \frac{-\langle J\ m_J|er_q|J'\ m'_J\rangle E_q}{\hbar}, \tag{B.2}$$

where subscript q indicates the polarization of light, and the primed and unprimed quantities are associated with the excited and ground states, respectively. The second equality is true for ^{88}Sr since it has no nuclear spin, and thus $\mathbf{F} = \mathbf{J} + \mathbf{I} = \mathbf{J}$. It is helpful to rewrite the matrix element using the Wigner-Eckart theorem [39]:

$$\langle J\ m_J|er_q|J'\ m'_J\rangle = \langle J\|e\mathbf{r}\|J'\rangle(-1)^{J'-1+m_J}\sqrt{2J+1}\begin{pmatrix} J' & 1 & J \\ m'_J & q & -m_J \end{pmatrix}, \tag{B.3}$$

where the object in parentheses is the the Wigner 3-j symbol. The result is a factorization into a geometric term and a reduced matrix element which no longer depends on the magnetic quantum number. Since the dipole does not interact with the spin of the electron, we can further simplify by decomposing into a reduced matrix

element involving just the orbital quantum number L,

$$\begin{aligned}\langle J\|e\mathbf{r}\|J'\rangle &\equiv \langle L\ S\ J\|e\mathbf{r}\|L'\ S'\ J'\rangle \\ &= \langle L\|e\mathbf{r}\|L'\rangle\delta_{SS'}(-1)^{J'+L+1+S}\sqrt{(2J'+1)(2L+1)}\begin{Bmatrix} L & L' & 1 \\ J' & J & S \end{Bmatrix},\end{aligned} \tag{B.4}$$

where the object in brackets this time is the Wigner 6-j symbol. Dipole matrix elements are computed using these reduced matrix elements and partial lifetimes of fine structure transitions [230],

$$\frac{1}{\tau_{J'J}} = \Gamma_{J'J} = \frac{\omega_{J'J}^3}{3\pi\epsilon_0\hbar c^3}\frac{2J+1}{2J'+1}|\langle J\|e\mathbf{r}\|J'\rangle|^2. \tag{B.5}$$

For strontium, available quantities are typically the overall lifetimes of excited state fine structure manifolds decaying into lower state manifolds. This is a sum over all possible decay paths,

$$\frac{1}{\tau_{L'L}} = \Gamma_{L'L} = \frac{1}{2S'+1}\sum_{J',J}\Gamma_{J'J}, \tag{B.6}$$

where the factor of $2S'+1$ is necessary because considering all $J' \to J$ possibilities essentially multiplies the $L' \to L$ decay rate by the number of J' states in the excited manifold. Plugging in the expression for $\langle J\|e\mathbf{r}\|J'\rangle$ in Equation B.5, the known decay rate is thus

$$\Gamma_{L'L} = \frac{|\langle L\|e\mathbf{r}\|L'\rangle|^2}{3\pi\epsilon_0\hbar c^3}\frac{1}{2S'+1}\sum_{J',J}\omega_{J'J}^3\,(2J+1)(2L+1)\begin{Bmatrix} L & L' & 1 \\ J' & J & S \end{Bmatrix}^2. \tag{B.7}$$

This makes calculating potentials for arbitrary states somewhat involved, since all $\omega_{J'J}$ frequency splittings must be used to first find $|\langle L\|e\mathbf{r}\|L'\rangle|^2$ before determining

the individual $\Gamma_{J'J}$ or $|\langle J\|e\mathbf{r}\|J'\rangle|^2$.[1] Such calculations are necessary to estimate the expected magic wavelengths for the $5s^2\,{}^1S_0 \longrightarrow 5s\,5p\,{}^3P_0$ clock and $5s^2\,{}^1S_0 \longrightarrow 5s\,5p\,{}^3P_1$ narrow-line cooling transitions [19, 89, 231], and to calculate the expected Casimir–Polder shifts presented in Chapter II. Note that the normalization convention used in this document is that of Brink and Satchler [232], which is different than what is used in the referenced magic wavelength calculations. The two reduced matrix elements are related by $\langle L\|e\mathbf{r}\|L'\rangle = \sqrt{2L+1}\langle L\|e\mathbf{r}\|L'\rangle$, with the matrix element on the right-hand-side being from this document.

B.1.1. Example: Ground State Dipole Potential

In the special case of transitions connected to strontium's ground state, the dipole matrix elements can be found immediately from the excited state lifetimes. Dipole interactions only couple the $5s^2\,{}^1S_0$ ground state to higher-lying ${}^1P_1$ singlet states, meaning there are only single $J' = 1 \to J = 0$ decay paths and therefore $\Gamma_{J'J} = \Gamma_{L'L}$. For linearly polarized light, the dipole matrix elements are then

$$|\langle J\ m_J|er_0|J'\ m'_J\rangle|^2 = \frac{1}{3}|\langle J\|e\mathbf{r}\|J'\rangle|^2 \tag{B.8}$$

$$= 3\pi\epsilon_0\hbar c^3\frac{\Gamma_{L'L}}{\omega^3_{J'J}}. \tag{B.9}$$

As an example calculation, these can be used to find the dipole potential the atom experiences when it's in the ground state. If the trapping laser is tuned very far from resonance, the RWA no longer applies. The dipole potential includes a counter-

[1] An alternative way to think about this [19, 89, 231] is combining the set of splittings $\omega_{J'J}$ and branching ratios to find the "center of mass" frequency between fine structure manifolds $\omega_{L'L}$ and then applying the L analog of Eq. (B.5)

rotating term (the Bloch–Siegert shift [233]),

$$V(\mathbf{r}) = -\frac{\hbar\Omega(\mathbf{r})^2}{4}\left(\frac{1}{\omega_\mathrm{L}+\omega_0} - \frac{1}{\omega_\mathrm{L}-\omega_0}\right), \tag{B.10}$$

where $\Omega(\mathbf{r})$ is the Rabi frequency, ω_0 is the atomic resonance, and ω_L is the laser frequency. The total ground state shift due to a linearly polarized field E_0 is thus a sum over states satisfying Eq. (B.9):

$$V(\mathbf{r}) = -\frac{3\pi\epsilon_0 c^3}{4}\, E_0^2 \sum_k \frac{\Gamma_k}{\omega_k^3}\left(\frac{1}{\omega_\mathrm{L}+\omega_k} - \frac{1}{\omega_\mathrm{L}-\omega_k}\right). \tag{B.11}$$

Here ω_k and Γ_k are the frequency splitting and decay rate from the kth excited state to the ground state, and we can compute the sum using the data presented in Table B.2. If we assume a Gaussian beam with waist parameter w_0 and power P, the maximum potential is

$$\begin{aligned} V(\mathbf{r}) =& -\frac{3c^2 P}{w_0^2}\sum_k \frac{\Gamma_k}{\omega_k^3}\left(\frac{1}{\omega_\mathrm{L}+\omega_k} - \frac{1}{\omega_\mathrm{L}-\omega_k}\right) \\ =& \frac{P}{w_0^2}\cdot\left(5.0160\times 10^{-37}\left[\mathrm{m}^2\cdot\mathrm{s}\right]\right), \end{aligned} \tag{B.12}$$

where we have assumed the laser to be operating at the 914 nm magic wavelength of the $5\mathrm{s}^2\,{}^1\mathrm{S}_0 \longrightarrow 5\mathrm{s}\,5\mathrm{p}\,{}^3\mathrm{P}_1$ intercombination line.

B.2. Casimir–Polder Level Shifts

In the case of an atom near a perfectly conducting plane, the atom–field interaction can be evaluated analytically to second order in perturbation theory. For

an arbitrary atomic level α the resulting CP shift is [39]

$$V_\alpha = \sum_j \frac{\mathrm{sgn}(\omega_{j\alpha})|\omega_{j\alpha}|^3}{4\pi\epsilon_0\pi c^3}\left[\left(\frac{d_{j,\parallel}^2}{2} - d_{j,z}^2\right)\frac{1}{z_j'}\left[f(z_j') - \Theta(\omega_{\alpha j})\pi\cos z_j'\right]\right.$$
$$- \left(\frac{d_{j,\parallel}^2}{2} + d_{j,z}^2\right)\left[\frac{1}{z_j'^2} + \left(\frac{2}{z_j'^3} - \frac{1}{z_j'}\right)\left[f(z_j') - \Theta(\omega_{\alpha j})\pi\cos z_j'\right]\right]$$
$$\left. - \left(\frac{d_{j,\parallel}^2}{2} + d_{j,z}^2\right)\frac{2}{z_j'^2}\left[g(z_j') - \Theta(\omega_{\alpha j})\pi\sin z_j'\right]\right]. \qquad \text{(B.13)}$$

Here $\omega_{j\alpha} := \omega_j - \omega_\alpha = -\omega_{\alpha j}$ is the level splitting, sgn( ) is the signum function, and $\Theta(\ )$ is the Heaviside step function. Again, f and g are auxiliary function of the sine and cosine integrals [Eq. (2.13)], and a rescaled position $z_j' = 2\omega_{j\alpha}z_j/c$ is also used. When $\omega_{j\alpha} > 0$ the level is coupled to higher-lying states, and the result is the same as Eq. (2.12) if the atom is assumed to be spherically symmetric. When $\omega_{j\alpha} < 0$, however, the coupling is to lower-lying states and the resulting oscillatory potential (in z) resembles that of a classical dipole [39].

The perpendicular and parallel dipole matrix elements are written compactly as $d_{j,\parallel}^2$ and $d_{j,z}^2$, respectively, with

$$d_{j,z}^2 = |\langle\alpha|\hat{z}\cdot\mathbf{d}|j\rangle|^2\ , \text{ and} \qquad \text{(B.14)}$$
$$d_{j,\parallel}^2 = |\langle\alpha|\hat{x}\cdot\mathbf{d}|j\rangle|^2 + |\langle\alpha|\hat{y}\cdot\mathbf{d}|j\rangle|^2.$$

For fine structure states, the Wigner 3-j symbols in Eq. (B.3) can be evaluated, and the dipole matrix elements are then written as m_J-dependent factors multiplying reduced dipole matrix elements:

$$d_{j,z}^2 = |\langle J, m_J | e r_0 | J', m_J \rangle|^2$$

$$= |\langle J \| e\mathbf{r} \| J' \rangle|^2 \times \begin{cases} 1/3, & J = 0 \to J' = 1 \\ 1 - m_J^2, & J = 1 \to J' = 0 \\ m_J^2/2, & J = 1 \to J' = 1 \\ (4 - m_J^2)/10, & J = 1 \to J' = 2 \\ (4 - m_J^2)/6, & J = 2 \to J' = 1 \\ m_J^2/6, & J = 2 \to J' = 2 \\ (9 - m_J^2)/21, & J = 2 \to J' = 3 \end{cases}, \tag{B.15}$$

$$d_{j,\|}^2 = |\langle J, m_J | e r_{+1} | J', m_J \rangle|^2 + |\langle J, m_J | e r_{-1} | J', m_J \rangle|^2$$

$$= |\langle J \| e\mathbf{r} \| J' \rangle|^2 \times \begin{cases} 2/3, & J = 0 \to J' = 1 \\ m_J^2, & J = 1 \to J' = 0 \\ 1 - m_J^2/2, & J = 1 \to J' = 1 \\ (6 + m_J^2)/10, & J = 1 \to J' = 2 \\ (2 + m_J^2)/6, & J = 2 \to J' = 1 \\ 1 - m_J^2/6, & J = 2 \to J' = 2 \\ (2 + m_J^2)/21, & J = 2 \to J' = 3 \end{cases}. \tag{B.16}$$

We use the various $\Gamma_{J'J}$ from the data tables in Sec. B.3 to calculate the reduced dipole matrix elements and evaluate the CP level shift for strontium's ground state and each of the magnetic sublevels in the $5s\,5p\,{}^3P_J$ triplet state. In addition to the tabulated transitions, we include the intercombination line when appropriate, where $\Gamma_{J'J} = 7.6$ kHz. The results are plotted in Fig. B.4, and the the oscillatory behavior of the ${}^3P_1$ excited state is clearly visible for $m_J = 1$.

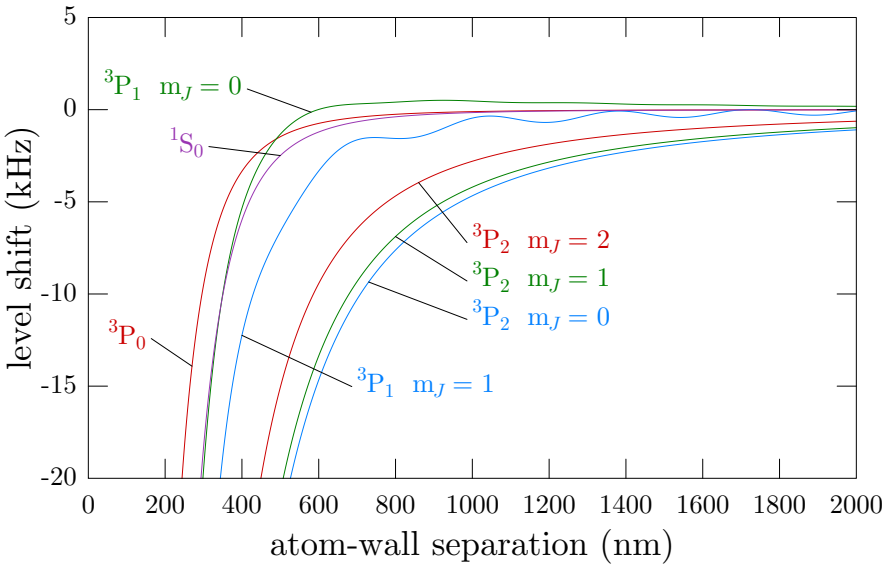

FIGURE B.4. Expected level shifts of strontium atoms near a perfect conductor, evaluated for the $5s^2\,{}^1S_0$ ground and $5s\,5p\,{}^3P_J$ triplet states. Differences between the excited- and ground-state shifts are plotted in Chapter II.

B.3. Tabulated Data

The following tables give spectroscopic data of various transitions connected to strontium's $5s^2\,{}^1S_0$ ground and $5s\,5p\,{}^3P_J$ triplet states. Wavelength and $\Gamma_{L'L}$ decay rate data are taken from Ref. [231], which compiled data from several sources [198, 234–236]. We use Eq. (B.7) to compute the reduced dipole matrix elements $|\langle L||e\mathbf{r}||L'\rangle|^2$ as well as partial decay rates $\Gamma_{J'J}$ to enable more straightforward calculation of expected shifts of individual fine-structure energy levels.

Exc. Orbital	λ (nm)	$\Gamma_{L'L}$ (Mrad/s)	source	$\|\langle L\|\|e\mathbf{r}\|\|L'\rangle\|^2$ ($C^2 \cdot m^2$)	$\Gamma_{L'L}/2\pi$ (MHz)
5s 5p	460.8618	190.01	expt [235]	1.9795×10^{-57}	30.2410
5s 6p	293.2685	1.87	expt [198]	5.0201×10^{-60}	0.2976
5s 7p	257.0238	5.32	expt [198]	9.6141×10^{-60}	0.8467
5s 8p	242.8826	14.9	thry [236]	2.2722×10^{-59}	2.3714
4d 5p	242.8100	12	thry [236]	1.8283×10^{-59}	1.9099
5s 9p	235.5027	11.6	thry [236]	1.6126×10^{-59}	1.8462
5s 10p	230.7980	7.6	thry [236]	9.9446×10^{-60}	1.2096
5s 11p	227.5921	4.88	thry [236]	6.1230×10^{-60}	0.7767

TABLE B.2. Reduced dipole matrix elements and total decay rates for transitions of the form $^1S_0 \longrightarrow ^1P_1$, originating from the $5s^2$ ground state.

N	J	J'	λ (nm)	$\Gamma_{L'L}$ (Mrad/s)	source	$\|\langle L\|\|e\mathbf{r}\|\|L'\rangle\|^2$ ($C^2 \cdot m^2$)	$\Gamma_{J'J}/2\pi$ (MHz)
6	0	1	679.2890	85	expt [94]	3.4090×10^{-58}	1.6263
	1	1	688.0208				4.6956
	2	1	707.2020				7.2063
7	0	1	432.7657	12	expt [237]	1.2093×10^{-59}	0.2231
	1	1	436.2933				0.6532
	2	1	386.6546				1.0335
8	0	1	378.1588	8.22	thry [236]	5.4922×10^{-60}	0.1519
	1	1	380.8495				0.4460
	2	1	386.6546				0.7104
9	0	1	355.4459	4.53	thry [236]	2.5068×10^{-60}	0.0835
	1	1	357.8221				0.2455
	2	1	362.9417				0.3920
10	0	1	343.5236	2.77	thry [236]	1.3818×10^{-60}	0.0510
	1	1	345.7426				0.1500
	2	1	350.5201				0.2399

TABLE B.3. Reduced dipole matrix elements and partial decay rates for transitions of the form $5s\,5p\,^3P_J \longrightarrow 5s\,Ns\,^3S_{J'}$ ($N = 6$–10).

N	J	J'	λ (nm)	$\Gamma_{L'L}$ (Mrad/s)	source	$\lvert\langle L\lvert\lvert e\mathbf{r}\rvert\lvert L'\rangle\rvert^2$ ($\mathrm{C}^2\cdot\mathrm{m}^2$)	$\Gamma_{J'J}/2\pi$ (MHz)
	0	0	–				–
	0	1	483.3459				6.64104
	0	2	–				–
	1	0	474.3244				18.8283
5	1	1	478.5654	120	expt [237]	4.7394×10^{-58}	4.8495
	1	2	487.7674				5.0432
	2	0	–				–
	2	1	472.3595				7.6337
	2	2	481.3222				14.3001

TABLE B.4. Reduced dipole matrix elements and partial decay rates for transitions of the form $5\mathrm{s}\,5\mathrm{p}\,{}^3\mathrm{P}_J \longrightarrow N\mathrm{p}^2\,{}^3\mathrm{P}_{J'}$.

N	J	J'	λ (nm)	$\Gamma_{L'L}$ (Mrad/s)	source	$\lvert\langle L\lvert\lvert e\mathbf{r}\rvert\lvert L'\rangle\rvert^2$ ($\mathrm{C}^2\cdot\mathrm{m}^2$)	$\Gamma_{J'J}/2\pi$ (MHz)
	0	1	2603.1254				0.0441
	0	2	–				–
	0	3	–				–
	1	1	2736.1990				0.0285
4	1	2	2692.1930	0.412	expt [238]	5.2050×10^{-58}	0.0538
	1	3	–				–
	2	1	3067.0208				0.0013
	2	2	3011.8377				0.0128
	2	3	2923.3748				0.0561
	0	1	483.3388				5.6352
	0	2	–				–
	0	3	–				–
	1	1	487.7432				4.1129
5	1	2	487.3849	61	expt [239]	4.2552×10^{-58}	7.4196
	1	3	–				–
	2	1	497.3051				0.2587
	2	2	496.9326				2.3334
	2	3	496.3643				9.3656
	0	1	394.1915				2.2589
	0	2	–				–
	0	3	–				–
	1	1	397.1161				1.6570
6	1	2	397.0383	24.62	expt [238]	9.2527×10^{-59}	2.9843
	1	3	–				–
	2	1	403.4318				0.1054
	2	2	403.3514				0.9488
	2	3	403.1512				3.8008

TABLE B.5. Reduced dipole matrix elements and partial decay rates for transitions of the form $5\mathrm{s}\,5\mathrm{p}\,{}^3\mathrm{P}_J \longrightarrow 5\mathrm{s}\,N\mathrm{d}\,{}^3\mathrm{D}_{J'}$ ($N = 4$–6).

N	J	J'	λ (nm)	$\Gamma_{L'L}$ (Mrad/s)	source	$\lvert\langle L\lvert\lvert e\mathbf{r}\rvert\lvert L'\rangle\rvert^2$ ($\mathrm{C}^2\cdot\mathrm{m}^2$)	$\Gamma_{J'J}/2\pi$ (MHz)
	0	1	363.0175				1.2993
	0	2	–				–
	0	3	–				–
	1	1	365.4964				0.9548
7	1	2	365.4307	14.2	thry [236]	4.1568×10^{-59}	1.7196
	1	3	–				–
	2	1	370.8396				0.0609
	2	2	370.7719				0.5488
	2	3	370.6953				2.1965
	0	1	347.8360				0.7777
	0	2	–				–
	0	3	–				–
	1	1	350.1113				0.5720
8	1	2	350.0670	8.51	thry [236]	2.1887×10^{-59}	1.0299
	1	3	–				–
	2	1	355.0111				0.0366
	2	2	354.9656				0.3293
	2	3	354.9094				1.3178
	0	1	339.0948				0.5032
	0	2	–				–
	0	3	–				–
	1	1	341.2568				0.3702
9	1	2	341.2568	5.51	thry [236]	1.3122×10^{-59}	0.6665
	1	3	–				–
	2	1	345.9102				0.0237
	2	2	345.9102				0.2133
	2	3	345.8528				0.8537

TABLE B.6. Reduced dipole matrix elements and partial decay rates for transitions of the form $5\mathrm{s}\,5\mathrm{p}\,{}^3\mathrm{P}_J \longrightarrow 5\mathrm{s}\,N\mathrm{d}\,{}^3\mathrm{D}_{J'}$ ($N = 7$–9).

APPENDIX C

DELAYED SELF-HETERODYNE METHOD

Optical frequency sources with narrow linewidths can be difficult to characterize. There are a few simple methods which are either impractical or do not work very well for narrow linewidths:

- An optical spectrum analyzer—a simple diffraction grating, for instance—measures a broad range of optical frequencies. The resolution is typically no better than a few GHz, and lasers with small $\delta f/f$ end up looking like a δ-function in frequency.

- It is possible to convert optical frequency fluctuations into a more reasonable quantity by passing the laser light through a high-Q optical resonator. The linewidth of the discriminating cavity, however, needs to be narrow relative to the laser (which can be costly), and this measurement cannot distinguish between noise on the laser and noise which perturbs the length of the resonator.

- Another approach is convert the laser spectrum from optical to radio frequency domains through heterodyne spectroscopy. This allows the narrow linewidth to be measured directly by high-resolution RF spectrum analyzers, but can be cumbersome because it requires a second laser that has similar frequency (different by at most a few GHz) and bandwidth as the target laser.

An alternative and more practical option is to beat the laser in question against a time-delayed, frequency-shifted version of itself. This "delayed self-heterodyne" technique is very similar to the final point above, except a narrow reference is not required.

Since it is a fairly common trick [240–244], this Appendix is meant as an overview to give intuition to well-established theoretical work [131, 132, 245]. First, a simple model [133] is shown to give rise to the expected Lorentzian line shape due to random phase noise. Next, the heterodyne and self-heterodyne techniques are discussed in the case of purely white noise. Finally, $1/f$ noise is added and details are given regarding how to extract a laser's linewidth from the output of a photodetector.

C.1. Mathematical Framework

In this section we hold off on discussing *how* we measure a laser's linewidth and instead develop some mathematical tools to help us analyze the methods discussed later. A laser's linewidth can be attributed to many processes, like collisional broadening and spontaneous emission, but we will use a simple model that lumps all these together into a single, randomized phase. That is, assuming a monochromatic plane wave, the laser's electric field is given by

$$E_{\text{L}}(t) = E_0 e^{i[\omega_0 t + \phi(t)]}, \tag{C.1}$$

where $\phi(t)$ is a stochastic, random variable. We assume no amplitude noise and ignore shot noise throughout this analysis because they do not change the resulting lineshape, which is our primary concern. We also will be using two-sided frequency functions, taking the positive frequencies to be the relevant quantity [130].

The (two-sided) power spectrum of the laser's electric field, according to the Wiener-Khinchin theorem, is given by the Fourier transform of the autocorrelation

function

$$S_E(\omega) = \int_{-\infty}^{+\infty} C_E(\tau) e^{-i\omega\tau} d\tau$$
$$= \int_{-\infty}^{+\infty} \big\langle E^*(t)E(t+\tau)\big\rangle e^{-i\omega\tau} d\tau. \tag{C.2}$$

Plugging in Eq. (C.1) and defining the quantity $\Delta\phi(t,\tau) := \phi(t+\tau) - \phi(t)$, known as the phase fluctuation or jitter, we find for the autocorrelation function

$$\big\langle E^*(t)E(t+\tau)\big\rangle = e^{i\omega_0\tau}\big\langle e^{i\Delta\phi(t,\tau)}\big\rangle$$
$$= e^{i\omega_0\tau} e^{-\frac{1}{2}\langle\Delta\phi^2(t,\tau)\rangle}. \tag{C.3}$$

The simplification has been made by using the integral representation of the expectation value, completing the square in the exponential, and using the fact that $\Delta\phi$ is a Gaussian random variable of mean value zero. The mean-square phase fluctuation can be broken down into correlation functions of phase,

$$\big\langle\Delta\phi^2(t,\tau)\big\rangle = \langle\phi^2(t+\tau)\rangle + \langle\phi^2(t)\rangle - \langle\phi(t+\tau)\phi(t)\rangle - \langle\phi(t)\phi(t+\tau)\rangle$$
$$= C_\phi(0) + C_\phi(0) - C_\phi(-\tau) - C_\phi(\tau), \tag{C.4}$$

and we can again make use of the Wiener-Khinchin theorem—this time the inverse. That is, the autocorrelation, $C_i(\tau)$, of a quantity i is the inverse Fourier transform of its power spectral density, $S_i(\omega)$. Thus the mean-square phase fluctuation is expressed

in terms of a phase-fluctuation spectrum,

$$\begin{aligned}\left\langle \Delta\phi^2(t,\tau)\right\rangle &= \frac{1}{2\pi}\int_{-\infty}^{+\infty}\left\{\left[S_\phi(\omega)+S_\phi(\omega)\right]e^{i\omega 0} - S_\phi(\omega)(-\omega)e^{i\omega\tau} - S_\phi(\omega)e^{i\omega\tau}\right\}d\omega \\ &= \frac{1}{2\pi}\int_{-\infty}^{+\infty} S_\phi(\omega)\left[2-e^{-i\omega\tau}-e^{i\omega\tau}\right]d\omega \\ &= \frac{1}{\pi}\int_{-\infty}^{+\infty} S_\phi(\omega)\Big[1-\cos(\omega\tau)\Big]d\omega \\ &= \frac{2}{\pi}\int_{-\infty}^{+\infty} S_\phi(\omega)\sin^2\left(\omega\tau/2\right)d\omega. \end{aligned} \tag{C.5}$$

Now, $\omega = d\phi/dt$ implies $S_\phi(\omega) = S_\omega(\omega)/\omega^2$ [130] (write $S_\omega(\omega)$ as a time-averaged function of ϕ and integrate by parts), which allows us to work with frequency-fluctuation spectra. In the case where $S_\omega(\omega)$ is independent of frequency—that is the frequency jitter is a white-noise process—the result is

$$\begin{aligned}\left\langle \Delta\phi^2(t,\tau)\right\rangle &= \frac{2S_\omega}{\pi}\int_{-\infty}^{\infty}\frac{1}{\omega^2}\sin^2\left(\omega\tau/2\right)d\omega \\ &= \frac{S_\omega\tau^2}{2\pi}\int_{-\infty}^{\infty}\left(\frac{\sin(\omega\tau/2)}{\omega\tau/2}\right)^2 d\omega \\ &= S_\omega|\tau| \\ &=: \gamma|\tau|. \end{aligned} \tag{C.6}$$

We have used integral properties of the sinc function and noticed that $\left\langle \Delta\phi^2(t,\tau)\right\rangle \geq 0$. After plugging into Eq. (C.3) and taking the Fourier transform, the resultant power spectrum of the electric field is a Lorentzian distribution centered at ω_0 with full width at half maximum (FWHM) of γ:

$$S_{_E}(\omega) = \frac{{E_0}^2}{\pi}\,\frac{\gamma/2}{(\gamma/2)^2+(\omega-\omega_0)^2}. \tag{C.7}$$

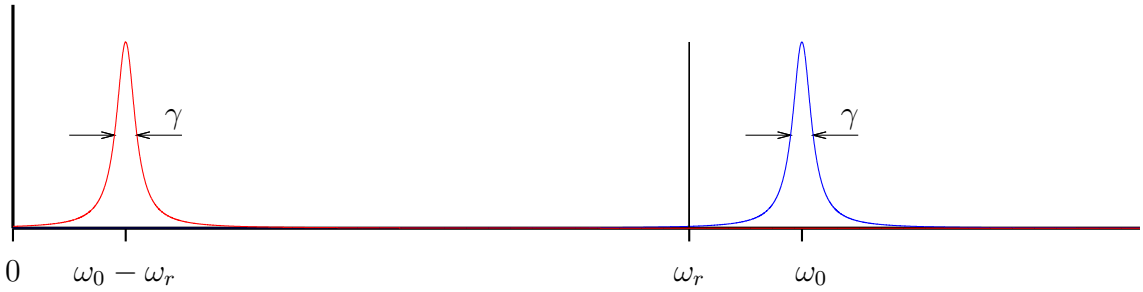

FIGURE C.1. Frequency spectrum of a laser with linewidth γ centered at frequency ω_0 (blue) beaten against a single-frequency plane wave (black) with frequency ω_r. The resulting beat note (red) is centered at $\omega_0 - \omega_r$ and also has linewidth γ.

Note that we have adopted the definition $S_\omega = \gamma$ rather than $S_\omega = 2\gamma$ (as in [131, 245]) because we want γ to represent the FWHM laser linewidth.

So, assuming a white-noise process and modeling it using a stochastic phase, we recover the expected result and generate some useful identities in the process. In particular, we will again use the simplification in Eq. (C.3) and the result of Eq. (C.5).

C.2. Heterodyne Measurement

As a useful introduction, consider a special case of heterodyne spectroscopy. Here the target laser is interfered with a *perfect* laser that has zero linewidth under this model. That is, the reference laser is monochromatic and its power spectrum $S_E(\omega)$ is a delta function in frequency space. We expect the resulting beat signal to have the same line shape as the target laser, but centered at the frequency difference of the two lasers (see Fig. C.1).

If the two electric field amplitudes of the two lasers are related by a factor of α, the combined field is

$$\begin{aligned} E_{\text{total}}(t) &= E_{\text{L}}(t) + E_{\text{ref}}(t) \\ &= E_0 e^{i[\omega_0 t + \phi(t)]} + \alpha E_0 e^{i\omega_r t}. \end{aligned} \tag{C.8}$$

This field is measured on a photodetector, which produces a signal current proportional to the square of the field. The resulting power spectrum is then the Fourier transform of the current autocorrelation function $C_I(\tau)$. Ignoring shot noise and dropping constants of proportionality, the autocorrelation function is

$$\begin{aligned} C_I(\tau) &= \langle I^*(t) I(t+\tau) \rangle \\ &\propto \langle E^*(t) E(t) E^*(t+\tau) E(t+\tau) \rangle \\ &= \Big\langle \left(E_0 e^{-i(\omega_0 t + \phi(t))} + \alpha E_0 e^{-i\omega_r t}\right) \left(E_0 e^{i(\omega_0 t + \phi(t))} + \alpha E_0 e^{i\omega_r t}\right) \times \\ &\quad \left(E_0 e^{-i(\omega_0 (t+\tau) + \phi(t+\tau))} + \alpha E_0 e^{-i\omega_r (t+\tau)}\right) \left(E_0 e^{i(\omega_0 (t+\tau) + \phi(t+\tau))} + \alpha E_0 e^{i\omega_r (t+\tau)}\right) \Big\rangle. \end{aligned} \tag{C.9}$$

Of the sixteen terms, many turn out to be zero under a time average, $\langle e^{ixt} \rangle = 0$. The result is four frequency-independent terms and two others, which happen to be complex conjugates,

$$\begin{aligned} C_I(\tau) &\propto {E_0}^4(\alpha^2+1)^2 + {E_0}^4 \alpha^2 \left[e^{-i(\omega_0 - \omega_r)\tau} \left\langle e^{-i\Delta\phi(t,\tau)} \right\rangle + e^{i(\omega_0 - \omega_r)\tau} \left\langle e^{i\Delta\phi(t,\tau)} \right\rangle \right] \\ &= {E_0}^4(\alpha^2+1)^2 + 2{E_0}^4 \alpha^2 e^{\langle \Delta^2 \phi(t,\tau) \rangle / 2} \cos\left[(\omega_0 - \omega_r)\tau\right]. \end{aligned} \tag{C.10}$$

We have again used $\Delta\phi = \phi(t+\tau) - \phi(t)$ and applied the identity from Eq. (C.3). Defining $\Omega = \omega_0 - \omega_r$, again assuming $S_\omega(\omega) = \gamma$, and evaluating the Fourier

transform, the measured current spectrum becomes

$$S_I(\omega) \propto 2\pi {E_0}^4(\alpha^2+1)^2\delta(\omega) + \frac{2{E_0}^4\alpha^2}{\pi}\left[\frac{\gamma/2}{(\gamma/2)^2+(\omega-\Omega)^2} + \frac{\gamma/2}{(\gamma/2)^2+(\omega+\Omega)^2}\right]. \tag{C.11}$$

This spectrum is simply a delta function at zero frequency and two Lorentzians, centered at $\pm\Omega$. In principle, there should be a frequency-independent term that comes from shot noise, but since that does not alter the shape of the power spectrum, it can be ignored. Note that if two identical lasers are used in such a heterodyne measurment, the derivation changes slightly, but the resulting spectrum has a linewidth of 2γ, with each laser contributing equally to the total noise [39].

C.3. Delayed Self-Heterodyne Measurement

More practical than the heterodyne technique, the delayed self-heterodyne setup requires only a single laser. As pictured in Fig. 3.9, a laser is interfered with a time-delayed and frequency-shifted version of itself (the frequency shift makes the resultant RF spectrum easier to measure by shifting it away from dc). This is easily achieved by coupling the zeroth order of an AOM into a long fiber and combining the output with the AOM's first-order beam on a beamsplitter. Note that we can delay either order of the AOM, which operates at a frequency Ω, but choose the zeroth for power considerations in a lossy fiber. Without a delay, phase fluctuations in the two beams are entirely correlated, and the measured power spectral density gives no information about the laser's linewidth. As the delay time $t_d = L_{\text{fiber}}/c_{\text{fiber}}$ increases, however, the two beams become more independent, and the result converges toward that of the heterodyne measurement.

The previous sections explicitly demonstrated the method used to calculate the photocurrent's power spectral density, but providing in-depth calculations for the self-heterodyne technique is beyond the scope of this appendix. What follows will outline the results presented in the literature [131, 132], with the details from the previous pages adding clarity to the process (for a more detailed discussion—which also uses the more experimentally relevant one-sided spectral density functions—see the second chapter of Dan Steck's Quantum Optics notes [39]).

The model for the electric field is the same as before, but now we combine the laser with itself,

$$E_{\text{total}}(t) = E_{\text{L}}(t - t_d) + \alpha E_{\text{L}}(t) e^{i\Omega t} \tag{C.12}$$

$$= E_0 e^{i[\omega_0(t-t_d)+\phi(t-t_d)]} + \alpha E_0 e^{i[(\omega_0+\Omega)t+\phi(t)]}, \tag{C.13}$$

where α is again the ratio of amplitudes between the two fields and Ω is the frequency difference (the operation frequency of the AOM). Again ignoring shot noise, the autocorrelation function on the detector is

$$\begin{aligned} C_I(\tau) &\propto \langle E^*(t)E(t)E^*(t+\tau)E(t+\tau)\rangle \\ &= {E_0}^4(\alpha^2+1)^2 + 2{E_0}^4\alpha^2\cos(\Omega\tau)\,\exp\left(-\frac{\left[\Delta\phi(t,\tau)+\Delta\phi(t-t_d,\tau)\right]^2}{2}\right), \end{aligned} \tag{C.14}$$

where again many terms have averaged to zero. The exponential term can be rewritten in in a useful way [131] which allows the identity of Eq. (C.5) to be repeatedly applied:

$$-\frac{\left[\Delta\phi(t,\tau)+\Delta\phi(t+t_d,\tau)\right]^2}{2} = -\Delta\phi^2(\tau)-\Delta\phi^2(t_d)+\frac{\Delta\phi^2(\tau+t_d)}{2}+\frac{\Delta\phi^2(\tau-t_d)}{2}$$
$$= \frac{4}{\pi}\int_{-\infty}^{\infty}\frac{S_\omega(\omega)}{\omega^2}\sin^2\left(\frac{\omega\tau}{2}\right)\sin^2\left(\frac{\omega t_d}{2}\right)d\omega. \qquad \text{(C.15)}$$

Thus, after dropping terms with no frequency dependence, we obtain

$$S_I(\omega)\propto\int_{-\infty}^{\infty}d\tau e^{-i\omega\tau}\cos(\Omega\tau)\exp\left[\frac{4}{\pi}\int_{-\infty}^{\infty}\frac{S_\omega(\omega')}{\omega'^2}\sin^2\left(\frac{\omega'\tau}{2}\right)\sin^2\left(\frac{\omega' t_d}{2}\right)d\omega'\right]. \qquad \text{(C.16)}$$

as the resulting power spectral density of the photodiode current.

C.3.1. White Noise

In general, the Fourier transform must be performed numerically, but the case of white noise $S_\omega(\omega')=\gamma$ has an analytical result [245]:

$$S_I(\omega)\propto\int_{-\infty}^{\infty}d\tau e^{-i\omega\tau}\cos(\Omega\tau)\exp\left(-\gamma\min\{|\tau|,|t_d|\}\right)$$
$$= \exp(-\tilde{t})\delta(\gamma\tilde{\omega})+\frac{1}{\gamma}\frac{1}{1+\tilde{\omega}^2}\left[1-\exp(-\tilde{t})\left(\frac{1}{\tilde{\omega}}\sin\left(\tilde{\omega}\tilde{t}\right)+\cos\left(\tilde{\omega}\tilde{t}\right)\right)\right]. \qquad \text{(C.17)}$$

Here $\tilde{\omega}=(\omega-\Omega)/\gamma$ is the frequency difference measured in linewidths, and $\tilde{t}=t_d\gamma=t_d/\tau_c$ expresses the time delay in terms of the coherence time τ_c of the laser. The spectrum consists of a delta function and a Lorentzian centered at Ω. The Lorentzian is broadened by an oscillatory term, whose contribution is exponentially suppressed with increasing delay times. The interpretation is that the delta function comes from sampling when the two beams are still perfectly correlated, and the oscillatory piece

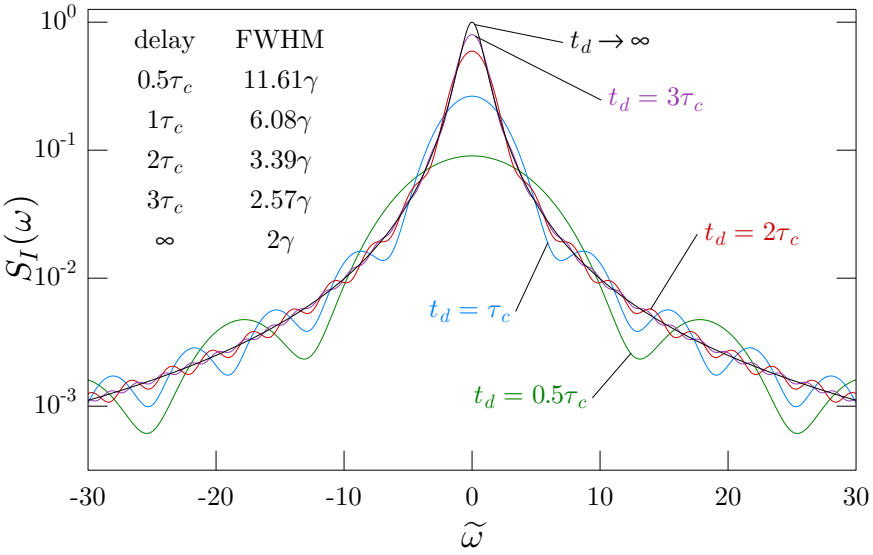

FIGURE C.2. Plot of analytical solutions of the photocurrent power spectrum in the delayed self-heterodyne technique for $S_\omega(\omega) = \gamma$ (white noise), see Eq. (C.17). Spectra are plotted for a variety of values of time delay, expressed in terms of the coherence length of the laser, $\tau_c = 1/\gamma$, and corresponding full width at half maximum (FWHM) are given. Periodicity of the wiggles in the wings of the spectra are determined by the length of the delay fiber.

represents residual coherence when the delay is not long compared to the coherence time. The result is plotted (without the delta-function) in Fig. C.2 for several delay times. For short delays, the broadening and scalloping of the Lorentzian is significant, but as the length of the fiber delay is increased, the oscillations become shallower and more closely spaced until they disappear entirely. As $t_d \to \infty$, the spectrum's FWHM linewidth converges to 2γ, which was the heterodyne result. From the perspective of making a quick measurement in the lab, note that the HWHM gives an upper bound of the white-noise parameter γ, regardless of the length of delay fiber (but also notice how bad this estimate gets for delay times less than τ_c). It is also possible to estimate the length of a (shorter) fiber using the periodic structure of the wings of the spectrum. If the linewidth of a laser is quite narrow, however, eliminating coherent behavior is impractical and the lineshape should be fit to determine γ. (For example,

if $\gamma = 1$ kHz, the coherence length $L_c = c_{\text{fiber}}/\gamma = 200$ km, which will yield extremely low output powers due to Rayleigh scattering if the laser does not operate at telecom wavelengths).

C.3.2. Adding $1/f$ Noise

For a gas-medium source (such as a He–Ne laser), it is a good approximation to include only white noise in modeling the laser's linewidth. Semiconductor devices, however, exhibit the $1/f$ or "flicker" noise inherent in all electronics, and we need to include an additional term in the frequency spectral noise density [246]:

$$S_\omega(\omega) = \gamma + \frac{k}{|\omega|}. \tag{C.18}$$

The $1/f$ component dominates laser linewidth, especially on long timescales since the noise diverges for small frequencies. Under the delayed self-heterodyne setup, we plug in the frequency spectral density and evaluate the integral in the exponent of Eq. (C.16) [132],

$$S_I(\omega) \propto \int_{-\infty}^{\infty} d\tau e^{-i\omega\tau} \cos(\Omega\tau) \exp\big(-\gamma \min\{|\tau|, |t_d|\}\big) \times \left[|\tau + t_d|^{-k(\tau+t_d)^2/2\pi} |\tau - t_d|^{-k(\tau-t_d)^2/2\pi} |\tau|^{k\tau^2/\pi} |t_d|^{kt_d^2/\pi|} \right]. \tag{C.19}$$

At this point numerical methods must be used to compute the Fourier transform and obtain the current power spectral density.

C.3.3. Laser Linewidth and Observation Time

Unfortunately, as $t_d \to \infty$ the integrand in Eq. (C.19) diverges for large τ. This means that in the heterodyne case, the $1/f$-noise component causes the laser to have infinite linewidth (which is quickly clear when trying to evaluate the integral in Eq. (C.5) with $\omega^2|\omega|$ in the denominator). Because of divergent noise at low frequencies, the laser's free-running frequency is unbounded and can—over long enough times—run away without returning to its initial value. This is why stating a laser's linewidth should always be accompanied with a specification of the *observation time* over which it is monitored.

In the case of Eq. (C.19), experimental constraints already fix the divergence in some sense. A spectrum analyzer's resolution bandwidth (RBW) determines the smallest frequency that can be resolved, therefore cutting off timescales above the instrument's acquisition time. As an example, a Gaussian RBW implies that the total spectrum measured on the analyzer is the convolution of $S_I(\omega)$ with a Gaussian of FWHM δ_{RBW}, and Eq. (C.19) is then modified to be

$$S_I(\omega) \propto \int_{-\infty}^{\infty} d\tau e^{-i(\omega-\Omega)\tau} \exp\big(-\gamma \min\{|\tau|,|t_d|\} - (\delta_{\mathrm{RBW}}\tau)^2/16\ln 2\big) \times \Big[|\tau+t_d|^{-k(\tau+t_d)^2/2\pi} |\tau-t_d|^{-k(\tau-t_d)^2/2\pi} |\tau|^{k\tau^2/\pi} |t_d|^{kt_d^2/\pi}\Big], \quad \text{(C.20)}$$

where we have for convenience also expanded the $\cos(\Omega\tau)$ term and dropped the mirror image of the spectral feature, centered at $\omega = -\Omega$ (this is allowed if $\Omega \gg \gamma$ and the tail of one peak does not contribute to the other). This result is representative of what is measured in the lab, and we can use Eq. (C.20) to characterize the γ and k parameters of a laser [116].

Declaring the linewidth of the laser with $1/f$ noise is another matter, however. Stating that the linewidth is infinite, while thought-provoking, is not very useful. The laser's unbounded frequency means that the time-averaged phase jitter $\langle \Delta\phi(\tau, t) \rangle \neq 0$ for finite times and the identity in Eq. (C.3) is not true (it should really involve the variance, reading $\langle e^{\pm ix} \rangle = e^{-\mathrm{Var}(x)/2}$). Statistical averages involving $\Delta\phi(t, \tau)$ are instead calculated over a specified time T_{obs} [247], which alters the integrand in Eq. (C.5). Photocurrent power spectral densities can be calculated with these new statistics, and the FWHM linewidth can in turn be calculated for known γ and k parameters at arbitrary T_{obs} [39].

REFERENCES CITED

[1] A. Ashkin, "Atomic-beam deflection by resonance-radiation pressure," Phys. Rev. Lett. **25**, 1321–1324 (1970).

[2] William D. Phillips, "Nobel Lecture: Laser cooling and trapping of neutral atoms," Rev. Mod. Phys. **70**, 721–741 (1998).

[3] Mark A. Kasevich, Erling Riis, Steven Chu, and Ralph G. Devoe, "rf spectroscopy in an atomic fountain," Phys. Rev. Lett. **63**, 612–615 (1989).

[4] Alexander D. Cronin, Jörg Schmiedmayer, and David E. Pritchard, "Optics and interferometry with atoms and molecules," Rev. Mod. Phys. **81**, 1051–1129 (2009).

[5] M. H. Anderson, J. R. Ensher, M. R. Matthews, C. E. Wieman, and E. A Cornell, "Observation of Bose-Einstein Condensation in a Dilute Atomic Vapor," Science (80-.). **269**, 198–201 (1995).

[6] M. R. Matthews, B. P. Anderson, P. C. Haljan, D. S. Hall, C. E. Wieman, and E. A. Cornell, "Vortices in a Bose-Einstein Condensate," Phys. Rev. Lett. **83**, 2498–2501 (1999).

[7] Markus Greiner, Olaf Mandel, Tilman Esslinger, Theodor W. Hänsch, and Immanuel Bloch, "Quantum phase transition from a superfluid to a Mott insulator in a gas of ultracold atoms," Nature **415**, 39–44 (2002).

[8] T. L. Gustavson, P. Bouyer, and M. A. Kasevich, "Precision Rotation Measurements with an Atom Interferometer Gyroscope," Phys. Rev. Lett. **78**, 2046–2049 (1997).

[9] Susannah M. Dickerson, Jason M. Hogan, Alex Sugarbaker, David M. S. Johnson, and Mark A. Kasevich, "Multiaxis inertial sensing with long-time point source atom interferometry," Phys. Rev. Lett. **111**, 1–5 (2013).

[10] Dimtry Budker and Michael Romalis, "Optical magnetometry," Nat. Phys. **3**, 227–234 (2007).

[11] J. D. Carter and J. D. D. Martin, "Coherent manipulation of cold Rydberg atoms near the surface of an atom chip," Phys. Rev. A - At. Mol. Opt. Phys. **88**, 1–7 (2013).

[12] Pierre Cladé, Estefania De Mirandes, Malo Cadoret, Saïda Guellati-Khélifa, Catherine Schwob, Francois Nez, Lucile Julien, and Francois Biraben, "Determination of the fine structure constant based on bloch oscillations of ultracold atoms in a vertical optical lattice," Phys. Rev. Lett. **96**, 2–5 (2006).

[13] J. J. Hudson, D. M. Kara, I. J. Smallman, B. E. Sauer, M. R. Tarbutt, and E. A. Hinds, "Improved measurement of the shape of the electron," Nature **473**, 493–496 (2011).

[14] C. W. Chou, D. B. Hume, T. Rosenband, and D. J. Wineland, "Optical clocks and relativity," Science **329**, 1630–1633 (2010).

[15] Hidetoshi Katori, Tetsuya Ido, Yoshitomo Isoya, and Makoto Kuwata-Gonokami, "Magneto-Optical Trapping and Cooling of Strontium Atoms down to the Photon Recoil Temperature," Phys. Rev. Lett. **82**, 1116–1119 (1999).

[16] Xinye Xu, Thomas H Loftus, John L Hall, Alan Gallagher, and Jun Ye, "Cooling and trapping of atomic strontium," J. Opt. Soc. Am. B **20**, 968 (2003).

[17] F. Sorrentino, G. Ferrari, Poli N., R. Drullinger, and G. M. Tino, "Laser cooling and trapping of atomic strontium for ultracold atoms physics, high-precision spectroscopy and quantum sensors," Mod. Phys. Lett. B **20**, 1287–1320 (2006).

[18] Masao Takamoto, Feng-Lei Hong, Ryoichi Higashi, and Hidetoshi Katori, "An optical lattice clock." Nature **435**, 321–4 (2005).

[19] Martin M. Boyd, *High precision spectroscopy of strontium in an optical lattice: Towards a new standard for frequency and time*, Ph.D. dissertation, UC Boulder (2007).

[20] S. T. Cundiff and J. Ye, "Colloquium: Femtosecond optical frequency combs," Rev. Mod. Phys. **75**, 325–342 (2003).

[21] T. L. Nicholson, S. L. Campbell, R. B. Hutson, G. E. Marti, B. J. Bloom, R. L. McNally, W. Zhang, M. D. Barrett, M. S. Safronova, G. F. Strouse, W. L. Tew, and J. Ye, "Systematic evaluation of an atomic clock at 2×10^{-18} total uncertainty." Nat. Commun. **6**, 6896 (2015).

[22] S. B. Koller, J. Grotti, St. Vogt, A. Al-Masoudi, S. Dörscher, S. Häfner, U. Sterr, and Ch. Lisdat, "A transportable optical lattice clock with 7×10^{-17} uncertainty," Phys. Rev. Lett. **116**, 063001 (2016).

[23] Kai Bongs *et al.*, "Development of a strontium optical lattice clock for the SOC mission on the ISS," Comptes Rendus Phys. **16**, 553–564 (2015).

[24] F. Sorrentino, . Alberti, G. Ferrari, V. Ivanov, N. Poli, M. Schioppo, and G. Tino, "Quantum sensor for atom-surface interactions below 10μm," Phys. Rev. A **79**, 013409 (2009).

[25] Vladyslav V Ivanov, "Study of surface potentials using resonant tunnelling of cold atoms in optical lattices," J. Phys. B At. Mol. Opt. Phys. **45**, 205004 (2012).

[26] M. G. Tarallo, T. Mazzoni, N. Poli, D. V. Sutyrin, X. Zhang, and G. M. Tino, "Test of Einstein equivalence principle for 0-spin and half-integer-spin atoms: Search for spin-gravity coupling effects," Phys. Rev. Lett. **113**, 1–5 (2014).

[27] Thomas H. Loftus, Tetsuya Ido, Martin M. Boyd, Andrew D. Ludlow, and Jun Ye, "Narrow line cooling and momentum-space crystals," Phys. Rev. A - At. Mol. Opt. Phys. **70**, 1–14 (2004).

[28] Simon Stellmer, Benjamin Pasquiou, Rudolf Grimm, and Florian Schreck, "Laser cooling to quantum degeneracy," Phys. Rev. Lett. **110**, 1–5 (2013).

[29] J. Reichel and V. Vuletic, *Atom Chips* (Wiley, 2011).

[30] Mark Keil, Omer Amit, Shuyu Zhou, David Groswasser, Yonathan Japha, and Ron Folman, "Fifteen years of cold matter on the atom chip: promise, realizations, and prospects," J. Mod. Opt. **0340**, 1–46 (2016).

[31] Yu-ju Lin, Igor Teper, Cheng Chin, and Vladan Vuletić, "Impact of the Casimir-Polder Potential and Johnson Noise on Bose-Einstein Condensate Stability Near Surfaces," Phys. Rev. Lett. **92**, 050404 (2004).

[32] D. J. Alton, N. P. Stern, Takao Aoki, H. Lee, E. Ostby, K. J. Vahala, and H. J. Kimble, "Strong interactions of single atoms and photons near a dielectric boundary," Nat. Phys. **7**, 159–165 (2010).

[33] P. G. Petrov, S. MacHluf, S. Younis, R. MacAluso, T. David, B. Hadad, Y. Japha, M. Keil, E. Joselevich, and R. Folman, "Trapping cold atoms using surface-grown carbon nanotubes," Phys. Rev. A - At. Mol. Opt. Phys. **79**, 1–11 (2009).

[34] A. González-Tudela, C. L. Hung, D. E. Chang, J. I. Cirac, and H. J. Kimble, "Subwavelength vacuum lattices and atom-atom interactions in photonic crystals," Nat. Photonics **9**, 320 (2015).

[35] Richard P. Feynman, *QED: The Strange Theory of Light and Matter* (Princeton University Press, Princeton, N.J., 1985).

[36] Peter W. Milonni, *The Quantum Vacuum: An Introduction to Quantum Electrodynamics* (Academic Press, San Diego, CA, 1994).

[37] H. A. Bethe, "The Electomagnetic Shift of Energy Levels," Phys. Rev. **72**, 339–341 (1947).

[38] Tatsumi Aoyama, Masashi Hayakawa, Toichiro Kinoshita, and Makiko Nio, "Tenth-order QED contribution to the electron g-2 and an improved value of the fine structure constant," Phys. Rev. Lett. **109**, 13–16 (2012).

[39] Daniel A. Steck, "Quantum and Atom Optics," course notes available online at http://steck.us/teaching (2006).

[40] H. B. G. Casimir, "On the attraction between two perfectly conducting plates," Proc. K. Ned. Akad. Wet. **51**, 150 (1948).

[41] P. W. Milonni, R. J. Cook, and M. E. Goggin, "Radiation pressure from the vacuum: Physical interpretation of the Casimir force," Phys. Rev. A **38**, 1621–1623 (1988).

[42] E. J. W. Verwey, "Theory of the stability of lyophobic colloids." J. Phys. Colloid Chem. **51**, 631–636 (1947).

[43] E. A. Power and T. Thirunamachandran, "The Non-Additive Dispersion Energies for N Molecules: A Quantum Electrodynamical Theory," Proc. R. Soc. A Math. Phys. Eng. Sci. **401**, 267–279 (1985).

[44] Holger Gies, Kurt Langfeld, and Laurent Moyaerts, "Casimir effect on the worldline," J. High Energy Phys. **2003**, 018–018 (2003).

[45] Klaus Aehlig and Helge Dietert, "Casimir Forces via Worldline Numerics: Method Improvements and Potential Engineering Applications," arXiv Prepr. arXiv1110.5936v1 , 1–13 (2011).

[46] Jonathan B. Mackrory, Tanmoy Bhattacharya, and Daniel A. Steck, "Worldline approach for numerical computation of electromagnetic Casimir energies: Scalar field coupled to magnetodielectric media," Phys. Rev. A **94**, 042508 (2016).

[47] Stephen M. Barnett, Alain Aspect, and Peter W. Milonni, "On the quantum nature of the Casimir-Polder interaction," J. Phys. B At. Mol. Opt. Phys. **33**, L143–L149 (2000).

[48] M. Bordag, U. Mohideen, and V. M. Mostepanenko, "New developments in the Casimir effect," Phys. Rep. **353**, 1–205 (2001).

[49] V. A. Parsegian, *Van der Waals Forces: A Handbook for Biologists, Chemists, Engineers, and Physicists* (Cambridge University Press, 2005).

[50] G. L. Klimchitskaya, U. Mohideen, and V. M. Mostepanenko, "The Casimir force between real materials: Experiment and theory," Rev. Mod. Phys. **81**, 1827–1885 (2009).

[51] D. Dalvit, P. Milonni, D. Roberts, and F. da Rosa, eds., *Casimir Physics*, Lecture Notes in Physics (Springer Berlin Heidelberg, 2011).

[52] Alejandro W. Rodriguez, Federico Capasso, and Steven G. Johnson, "The Casimir effect in microstructured geometries," Nat. Photonics **5**, 211–221 (2011).

[53] E. M. Lifshitz, "The theory of molecular attractive forces between solids," J. Exp. Theor. Phys. , 73–83 (1956).

[54] I. E. Dzyaloshinskii, E. M. Lifshitz, and L. P. Pitaevskii, "General Theory of van der Waals' Forces," Physics-Uspekhi **4**, 153–176 (1961).

[55] A. O. Sushkov, W. J. Kim, D. A. R. Dalvit, and S. K. Lamoreaux, "Observation of the thermal Casimir force," Nat. Phys. **7**, 230–233 (2011).

[56] S. K. Lamoreaux, "Demonstration of the Casimir Force in the 0.6 to 6 μm Range," Phys. Rev. Lett. **78**, 5–8 (1997).

[57] G. Bressi, G. Carugno, R. Onofrio, and G. Ruoso, "Measurement of the Casimir Force between Parallel Metallic Surfaces," Phys. Rev. Lett. **88**, 041804 (2002).

[58] U. Mohideen and Anushree Roy, "Precision Measurement of the Casimir Force from 0.1 to 0.9 μm," Phys. Rev. Lett. **81**, 4549–4552 (1998).

[59] H. B. Chan, V. A. Aksyuk, R. N. Kleiman, D. J. Bishop, and F. Capasso, "Quantum mechanical actuation of microelectromechanical systems by the Casimir force." Science **291**, 1941–4 (2001).

[60] Mariangela Lisanti, Davide Iannuzzi, and Federico Capasso, "Observation of the skin-depth effect on the Casimir force between metallic surfaces." Proc. Natl. Acad. Sci. U. S. A. **102**, 11989–92 (2005).

[61] H. B. Chan, Y. Bao, J. Zou, R. A. Cirelli, F. Klemens, W. M. Mansfield, and C. S. Pai, "Measurement of the casimir force between a gold sphere and a silicon surface with nanoscale trench arrays," Phys. Rev. Lett. **101**, 1–4 (2008).

[62] Francesco Intravaia, Stephan Koev, Il Woong Jung, A. Alec Talin, Paul S. Davids, Ricardo S. Decca, Vladimir A. Aksyuk, Diego A. R. Dalvit, and Daniel López, "Strong Casimir force reduction through metallic surface nanostructuring." Nat. Commun. **4**, 2515 (2013).

[63] J. N. Munday, Federico Capasso, and V. Adrian Parsegian, "Measured long-range repulsive Casimir-Lifshitz forces." Nature **457**, 170–3 (2009).

[64] F. Michael Serry, Dirk Walliser, and G. Jordan Maclay, "The role of the casimir effect in the static deflection and stiction of membrane strips in microelectromechanical systems (MEMS)," J. Appl. Phys. **84**, 2501 (1998).

[65] E. Buks and M. L. Roukes, "Stiction, adhesion energy, and the Casimir effect in micromechanical systems," Phys. Rev. B **63**, 033402 (2001).

[66] Gauthier Torricelli, Peter J. Van Zwol, Olex Shpak, George Palasantzas, Vitaly B. Svetovoy, Chris Binns, Bart J. Kooi, Peter Jost, and Matthias Wuttig, "Casimir force contrast between amorphous and crystalline phases of AIST," Adv. Funct. Mater. **22**, 3729–3736 (2012).

[67] Xi-fang Liu, Yong Li, and H. Jing, "Casimir switch: steering optical transparency with vacuum forces," Sci. Rep. **6**, 27102 (2016).

[68] A. Shih and V. A. Parsegian, "Van der Waals forces between heavy alkali atoms and gold surfaces: Comparison of measured and predicted values," Phys. Rev. A **12**, 835–841 (1975).

[69] A. Anderson, S. Haroche, E. A. Hinds, W. Jhe, and D. Meschede, "Measuring the van der Waals forces between a Rydberg atom and a metallic surface," Phys. Rev. A **37**, 3594–3597 (1988).

[70] V. Sandoghdar, C. I. Sukenik, E. Hinds, and Serge Haroche, "Direct measurement of the van der Waals interaction between an atom and its images in a micron-sized cavity," Phys. Rev. Lett. **68**, 3432–3435 (1992).

[71] C. Sukenik, M. Boshier, D. Cho, V. Sandoghdar, and E. Hinds, "Measurement of the Casimir-Polder force," Phys. Rev. Lett. **70**, 560–563 (1993).

[72] John Perreault, Alexander Cronin, and T. Savas, "Using atomic diffraction of Na from material gratings to measure atom-surface interactions," Phys. Rev. A **71**, 053612 (2005).

[73] S. Lepoutre, H. Jelassi, V. P. A. Lonij, G. Trénec, M. Büchner, A. D. Cronin, and J. Vigué, "Dispersive atom interferometry phase shifts due to atom-surface interactions," EPL (Europhysics Lett. **88**, 20002 (2009).

[74] Vincent P. A. Lonij, William F. Holmgren, and Alexander D. Cronin, "Magic ratio of window width to grating period for van der Waals potential measurements using material gratings," Phys. Rev. A **80**, 062904 (2009).

[75] D. Harber, J. Obrecht, J. McGuirk, and E. Cornell, "Measurement of the Casimir-Polder force through center-of-mass oscillations of a Bose-Einstein condensate," Phys. Rev. A **72**, 033610 (2005).

[76] J. M. Obrecht, R. J. Wild, M. Antezza, L. P. Pitaevskii, S. Stringari, and E. A. Cornell, "Measurement of the temperature dependence of the Casimir-Polder force." Phys. Rev. Lett. **98**, 063201 (2007).

[77] J. McGuirk, D. Harber, J. Obrecht, and E. Cornell, "Alkali-metal adsorbate polarization on conducting and insulating surfaces probed with Bose-Einstein condensates," Phys. Rev. A **69**, 062905 (2004).

[78] A. Landragin, J. Courtois, G. Labeyrie, N. Vansteenkiste, Ci. Westbrook, and A. Aspect, "Measurement of the van der Waals Force in an Atomic Mirror." Phys. Rev. Lett. **77**, 1464–1467 (1996).

[79] N. Westbrook, C. I. Westbrook, a. Landragin, G. Labeyrie, L. Cognet, V. Savalli, G. Horvath, a. Aspect, C. Hendel, K. Moelmer, J.-Y. Courtois, W. D. Phillips, R. Kaiser, and V. Bagnato, "New Physics with Evanescent Wave Atomic Mirrors: The van der Waals Force and Atomic Diffraction," Phys. Scr. **T78**, 7 (1998).

[80] Fujio Shimizu, "Specular Reflection of Very Slow Metastable Neon Atoms from a Solid Surface," Phys. Rev. Lett. **86**, 987–990 (2001).

[81] A. K. Mohapatra and C. S. Unnikrishnan, "Measurement of the van der Waals force using reflection of cold atoms from magnetic thin-film atom mirrors," Europhys. Lett. **73**, 839–845 (2006).

[82] T. E. Judd, R. G. Scott, A. M. Martin, B. Kaczmarek, and T. M. Fromhold, "Quantum reflection of ultracold atoms from thin films, graphene and semiconductor heterostructures," New J. Phys. **13** (2011), 10.1088/1367-2630/13/8/083020.

[83] Helmar Bender, Christian Stehle, Claus Zimmermann, Sebastian Slama, Johannes Fiedler, Stefan Scheel, Stefan Yoshi Buhmann, and Valery N. Marachevsky, "Probing atom-surface interactions by diffraction of Bose-Einstein condensates," Phys. Rev. X **4**, 1–10 (2014).

[84] H. Bender, Ph. W. Courteille, C. Marzok, C. Zimmermann, and S. Slama, "Direct Measurement of Intermediate-Range Casimir-Polder Potentials," Phys. Rev. Lett. **104**, 083201 (2010).

[85] M. Oria, M. Chevrollier, D. Bloch, M. Fichet, and M. Ducloy, "Spectral Observation of Surface-Induced Vanderwaals Attraction on Atomic Vapor," Europhys. Lett. **14**, 527–532 (1991).

[86] Horacio Failache, Solomon Saltiel, Michèle Fichet, Daniel Bloch, and Martial Ducloy, "Resonant van der Waals Repulsion between Excited Cs Atoms and Sapphire Surface," Phys. Rev. Lett. **83**, 5467–5470 (1999).

[87] M. Fichet, G. Dutier, A. Yarovitsky, P. Todorov, I. Hamdi, I. Maurin, S. Saltiel, D. Sarkisyan, M.-P. Gorza, D. Bloch, and M. Ducloy, "Exploring the van der Waals atom-surface attraction in the nanometric range," Europhys. Lett. **77** (2007), 10.1209/0295-5075/77/54001.

[88] Athanasios Laliotis, Thierry Passerat de Silans, Isabelle Maurin, Martial Ducloy, and Daniel Bloch, "Casimir-Polder interactions in the presence of thermally excited surface modes." Nat. Commun. **5**, 4364 (2014).

[89] Andrew D. Ludlow, *The strontium optical lattice clock : Optical spectroscopy with sub-Hertz accuracy*, Ph.D. dissertation, UC Boulder (2008).

[90] C. Henkel and M. Wilkens, "Heating of trapped atoms near thermal surfaces," Europhys. Lett. **47**, 414–420 (1999).

[91] D. M. Harber and J. M. McGuirk, "Thermally induced losses in ultra-cold atoms magnetically trapped near room-temperature surfaces," J. low Temp. ... **133**, 229–238 (2003).

[92] Jun Ye, H. J. Kimble, and Hidetoshi Katori, "Quantum state engineering and precision metrology using state-insensitive light traps." Science **320**, 1734–8 (2008).

[93] R Grimm, M Weidemüller, and Y Ovchinnikov, "Optical dipole trap for neutral atoms," Adv. At. Mol. Opt. Phys. **42**, 95 (2000).

[94] Tetsuya Ido and Hidetoshi Katori, "Recoil-Free Spectroscopy of Neutral Sr Atoms in the Lamb-Dicke Regime," Phys. Rev. Lett. **91**, 1–4 (2003).

[95] Elizabeth Schoene, *Cold Atom Control with an Optical One-Way Barrier*, Ph.D. dissertation, University of Oregon (2010).

[96] James C. Camparo, "The diode laser in atomic physics," Contemp. Phys. **26**, 443 (1985).

[97] Carl E. Wieman and Leo Hollberg, "Using diode lasers for atomic physics," Rev. Sci. Instrum. **62**, 1 (1991).

[98] Cunyun Ye, *Tunable External Cavity Diode Lasers* (World Scientific, 2004).

[99] Gábor Galbács, "A Review of Applications and Experimental Improvements Related to Diode Laser Atomic Spectroscopy," Appl. Spectrosc. Rev. **41**, 259–303 (2006).

[100] A. L. Schawlow and C. H. Townes, "Infrared and optical masers," Phys. Rev. **112**, 1940–1949 (1958).

[101] Marek Osinski and Jens Buus, "Linewidth Broadening Factor in Semiconductor Lasers—An Overview," IEEE J. Quantum Electron. **23**, 9–29 (1987).

[102] Charles H. Henry, "Theory of the Linewidth of Semiconductor Lasers," IEEE J. Quantum Electron. **18**, 259–264 (1982).

[103] Govind P. Agrawal and Charles M. Bowden, "Concept of linewidth enhancement factor in semiconductor lasers," (1993).

[104] Daniel A. Steck, "Classical and Modern Optics," course notes available online at http://steck.us/teaching (2006).

[105] E. Patzak, A. Sugimura, S. Saito, T. Mukai, and H. Olesen, "Semiconductor laser linewidth in optical feedback configurations," Electron. Lett. **19**, 1026–1027 (1983).

[106] R. Kazarinov and C. Henry, "The relation of line narrowing and chirp reduction resulting from the coupling of a semiconductor laser to passive resonator," IEEE J. Quantum Electron. **23**, 1401–1409 (1987).

[107] P. Zorabedian and W. R. Trutna, "Interference-filter-tuned, alignment-stabilized, semiconductor external-cavity laser," Opt. Lett. **13**, 826–828 (1988).

[108] X. Baillard, A. Gauguet, S. Bize, P. Lemonde, Ph Laurent, A. Clairon, and P. Rosenbusch, "Interference-filter-stabilized external-cavity diode lasers," Opt. Commun. **266**, 609–613 (2006).

[109] Daniel J. Thompson and Robert E. Scholten, "Narrow linewidth tunable external cavity diode laser using wide bandwidth filter," Rev. Sci. Instrum. **83**, 1–6 (2012).

[110] K. B. Macadam, A. Steinbach, and C. Wieman, "A Narrow-Band Tunable Diode-Laser System With Grating Feedback, and a Saturated Absorption Spectrometer for Cs and Rb," (1992).

[111] L. Ricci, M. Weidemäller, T. Esslinger, A. Hemmerich, C. Zimmermann, V. Vuletic, W. König, and T. W. Hänsch, "A compact grating-stabilized diode laser system for atomic physics," Opt. Commun. **117**, 541–549 (1995).

[112] A. S. Arnold, J. S. Wilson, and M. G. Boshier, "A simple extended-cavity diode laser," Rev. Sci. Instrum. **69**, 1236 (1998).

[113] V. V. Vassiliev, S. A. Zibrov, and V. L. Velichansky, "Compact extended-cavity diode laser for atomic spectroscopy and metrology," Rev. Sci. Instrum. **77**, 1–4 (2006).

[114] Daniel Adam Steck, *Quantum Chaos, Transport, and Decoherence in Atom Optics*, Ph.D. dissertation, The University of Texas at Austin (2001).

[115] Tao Li, *Manipulation of Cold Atoms Using an Optical One-Way Barrier*, Ph.D. dissertation, University of Oregon (2008).

[116] Eryn C. Cook, Paul J. Martin, Tobias L. Brown-Heft, Jeffrey C. Garman, and Daniel A. Steck, "High passive-stability diode-laser design for use in atomic-physics experiments." Rev. Sci. Instrum. **83**, 043101 (2012).

[117] http://atomoptics.uoregon.edu/unilaser (2011).

[118] Erica Mason, *Generation of Repumping Light for Ultracold Strontium Experiments*, Bachelor's honors thesis, University of California, Santa Barbara (2013).

[119] Scott B. Papp, *Experiments with a two-species Bose-Einstein condensate utilizing widely tunable interparticle interactions*, Ph.D. dissertation, University of Colorado (2007).

[120] B. P. Abbott *et al.*, "LIGO: the Laser Interferometer Gravitational-Wave Observatory," Reports Prog. Phys. **72**, 076901 (2009).

[121] S. T. Smith, D. G. Chetwynd, and D. K. Bowen, "Design and assessment of monolithic high precision translation mechanisms," J. Phys. E. **20**, 977–983 (1987).

[122] Todd P. Meyrath, "An analog current controller design for laser diodes," available online at http://george.ph.utexas.edu/~meyrath/informal (2003).

[123] Jeremy J. Thorn, *Dissipative Control and Imaging of Cold Atoms*, Ph.D. dissertation, University of Oregon (2012).

[124] K. G. Libbrecht and J. L. Hall, "A lownoise highspeed diode laser current controller," Rev. Sci. Instrum. **64**, 2133–2135 (1993).

[125] Christopher J. Erickson, Marshall Van Zijll, Greg Doermann, and Dallin S. Durfee, "An ultrahigh stability, low-noise laser current driver with digital control." Rev. Sci. Instrum. **79**, 073107 (2008).

[126] Christopher M. Seck, Paul J. Martin, Eryn C. Cook, Brian C. Odom, and Daniel A. Steck, "Noise reduction of a Libbrecht-Hall style current driver," Rev. Sci. Instrum. **87**, 2–5 (2016).

[127] http://atomoptics.uoregon.edu/unilaser_cover (2011).

[128] A. D. Cimmarusti, J. A. Crawford, Norris D. G., and L. A. Orozco, "Enhancements to cavity quantum electrodynamics system," Rev. Mex. Fis. **57**, 29–35 (2011).

[129] Daryl W. Preston, "Doppler-free saturated absorption: Laser spectroscopy," Am. J. Phys. **64**, 1432 (1996).

[130] Fritz Riehle, *Frequency Standards: Basics and Applications* (Wiley, 2006).

[131] Philippe B. Gallion and Guy Debarge, "Quantum Phase Noise and Field Correlation in Single Frequency Semiconductor Laser Systems," IEEE J. Quantum Electron. **20**, 343–349 (1984).

[132] Linden B. Mercer, "1/f Frequency Noise Effects on Self-Heterodyne Linewidth Measurements," J. Light. Technol. **9**, 485–493 (1991).

[133] Harrison E. Rowe, *Signals and noise in communication systems* (Van Nostrand, Princeton, N.J., 1965).

[134] M. Prentiss, A. Cable, J. E. Bjorkholm, Steven Chu, E. L. Raab, and D. E. Pritchard, "Atomic-density-dependent losses in an optical trap," Opt. Lett. **13**, 452 (1988).

[135] T. Arpornthip, C. A. Sackett, and K. J. Hughes, "Vacuum-pressure measurement using a magneto-optical trap," Phys. Rev. A - At. Mol. Opt. Phys. **85**, 1–7 (2012).

[136] Rowan W. G. Moore, Lucie A. Lee, Elizabeth A. Findlay, Lara Torralbo-Campo, Graham D. Bruce, and Donatella Cassettari, "Measurement of vacuum pressure with a magneto-optical trap: A pressure-rise method," Rev. Sci. Instrum. **86**, 4–7 (2015).

[137] T. A. Delchar, *Vacuum Physics and Techniques*, CRC Monographs on Statistics & Applied Probability (Springer Netherlands, 1993).

[138] Austin Chambers, *Modern Vacuum Physics*, Masters series in physics and astronomy (Taylor & Francis, 2004).

[139] J. H. Moore, C. C. Davis, M. A. Coplan, and S. C. Greer, *Building Scientific Apparatus*, Building Scientific Apparatus (Cambridge University Press, 2009).

[140] K. J. Ross and B. Sonntag, "High temperature metal atom beam sources," Rev. Sci. Instrum. **66**, 4409–4433 (1995).

[141] M. Schioppo, N. Poli, M. Prevedelli, St. Falke, Ch. Lisdat, U. Sterr, and G. M. Tino, "A compact and efficient strontium oven for laser-cooling experiments," Rev. Sci. Instrum. **83** (2012), 10.1063/1.4756936.

[142] Ruwan Senaratne, Shankari V. Rajagopal, Zachary A. Geiger, Kurt M. Fujiwara, Vyacheslav Lebedev, and David M. Weld, "Effusive atomic oven nozzle design using an aligned microcapillary array," Rev. Sci. Instrum. **86**, 1–5 (2015).

[143] C. B. Alcock, V. P. Itkin, and M. K. Horrigan, "Vapour Pressure Equations for the Metallic Elements: 2982500K," Can. Metall. Q. **23**, 309–313 (1984).

[144] R. G. Livesey, *Foundations of vacuum science and technology*, edited by J. M. Lafferty (Wiley, New York, 1998) Chap. 2.

[145] Wolfgang Demtröder, *Laser Spectroscopy: Basic Concepts and Instrumentation* (Springer Berlin Heidelberg, 2013).

[146] Norman Ramsey, *Molecular beams* (Oxford University Press, Oxford; New York, 1985).

[147] Harold J. Metcalf and Peter van der Straten, *Laser Cooling and Trapping* (Springer-Verlag, New York, 1999).

[148] J. A. Neuman, P. Wang, and A. Gallagher, "Robust high-temperature sapphire cell for metal vapors," Rev. Sci. Instrum. **66**, 3021–3023 (1995).

[149] Jafar Safarian and Thorvald A. Engh, "Vacuum Evaporation of Pure Metals," Metall. Mater. Trans. A **44**, 747–753 (2012).

[150] Tao Yang, Kanhaiya Pandey, Mysore Srinivas Pramod, Frederic Leroux, Chang Chi Kwong, Elnur Hajiyev, Zhong Yi Chia, Bess Fang, and David Wilkowski, "A high flux source of cold strontium atoms," Eur. Phys. J. D **69** (2015), 10.1140/epjd/e2015-60288-y.

[151] M. Bernardini, "Air bake-out to reduce hydrogen outgassing from stainless steel," J. Vac. Sci. Technol. A Vacuum, Surfaces, Film. **16**, 188 (1998).

[152] Donald J. Santeler, "New concepts in molecular gas flow," J. Vac. Sci. Technol. A Vacuum, Surfaces, Film. **4**, 338 (1986).

[153] Kevin M. Birnbaum, *Cavity QED with Multilevel Atoms*, Ph.D. dissertation, California Institute of Technology (2005).

[154] Y. Tito Sasaki, "A survey of vacuum material cleaning procedures: A subcommittee report of the American Vacuum Society Recommended Practices Committee," J. Vac. Sci. Technol. A Vacuum, Surfaces, Film. **9**, 2025 (1991).

[155] Satoshi Kurokouchi, Satsuo Shinoda, and Shinsaku Morita, "Properties of a newly developed concave nickel gasket for the ConFlat-type sealing system," J. Vac. Sci. Technol. A Vacuum, Surfaces, Film. **24**, 1847 (2006).

[156] Thomas Howard Loftus, *Laser Cooling and Trapping of Atomic Ytterbium*, Ph.D. dissertation, University of Oregon (2001).

[157] W. Ertmer, R. Blatt, J. L. Hall, and M. Zhu, "Laser manipulation of atomic beam velocities: Demonstration of stopped atoms and velocity reversal," Phys. Rev. Lett. **54**, 996–999 (1985).

[158] Jun Umezu and Fujio Shimizu, "Laser cooling of an atomic beam by spatial doppler tuning of a resonance transition," Jpn. J. Appl. Phys. **24**, 1655–1657 (1985).

[159] R. J. Napolitano, S. C. Zilio, and V. S. Bagnato, "Adiabatic following conditions for the deceleration of atoms with the Zeeman tuning technique," Opt. Commun. **80**, 110–114 (1990).

[160] William D. Phillips and Harold Metcalf, "Laser deceleration of an atomic beam," Phys. Rev. Lett. **48**, 596–599 (1982).

[161] Yuri B. Ovchinnikov, "A Zeeman slower based on magnetic dipoles," Opt. Commun. **276**, 261–267 (2007).

[162] Yuri B. Ovchinnikov, "A permanent Zeeman slower for Sr atomic clock," in *Eur. Phys. J. Spec. Top.*, Vol. 163 (2008) pp. 95–100.

[163] S. P. Krzyzewski, T. G. Akin, Parshuram Dahal, and E. R I Abraham, "A clip-on Zeeman slower using toroidal permanent magnets," Rev. Sci. Instrum. **85**, 1–6 (2014).

[164] Ian R. Hill, Yuri B. Ovchinnikov, Elizabeth M. Bridge, E. Anne Curtis, and Patrick Gill, "Zeeman slowers for strontium based on permanent magnets," J. Phys. B At. Mol. Opt. Phys. **47**, 075006 (2014).

[165] V. Lebedev and D. M. Weld, "Self-assembled Zeeman slower based on spherical permanent magnets," J. Phys. B At. Mol. Opt. Phys. **47**, 155003 (2014).

[166] Alexandria Parsagian and Michaela Kleinert, "Designing and building a permanent magnet Zeeman slower for calcium atoms using a 3D printer," Am. J. Phys. **83**, 892–899 (2015).

[167] G. Reinaudi, C. B. Osborn, K. Bega, and T. Zelevinsky, "Dynamically configurable and optimizable Zeeman slower using permanent magnets and servomotors," J. Opt. Soc. Am. B **29**, 729 (2012).

[168] Todd Philip Meyrath, *Experiments with Bose-Einstein Condensation in an Optical Box*, Ph.D. dissertation, The University of Texas at Austin (2005).

[169] J. Berger and D. Fekete, "Narrow single stabilized mode operation of coupled-stripe diode lasers," Appl. Phys. Lett. **47**, 1029–1031 (1985).

[170] C. Zimmermann, V. Vuletic, A. Hemmerich, and T. W. Hansch, "All solid state laser source for tunable blue and ultraviolet radiation," Appl. Phys. Lett. **66**, 2318 (1995).

[171] John H. Marquardt, "Grating-tuned semiconductor MOPA lasers for precision spectroscopy," in *Proc. SPIE*, Vol. 2834 (SPIE, 1996) pp. 34–40.

[172] J. N. Walpole, "Semiconductor amplifiers and lasers with tapered gain regions," Opt. quantum Electron. **28**, 623–645 (1996).

[173] Jayampathi C. B. Kangara, Andrew J. Hachtel, Matthew C. Gillette, Jason T. Barkeloo, Ethan R. Clements, Samir Bali, Brett E. Unks, Nicholas A. Proite, Deniz D. Yavuz, Paul J. Martin, Jeremy J. Thorn, and Daniel A. Steck, "Design and construction of cost-effective tapered amplifier systems for laser cooling and trapping experiments," Am. J. Phys. **82**, 805–817 (2014).

[174] Edeltraud Gehrig and Ortwin Hess, "Spatio-temporal dynamics of light amplification and amplified spontaneous emission in high-power tapered semiconductor laser amplifiers," Quantum Electron. IEEE J. **37**, 1345–1355 (2001).

[175] B. E. Unks, N. A. Proite, and D. D. Yavuz, "Generation of high-power laser light with Gigahertz splitting," Rev. Sci. Instrum. **78** (2007), 10.1063/1.2776971.

[176] A. C. Wilson, J. C. Sharpe, C. R. McKenzie, P. J. Manson, and D. M. Warrington, "Narrow-linewidth master-oscillator power amplifier based on a semiconductor tapered amplifier." Appl. Opt. **37**, 4871–4875 (1998).

[177] Matthias Fuchs, *Development of a High Power Stabilized Diode Laser System*, Master's thesis, University of Oregon (2006).

[178] Ken Takase, John K. Stockton, and Mark A. Kasevich, "High-power pulsed-current-mode operation of an overdriven tapered amplifier." Opt. Lett. **32**, 2617–9 (2007).

[179] http://atomoptics.uoregon.edu/ta_circuit (2014).

[180] "Application Note: Alignment of a DFB MOPA System with DFB TPA Configuration," Rev. 2.0, Eagleyard Photonics, available online at http://www.eagleyard.com/fileadmin/downloads/documents/eyP_AppNote_TPA_2-0.pdf.

[181] Yosuke Shimada, Yuko Chida, Nozomi Ohtsubo, Takatoshi Aoki, Makoto Takeuchi, Takahiro Kuga, and Yoshio Torii, "A simplified 461-nm laser system using blue laser diodes and a hollow cathode lamp for laser cooling of Sr," Rev. Sci. Instrum. **84**, 1–7 (2013).

[182] C. J. H. Pagett, P. H. Moriya, R. Celistrino Teixeira, R. F. Shiozaki, M. Hemmerling, and Ph. W. Courteille, "Injection locking of a low cost high power laser diode at 461 nm," Rev. Sci. Instrum. **87**, 4–8 (2016).

[183] P. A. Franken, A. E. Hill, C. W. Peters, and G. Weinreich, "Generation of optical harmonics," Phys. Rev. Lett. **7**, 118–119 (1961).

[184] A. Ashkin, G. D. Boyd, and J. M. Dziedzic, "Resonant Optical Second Harmonic Generation and Mixing," J. Quantum Electron. **2**, 109–124 (1966).

[185] G. D. Boyd and D. A. Kleinman, "Parametric interaction of focused Gaussian light beams," J. Appl. Phys. **39**, 3597–3639 (1968).

[186] I. Juwiler, A. Arie, A. Skliar, and G. Rosenman, "Efficient quasi-phase-matched frequency doubling with phase compensation by a wedged crystal in a standing-wave external cavity," Opt. Lett. **24**, 1236–1238 (1999).

[187] R. Le Targat, J. J. Zondy, and P. Lemonde, "75%-Efficiency blue generation from an intracavity PPKTP frequency doubler," Opt. Commun. **247**, 471–481 (2005).

[188] Eryn C. Cook, Ph.D. dissertation, University of Oregon (2017).

[189] Aaron D. Saenz, *461 nm Laser for Studies in Ultracold Neutral Strontium*, Master's thesis, Rice University (2005).

[190] Firuz Torabi-Goudarzi and Erling Riis, "Efficient cw high-power frequency doubling in periodically poled KTP," Opt. Commun. **227**, 389–403 (2003).

[191] T. W. Hänsch, I. S. Shahin, and A. L. Schawlow, "High-resolution saturation spectroscopy of the sodium D lines with a pulsed tunable dye laser," Phys. Rev. Lett. **27**, 707–710 (1971).

[192] G. C. Bjorklund, "Frequency-modulation spectroscopy: a new method for measuring weak absorptions and dispersions." Opt. Lett. **5**, 15 (1980).

[193] C. Wieman and T. W. Hänsch, "Doppler-free laser polarization spectroscopy," Phys. Rev. Lett. **36**, 1170–1173 (1976).

[194] K. L. Corwin, Z. T. Lu, C. F. Hand, R. J. Epstein, and C. E. Wieman, "Frequency-stabilized diode laser with the Zeeman shift in an atomic vapor." Appl. Opt. **37**, 3295–3298 (1998).

[195] T. Petelski, M. Fattori, G. Lamporesi, J. Stuhler, and G.M. Tino, "Doppler-free spectroscopy using magnetically induced dichroism of atomic vapor: a new scheme for laser frequency locking," Eur. Phys. J. D **22**, 279–283 (2003).

[196] Takatoshi Aoki, Kotaro Umezawa, Yuki Yamanaka, Naotomo Takemura, Yasuhiro Sakemi, and Yoshio Torii, "A 461 nm laser system and hollow-cathode lamp spectroscopy for magneto-optical trapping of Sr atoms," J. Phys. Soc. Japan **81**, 1–5 (2012).

[197] C. R. Vidal and J. Cooper, "Heat-pipe oven: A new, well-defined metal vapor device for spectroscopic measurements," J. Appl. Phys. **40**, 3370–3374 (1969).

[198] W. H. Parkinson, E. M. Reeves, and F. S. Tomkins, "Neutral calcium, strontium and barium: determination of f values of the principal series by the hook method," J. Phys. B At. Mol. Phys. **9**, 157 (1976).

[199] J. C. Turnbull, "Barium, strontium, and calcium as getters in electron tubes," J. Vac. Sci. Technol. **14**, 636 (1977).

[200] G. C. Bjorklund, M. D. Levenson, W. Lenth, and C. Ortiz, "Frequency modulation (FM) spectroscopy," Appl. Phys. B Photophysics Laser Chem. **32**, 145–152 (1983).

[201] John-Patrick Stacey, *Stabilization and Control In a Linear Ion Trap*, Ph.D. dissertation, Wadham College, Oxford (2003).

[202] J. D. Siverns, L. R. Simkins, S. Weidt, and W. K. Hensinger, "On the application of radio frequency voltages to ion traps via helical resonators," Appl. Phys. B Lasers Opt. **107**, 921–934 (2012).

[203] W. W. Macalpine and R. O. Schildknecht, "Coaxial Line with Helical Inner Conductor," Proc. IRE **47**, 2099–2105 (1959).

[204] Robert H. Johns W3JIP, "Homebrew Your Own Inductors," QST, 35 (1997).

[205] P. Bouyer, T. L. Gustavson, K. G. Haritos, and M. a. Kasevich, "Microwave signal generation with optical injection locking," Opt. Lett. **21**, 1502 (1996).

[206] Hank Zumbahlen, "Mini Tutorial MT-202: All Pass Filters," Analog Devices, available online at http://www.analog.com/media/en/training-seminars/tutorials/MT-202.pdf (2012).

[207] http://www.ethernut.de/.

[208] Peter E. Gaskell, Jeremy J. Thorn, Sequoia Alba, and Daniel A. Steck, "An open-source, extensible system for laboratory timing and control," Rev. Sci. Instrum. **80**, 1–10 (2009).

[209] Beniamino Barbieri and Nicolo Beverini, "Beniamino Barbieri and Nicolo Beverini Fisica,," Rev. Mod. Phys. **62** (1990).

[210] M.N. Reddy, "Laser Optogalvanic Spectroscopy: Experimental and Potential Applications in R&D," Def. Sci. Jounial **44**, 279–293 (1994).

[211] Windell Haven Oskay, *Atom optics experiments in quantum chaos*, Ph.D. dissertation, The University of Texas at Austin (2001).

[212] Pantita Palittapongarnpim, *Characterization of Magneto-optical Trap For Experiments in Light-Atom Interfacing*, Master's thesis, University of Calgary (2012).

[213] Steven Chu, L. Hollberg, J. E. Bjorkholm, Alex Cable, and A. Ashkin, "Three-dimensional viscous confinement and cooling of atoms by resonance radiation pressure," Phys. Rev. Lett. **55**, 48–51 (1985).

[214] "Engineering Design Guide," Sorbathane Inc., available online at http://www.sorbothane.com/engineering-design-guide.aspx (2015).

[215] Daniel A. Steck, "Analog and Digital Electronics," course notes available online at http://steck.us/teaching (2015).

[216] Y. Castin, H. Wallis, and J. Dalibard, "Limit of Doppler cooling," J. Opt. Soc. Am. B **6**, 2046–2057 (1989).

[217] T. Binnewies, G. Wilpers, U. Sterr, F. Riehle, J. Helmcke, T. E. Mehlstäubler, E. M Rasel, and W. Ertmer, "Doppler Cooling and Trapping on Forbidden Transitions," Phys. Rev. Lett. **87**, 123002 (2001).

[218] Jan Grünert and Andreas Hemmerich, "Sub-Doppler magneto-optical trap for calcium," Phys. Rev. A. At. Mol. Opt. Phys. **65**, 414011–414014 (2002).

[219] Thomas H. Loftus, Tetsuya Ido, Andrew D. Ludlow, Martin M. Boyd, and Jun Ye, "Narrow line cooling: Finite photon recoil dynamics," Phys. Rev. Lett. **93**, 11–14 (2004).

[220] Kurt R. Vogel, Timothy P. Dinneen, Alan Gallagher, and John L. Hall, "Narrow-line Doppler cooling of strontium to the recoil limit," IEEE Trans. Instrum. Meas. **48**, 618–621 (1999).

[221] P. D. Lett, W. D. Phillips, S. L. Rolston, C. E. Tanner, R. N. Watts, and C. I. Westbrook, "Optical molasses," J. Opt. Soc. Am. B **6**, 2084 (1989).

[222] J. Dalibard and C. Cohen-Tannoudji, "Laser cooling below the Doppler limit by polarization gradients: simple theoretical models," J. Opt. Soc. Am. B **6**, 2023 (1989).

[223] E. L. Raab, M. Prentiss, Alex Cable, Steven Chu, and D. E. Pritchard, "Trapping of Neutral Sodium Atoms with Radiation Pressure," Phys. Rev. Lett. **59**, 2631–2634 (1987).

[224] S. Friebel, C. D'Andrea, J. Walz, M. Weitz, and T. W. Hänsch, "CO2-laser optical lattice with cold rubidium atoms," Phys. Rev. A **57**, R20–R23 (1998).

[225] Simon Stellmer and Florian Schreck, "Reservoir spectroscopy of 5s5p 3P2 - 5snd 3D1,2,3 transitions in strontium," Phys. Rev. A - At. Mol. Opt. Phys. **90**, 1–14 (2014).

[226] J. E. Sansonetti and G. Nave, "Wavelengths, transition probabilities, and energy levels for the spectrum of neutral strontium (SrI)," J. Phys. Chem. Ref. Data **39** (2010), 10.1063/1.3449176.

[227] Yannick Bidel, *Piégeage et refroidissement laser du strontium Etude de leffet des interférences en diffusion multiple*, Ph.D. dissertation, University of Nice Sophia Antipolis (2002).

[228] G Ferrari, P Cancio, R Drullinger, G Giusfredi, N Poli, M Prevedelli, C Toninelli, and G M Tino, "Precision frequency measurement of visible intercombination lines of strontium." Phys. Rev. Lett. **91**, 243002 (2003).

[229] I. Courtillot, A. Quessada-Vial, A. Brusch, D. Kolker, G. D. Rovera, and P. Lemonde, "Accurate spectroscopy of Sr atoms," Eur. Phys. J. D **33**, 161–171 (2005).

[230] Rodney Loudon, *The quantum theory of light*, 2nd ed. (Oxford University Press, Oxford; New York, 1983).

[231] Xiaoji Zhou, Xia Xu, Xuzong Chen, and Jingbiao Chen, "Magic wavelengths for terahertz clock transitions," Phys. Rev. A - At. Mol. Opt. Phys. **81**, 1–7 (2010).

[232] D. M. Brink and G. R. Satchler, *Angular Momentum*, Oxford science publications (Clarendon Press, 1993).

[233] F. Bloch and A. Siegert, "Magnetic resonance for nonrotating fields," Phys. Rev. **57**, 522–527 (1940).

[234] Charlotte E. Moore, *Atomic energy levels as derived from the analyses of optical spectra* (National Technical Information Service, Springfield, Va., 1990).

[235] Masami Yasuda, Tetsuo Kishimoto, Masao Takamoto, and Hidetoshi Katori, "Photoassociation spectroscopy of ^{88}Sr: Reconstruction of the wave function near the last node," Phys. Rev. A - At. Mol. Opt. Phys. **73**, 4 (2006).

[236] H. G. C. Werij, Chris H. Greene, C. E. Theodosiou, and Alan Gallagher, "Oscillator strengths and radiative branching ratios in atomic Sr," Phys. Rev. A **46**, 1248–1260 (1992).

[237] C. H. Corliss and W. R. Bozman, *Experimental Transition Probabilities for Spectral Lines of Seventy Elements Derived from the NBS Tables of Spectralline Intensities: The Wavelength, Energy Levels, Transition Probability, and Oscillator Strength of 25,000 Lines Between 2000 and 9000A for*, NBS monograph (U.S. Government Printing Office, 1962).

[238] S. G. Porsev, Andrew D. Ludlow, Martin M. Boyd, and Jun Ye, "Determination of Sr properties for a high-accuracy optical clock," Phys. Rev. A - At. Mol. Opt. Phys. **78**, 1–9 (2008).

[239] H. J. Andra, H.-J. Plohn, W. Wittmann, A. Gaupp, J. O. Stoner Jr., and M. Gaillard, "Lifetimes of levels in neutral strontium (Sr I)," J. Opt. Soc. Am. **65**, 1410 (1975).

[240] Hanne Ludvigsen, Mika Tossavainen, and Matti Kaivola, "Laser linewidth measurements using self-homodyne detection with short delay," Opt. Commun. **155**, 180–186 (1998).

[241] Peter Horak and Wei H. Loh, "On the delayed self-heterodyne interferometric technique for determining the linewidth of fiber lasers." Opt. Express **14**, 3923–3928 (2006).

[242] Xiaopei Chen, *Ultra-Narrow Laser Linewidth Measurement Ultra-Narrow Laser Linewidth Measurement*, Ph.D. dissertation, Virginia Tech (2006).

[243] Hidemi Tsuchida, "Simple technique for improving the resolution of the delayed self-heterodyne method," Opt. Lett. **15**, 640–642 (1990).

[244] Wu Zhou, Kin Man Chong, and Hong Guo, "Linewidth measurement of Littrow structure semiconductor laser with improved methods," Phys. Lett. A **372**, 4327–4332 (2008).

[245] P. Gallion, F. J. Mendieta, and R. Leconte, "Single-frequency laser phase-noise limitation in single-mode optical-fiber coherent-detection systems with correlated fields," Josa **72**, 1–4 (1982).

[246] Klaus Petermann, *Laser Diode Modulation and Noise*, Advances in Opto-Electronics (Springer Netherlands, 1988).

[247] L. S. Cutler and C. L. Searle, "Some Aspects of the Theory and Measurement of Frequency Fluctuations in Frequency Standards," Proc. IEEE **54**, 136–154 (1966)